TÉCNICO LISBOA

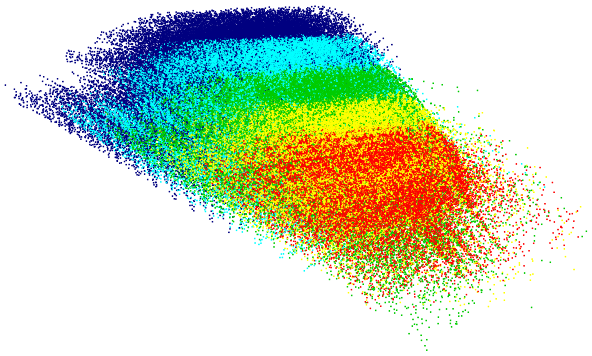

Multi-Parametric Analysis of Porous Radiant Burners

Marta Filipa Candelária Fidalgo

Thesis to obtain the Master of Science Degree in

Aerospace Engineering

Supervisor(s): Prof. José Manuel da Silva Chaves Ribeiro Pereira
Prof. Miguel Abreu Almeida Mendes

Examination Committee

Chairperson: Prof. Filipe Szolnoky Ramos Pinto Cunha
Supervisor: Prof. José Manuel da Silva Chaves Ribeiro Pereira
Member of the Committee: Prof. Viriato Sérgio de Almeida Semião

November 2019

Dedicated to my shadow, who made it a point to sabotage my arrogant efforts every step of the way.
Only with her on my side was this possible.

Acknowledgments

I would like to acknowledge all those who, one way or another, contributed to the successful completion of this dissertation. First, I would like to express my gratitude to my supervisors, Professor José Manuel Chaves Ribeiro Pereira and Professor Miguel Abreu Almeida Mendes, for their valuable knowledge and guidance throughout the course of the work. I am grateful also for my colleagues at LASEF, for their support and availability to lend a helping hand, especially Dr. Duarte Manuel Salvador Freire Silva de Albuquerque for his forthcoming aid with IT related issues. I extend my thanks to my friend Carlos Jorge Alves Porrais, whose insight on Decision Systems and Search Methods was crucial for the successful implementation of the dynamic Domain Exploration algorithm featured in this work. Lastly I would like to acknowledge my friends and family for their patience and support through this endeavor.

Also, I would like to thank the financial support provided by IDMEC-IST and the opportunity to take my work further into the scientific community.

Resumo

A combustão em meios porosos inertes é uma maneira eficaz de obter elevadas potências radiantes para uma grande variedade de densidades de energia, reduzindo também as emissões de poluentes. Trata-se de um fenómeno muito complexo no que toca à interacção entre os diferentes modos de transferência de calor, tendo os parâmetros que os governam muito potencial de influenciar a optimização do desempenho. Avanços na prototipagem rápida permitem a criação de novas configurações de meios porosos, com muitas possibilidades de adaptar materiais, propriedades geométricas, térmicas e radiativas a um objectivo específico de projecto. Nesta tese, várias investigações paramétricas multidimensionais são realizadas com o objectivo de caracterizar o domínio das configurações ideais de queimadores radiantes, especificamente relativo à eficiência radiante e ao máximo da temperatura do sólido. Emprega-se um modelo unidimensional com duas equações de energia, cinética química detalhada e aproximação S_6 para a equação de transferência radiativa. Os parâmetros do problema são desacopulados tanto quanto possível, deixando de lado as correlações existentes. É realizado um estudo sobre o comportamento da estabilidade da combustão, com o objetivo de compreender melhor o comportamento da chama, seguido do desenvolvimento de um código de aplicação encarregado do gestão autónoma de mais de 100 mil simulações interdependentes, sequencialmente. Constata-se que, dos 8 parâmetros investigados, a emissividade, a razão de excesso de ar, o coeficiente de extinção e o albedo são os parametros determinantes para alcançar melhor desempenho. Obtém-se um aumento da eficiência radiativa superior a 50%.

Palavras-chave: Combustão, Meios Porosos, Queimador Radiante, Radiação, Análise Multi-Paramétrica

Abstract

Combustion within porous inert media is an effective way to obtain high radiant outputs for a large range of power densities, whilst simultaneously reducing pollutant emissions. This phenomena is very complex in terms of the interaction between the different heat transfer modes, and the parameters that govern them hold much potential in terms of influence on the realm of performance optimization. Additive manufacturing allows for non-conventional porous media configurations to be created, with endless possibility to tailor materials, geometric, thermal and radiative properties to a specific design demand. In this Thesis, a series of multi-dimensional parametric investigations are conducted with the aim of characterizing the domain of optimal burner configurations, as it pertains to the radiant efficiency and the peak solid temperature. A one-dimensional model is employed, with two coupled energy equations for both gas and solid, multi-step chemical kinetics and the S_6 approximation to solve the radiative transfer equation. The problem's parameters are de-coupled as much as possible, leaving aside existing property correlations. A study on the stability behavior of porous media combustion is carried out, aimed at better grasping the flame behavior, followed by the development of an driver code tasked with the autonomous management of 100 k+ different inter-dependent burner case simulations simultaneously. It is found that, amongst the 8 parameters investigated, it is the emissivity, the excess air ratio, the extinction coefficient and the scattering albedo that are most determinant for achieving the best performance. The radiant efficiency is improved more than 50%.

Keywords: Combustion, Porous Media, Radiant Burner, Radiation, Multi-Parameter Analysis

Contents

List of Tables

List of Figures

Nomenclature

Greek symbols

β	PIM extinction coefficient [1/m]
ε	PIM material emissivity
η_{rad}	radiant efficiency
λ	excess air ratio
μ	dynamic viscosity [kg/m s] or direction angle cosine
ν_k	mass diffusion velocity of k^{th} species
ρ	density [kg/m^3]
σ	Stefan-Boltzmann constant 5.6696×10^{-8} [W/m^2 K^4] or standard deviation
σ_s	scattering coefficient
σ_{abs}	absorption coefficient
τ	radiative optical depth
Φ	equivalence ratio or scattering phase function
ϕ	solid porosity
$\dot{\omega_k}$	production rate of k^{th} species [kmol/m^3 s]
ω	PIM scattering albedo

Roman symbols

A	cross-sectional area [m^2] or Arrhenius pre-exponential factor [variable units]
$Al_2\ O_3$	aluminum oxide ceramic
C	individual burner case
C_p	specific heat capacity at constant pressure [J/kg K]
c_v	coefficient of variation

CH_4	methane
CO	carbon monoxide
CO_2	carbon dioxide
d_{pc}	characteristic pore structure dimension [m]
E	activation Energy
$\bar{h}_k$	enthalpy of the k^{th} species [J/kmol]
H_v	volumetric convective heat transfer coefficient [W/m^3 K]
H_2O	water
I	radiation intensity [W/m^2]
I_b	black body radiation intensity [W/m^2]
k	thermal conductivity [W/m K]
k_f	Reaction rate
L	flame-holder/burner length [m]
LHV_{CH_4}	lower heating value for the complete combustion of CH_4
$\dot{m}$	axial mass flow rate [kg/m^2 s]
M	molecular weight [kg/mol]
Nu	Nusselt number
N_2	nitrogen
NO_x	generic nitrogen oxide
p	environment pressure [Pa]
Pr	Prandtl number
Q_r	radiative heat flux [W/m^2]
Q_{comb}	input power/power density [W]
Q_{rad}	radiative output [W]
R	universal gas constant 8.3144×10^3 [J/kmol K]
Re	Reynolds number
S_L	burning velocity [m/s]
S_v	surface area to volume ratio [1/m]

S_{L_0} free flame burning velocity [m/s]

SiC silicon carbide ceramic

T temperature [K]

t time coordinate [s]

u axial mean velocity of the gas-phase [m/s]

x axial coordinate [m]

X_k molar fraction of k^{th} species

Y_k mass fraction of k^{th} species

Subscripts

∞ environment

eff effective

f flame front

g gas-phase

in inlet

max maximum

out outlet

ref reference

s solid-phase

Glossary

S_6	Approximation for the DOM that reduces the radiating hemisphere to 6 directions
1D	One-Dimensional
2D	Two-Dimensional
3D	Three-Dimensional
BC	Boundary Condition
CPU	Central processing unit
DOM	Discrete Ordinates Method is an approximated method to solve the RTE, reducing the radiating hemisphere into a discrete directions.
LASEF	Laboratory of fluid simulation in energy and fluids
PIM	Porous Inert Media are porous materials that do not promote catalytic effects
PMC	Porous Media Combustion is the name given to the stabilization of a combustion reaction wave inside a porous media
PPS	Progressive Parametric Study, a multi-dimensional multi-stage parametric study, increasing in complexity across stages. Developed by the Author to investigate multi-parameter influence.
PRB	Porous Radiant Burner is a branch of PMC burners that are directed toward high radiant outputs
RTE	Radiative Tranfer Equations

Chapter 1

Introduction

This introductory chapter provides a first exposition of the research subject featured in the Thesis. An overview on the motivation and relevance of the topic is given. It is also conducted a literature review on the current state of the field regarding the study object, from which the objectives of the present research are derived. Lastly, an outline of the thesis' structure is made.

1.1 Motivation

When our ancestor, *Homo Erectus*, learned how to control fire, the fate of the human species was forever changed. Ever since, we have relied on the power of the flame for most of our cultural and technological advancements, even in the face of the life threatening dangers that its use entails. Nowadays, the combustion of fossil fuels is a staple of worldwide energy production, accounting for 85% of the energy produced around the globe (Figure1.1), having sustained such remarkable relevance since the Industrial Revolution. However, hand in hand with the importance of this source of energy, goes the risks and impacts it brings about.

In the latest decades, the scientific community has risen questions about the impact of these technologies on human health and also the planet's, due to its potentially hazardous by-products, either from CO and NO_x compounds that can severely affect the respiratory tract, or to the high CO_2 emissions that impact global warming. Also, after almost 200 years of uninterrupted growing use, fossil fuel reserves have been on the decline, which paints a future where its availability will be diminished and its price will likely skyrocket. This has motivated the search for alternatives that can get around these issues.

These alternatives can be divided roughly into three categories: firstly there is nuclear energy, which is very promising with regard to sheer energy production capacity. However, nuclear fusion is still far from fruition and nuclear fission is a very controversial option due to its association with nuclear weapon production as well as *de facto* accidents like Chernobyl and Fukushima. Also, it is a complex technology, suited only for centralized energy production and presents important challenges with respect with the disposal of its radioactive waste. In the second group there are the so-called "Earth renewable" energies, which consist on the conversion of energy from natural phenomena, such as wind, solar or tidal, into

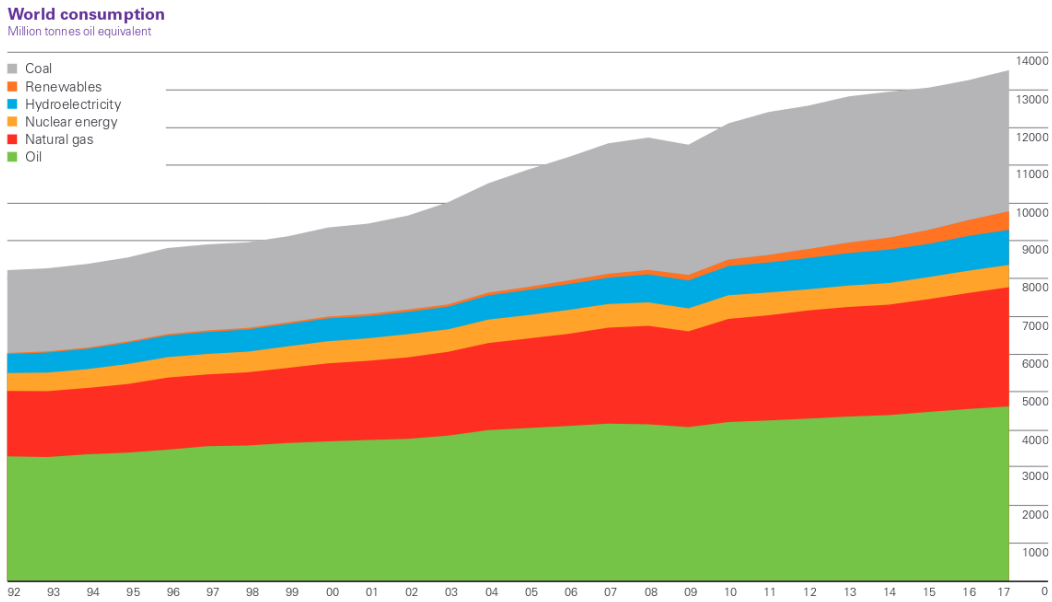

Figure 1.1: Prevalence of fossil fuel combustion as the main primary energy source worldwide [1].

electrical energy. The alternatives in this group however, despite being virtually limitless in availability and null in emissions (except for those involved in battery production), lack the reliability and simplicity of combustion. Lastly there is the path corresponding to the development of cleaner and more sustainable combustion technology. This can be achieved either by the adoption of cleaner and more abundant fuels, such as hydrogen, biomass, landfill gas or even CO_2 [2], to the development of new combustion techniques, that better harness the energy released during the reaction.

One such technique is known as Porous Media Combustion (PMC), and it consists of the burning of a premixed fuel inside a Porous Inert Media (PIM), usually characterized by high specific surface area, conductivity and emissivity. Its main advantages stem from the high multi-mode heat transfer that occurs within the porous solid when a premixed flame is stabilized inside it. The porous matrix acts as a heat recirculation device that redirects enthalpy from the exhaust gases back to the upstream of the flame, through a combination of convection, conduction and radiation heat transfer, preheating the incoming reactants. This leads to an increase in burning velocity and subsequent extension of lean flammability limits, when compared to conventional free flame burners [3–6]. Figure 1.2 illustrates these heat transfer mechanisms. Due to the intense heat transfer that takes place inside the burner, sharp temperature gradients are softened, which allied with stable lean combustion achieved with preheating, allows for very low emission of pollutants like NO_x and CO [7–9]. Another advantage that characterizes porous burners is the potential for high radiant outputs, due to the high burning rates and to the fact that solids can emit radiation more efficiently and uniformly than gas radiation [10, 11]. These characteristics make PMC a very attractive technology, with a long list of possible applications: from the burning of low calorific gases and destruction of VOCs (volatile organic compounds), to the production of hydrogen, usage as heat exchanger, applications in internal combustion engines and gas turbines, thermoelectric power generation as well as domestic and industrial heating applications (Figure 1.2) [4, 6, 12].

It is toward the improvement of heating and thermoelectric generation technologies that the research

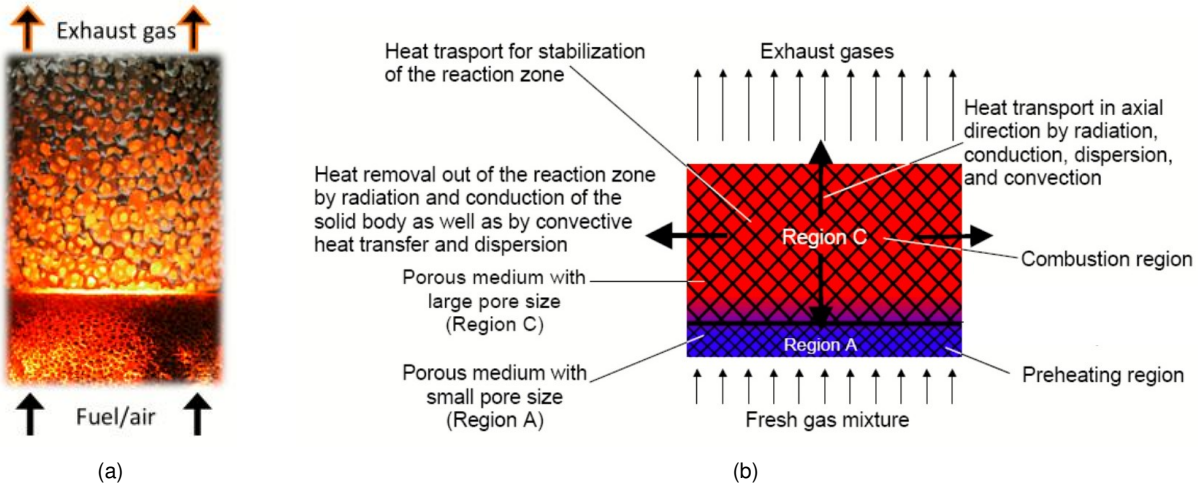

Figure 1.2: Porous Media Combustion: (a) combustion within a porous cylinder; (b) porous burner heat transfer scheme [5].

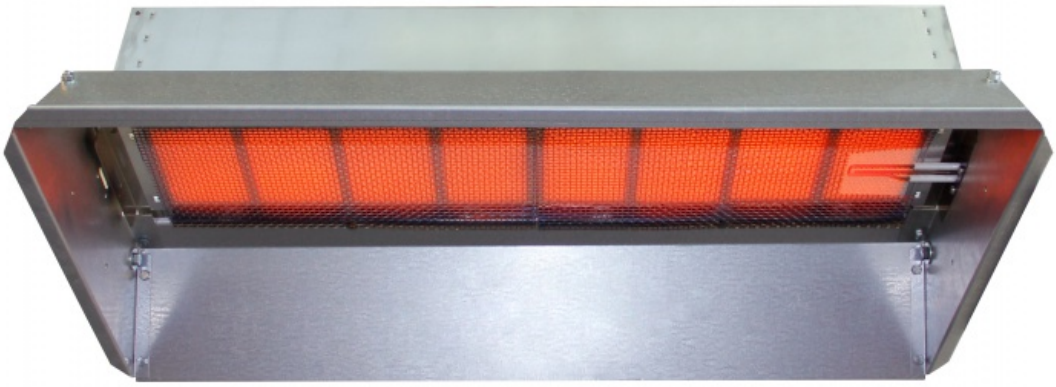

Figure 1.3: Example of a Porous Radiant Burner (PRB) heater from GoGas [13].

present in this thesis is directed. The burners employed in such applications are known as Porous Radiant Burners (PRBs - Figure 1.3), and their design is mostly focused on the improvement of the conversion of chemical energy into radiation, whilst taking into account durability and emission reduction. The porous materials typically used in this type of applications vary from ceramic/metal foams, to wire meshes or packed beds, which present challenges with regard to the measurement of geometric and thermodynamic properties. Furthermore, these properties are also inter-dependent, with several investigations on the correlations between the properties of these porous materials being reported [14–16]. However, with the rise of technologies like 3D printing, the possibility to produce a porous media with specific user requested properties is now at hand [17, 18]. This has prompted the search of new porous media configurations that can improve the performance of PRBs, namely with regard to radiant efficiency, that are not constrained by these relationships.

Another important issue regarding the performance of Porous Radiant Burners is the question about its life span. Due to being subjected to high temperatures from combustion [19], the porous solid that cages the flame is subject to quick wear and susceptible to cracks, oxidation and loss of its inert properties. Scheffler and Colombo [20] report limit temperatures of 1650^o C $(1923$ K$)$for SiC foams and commercially availiable burners typically have a 1450^o C $(1723$ K$)$ solid temperature limit [13].

The motivation for the present work stems from these points. Its objective is to provide a first step toward the maximization of the radiant efficiency of PRBs, whilst keeping solid temperatures below the durability limits, by gaining insight on the complex interactions between the several characterizing parameters of PRBs (thermal, geometric, radiative and operational) on its performance, with the ultimate goal of providing an optimal working zone and the relationship between these parameters on this optimal zone. The considerable amount of interconnected variables involved in the process of combustion within porous media makes it difficult to discern the best design option for a high performance radiant burner. Possible routes toward achieving an optimal design have included the use of diverse optimization algorithms, such as Search Methods and Genetic Algorithms [21, 22], however both options are only dedicated to finding the one best case, and since the specifications as to what the ”best case” is can vary according to the burner's intended use, this work strives to find instead the locus of optimal configurations.

1.2 Topic Overview

Investigations on porous media combustion are extensive, and have focused on various themes like flame characterization, heat transfer modeling, stability analysis, material and property description and burner performance, both with regard to emissions and efficiency. Howell *et al.* [4] conducted a review featuring experimental and modeling research, describing the structural properties of these materials and their heat transfer properties including convective, conduction, and radiative behavior. Exhaust emissions and radiant output from porous media burners are presented for both single-stage and multi-stage burners. They present approaches of varying sophistication that predict flame speeds, temperatures, concentration profiles and radiative efficiency. Mujeebu *et al.* [12, 23] also published a series of reviews on PMC, highlighting experimental investigations on premixed combustion, along with an exposition of possible applications of the concept, basic modeling approaches and suitable materials. They synthesized various modeling techniques ranging in levels of complexity and detail with regards to radiation, combustion, convective heat transfer and multi-dimensional analysis.

1.2.1 Origins

Porous media combustion has its origins in a 1971 study by Weinberg [24], with the introduction of the concept of excess enthalpy combustion: recuperation of energy from the exhaust gases to the upstream of the reaction zone, heating the incoming reactants. This mechanism was shown to make it theoretically possible to achieve temperatures in excess of the adiabatic flame temperature of the mixture

and extend the lean flammability limits. Hardesty and Weinberg [25] further investigated this concept through an experimental heat exchanger, and showed that this technique improved the flammability limits of a conventional flames allowing for the burning of leaner mixtures that yield gas temperatures as low as $1800\ \mathrm{K}$, consequently producing negligible rates of NOx compounds. Later, Takeno *et al.* [26–28] performed several studies that introduced the idea of inserting a high thermal conductivity porous solid into the flame zone as a means of achieving this type of flames. Their $1\mathrm{D}$ flame analysis showed promise in the burning of low heat content fuels, within a range of critical flow rates. They also found that the flame profile became thicker and more uniform, leading to lower rates of CO due to the consequent lower prevalence of incomplete fuel combustion. Echigo *et al.* [29] were able to achieve a 60% reduction in fuel consumption by placing a permeable and optically thick (low extinction coefficient) solid in the reaction zone, when compared with a conventional burner with the same radiative output (as referred to by Kamal and Mohamad [30]).

The following decades were ripe with investigative efforts on the combustion in porous media. The main branches followed consisted on the characterization of the flame, numerical modeling and stability analysis. Attention has also been given to the prediction of porous media heat transfer and geometric properties and to the burner durability.

Tong and Sathe [31] investigated the heat transfer characteristics of porous radiant burners. They employed a 1D conduction, convection and radiation model, where combustion was modeled as a spatially dependent heat generation zone. Local thermal non-equilibrium was assumed as well as an absorbing, emitting and scattering solid matrix. The Radiative Transfer Equation (RTE) was solved with spherical harmonics approximation. Effects of different parameters on the performance of porous radiant burners was investigated: for a given heat generation rate, large optical thickness and high heat transfer coefficient maximize radiant output, as well as low solid thermal conductivity, scattering albedo and flow velocity. Hsu *et al.* [3, 32] furthered the modeling of PMC with introduction of multi-step kinetics and improved description of thermophysical properties. They found that the preheating effect (and consequently the stability limits) was improved with increased convective heat transfer and effective thermal conductivity. They identified the need for optimization of burner characteristics, operating conditions and geometry in order to influence performance goals like pollutant emissions or thermal efficiencies. They found that the flame can be easily stabilized at the interface between two different porous blocks with different porosity and at the outlet if it faces a high temperature environment. Mital *et al.* [33] reported the first measurements of temperature and species distributions of the submerged reaction zone of a 2-layer porous radiant burners made of reticulated ceramic matrices and characterized them in terms of stability limits, radiant efficiencies and pollutant emissions. Reported radiant efficiencies were in the vicinity of 25%.

1.2.2 Modeling

With regard to modeling advances, Zhou and Pereira [34], compared predicions for the methane/air combustion in porous media between 4 different chemical kinetics models, ranging from a full mecha-

nism with 227 elemental reactions to the 1-step global mechanism. They found that 1-step mechanism overpredicts gas temperatures, but 4-step reduced offers good predictions. Pollutant emission should be studied with skeletal or full mechanisms. Later, Malico and Pereira [35] investigated the importance of radiation in the study of combustion in inert porous media. Radiative properties were studied, with a two-dimensional mass, momentum, gas and solid energy and species equations plus the S_6 approximation for the radiative transfer equation. It was showed that temperature profiles are sensitive to changes in radiative coefficients in the post-flame region, especially for increasing scattering albedo ($\omega = \sigma_s/(\sigma_s + \sigma_{abs})$). They also concluded that neglecting radiation yielded disagreement with experimental temperature profiles. Diamantis *et al.* [36] developed a one-dimensional model, including full radiation and detailed chemistry, that captured both surface and submerged flames. The model employed fixed flame approach included radiation heat loss to the upstream environment. They studied flame profiles, burning velocities and radiant efficiencies for submerged flames. They found that leaner mixtures lead to higher radiant efficiencies, for the same flame position. Peak radiant efficiencies achieved for submerged flames touched 25% for $\Phi = 0.5$

1.2.3 Performance study

Many investigative efforts, both numerical and experimental, have been carried out since, with the purpose of assessing porous radiant burners' performance characteristics. Keramiotis *et al.* [37, 38] carried out a series of experimental studies aimed at the characterization of porous burners with regards to thermal efficiency, pollutant formation, operating limits. They also studied burner fuel interchangeability, performing experiments for different types of fuels, including methane, LPG and syngas. The radiation output was defined through an idealized model, $Q_{rad} = \sigma\varepsilon A(T^4 – T_\infty^4)$. Thermal loads were varied from 200 to $1000\ \mathrm{kW/m^2}$ and excess air ratio $\Phi = 1.2$ to 1.6. The authors observed stable combustion across the ranges, fuel interchangeability and low emissions. Pollutant emissions were found below $50\ \mathrm{ppm}$ and the radiant efficiency for $800\ \mathrm{kW}$ around 25%. Hashemi [39] experimentally studied surface temperatures and radiant efficiencies of metal porous radiant burners for different porous medium thicknesses. Maximum surface temperature is achieve for the thickest burner and radiant efficiency is maximum for the lower firing rate and higher thickness.

Nejad *et al.* [40] investigated the effects of optical thickness, scattering albedo, excess air ratio, and porosity on the radiant efficiency. They employed a three-dimensional model, with 5-step chemical kinetics and S_6 approximation for the RTE. Optical thickness was found to increase radiant efficiency by enhancing the absorption by the solid phase. Porosity, which was coupled to the porous matrix's surface area, had a negative effect on radiant efficiency. High excess air ratio and high scattering albedo also led to low radiant efficiency. Liu *et al.* [41] studied the effects of inlet velocity, equivalence ratio, extinction coefficient and solid thermal conductivity on $2\mathrm{D}$ temperature distributions and velocity of CH_4/air lean combustion on a 2-layer burner, using transient model that takes into account the momentum equation. They found that contours of temperature and velocity are influenced by the burner wall and that conductivity has more impact on the upstream section than the flame holder section. They also observed

that the extinction coefficient has significant influence on temperature profiles of both gas and solid phases. Horsman and Daun [21] performed the design optimization of the radiant efficiency of a 2-layer radiant burner through surface response modeling, with downstream pore size and porosity as design parameters. They obtained statistically significant improvements and highlighted the importance of considering non-linear interactions between parameters. Radiant efficiency was defined as ratio between $T^4_{s,out}/T^4_{AdFlame}$, achieving 30% improvement. Randrianalisoa *et al.* [42] conducted investigations on the foam material for porous radiant burners. Their goal was to optimize energy efficiency and pollutant formation. They found that the optimal choice is lies in combination between different materials and porosity gradients.

1.2.4 Material properties

Interest was also shown in defining the relationships between the geometrical, thermal and radiative properties. Hsu and Howell [43] developed correlations for the effective thermal conductivity and for the extinction coefficient, from experiments with partially stabilized zirconia (PSZ) of different pore sizes and porosities. Deitrich *et al.* [44] investigated different ceramic foams, varying in material, porosity and cell density (PPC), using the Rossland approximation for the inverse analysis. They found that the total extinction coefficient has strong dependence on cell size and porosity, while the total emissivity is dependent solely on the porosity. Fu and Gore [15] developed relationships for the volumetric heat transfer coefficient, from experiments performed on foams ranging in pore density and thickness. They proposed a relationship for the pore diameter based on the solid porosity and the pore density. Other correlations are given for the relationship between the specific surface area and the pore density in the works of Scheffler and Colombo [20] and Kaviany [45].

1.2.5 Flame stability

Akbari and Riahi[46] looked into the effects of the inlet gas temperature, pore density, porosity and length of the porous medium on thermal performance and stability. A one-dimensional transient model with single step kinetics and radiation approximated with Rossland diffusion was used. Blow-off was recorded for decreasing equivalence ratio and pore density, as well as for increasing firing rate and porosity. Mendes *et al.* [47] carried out a numerical investigation of the stabilization diagram for CH_4/air premixed flames. A 1D numerical model was used, with energy equations for both gas and solid phases, chemical kinetics and several different radiation models. The authors studied the influence of boundary conditions and radiation models on flame stability, identifying unstable flames both on the upstream surface and on the downstream half of the porous matrix.

Despite extensive study on the radiant efficiency and radiant output of PRBs, there are not any studies, to the best of the author's knowledge, featuring the maximization of these quantities for more than 2 parameters simultaneously, which may be very relevant given the non-linear nature of the phenomena. Furthermore, no parametric studies of the peak temperature of the porous media, which is paramount for the durability of the burner, were found in the open literature. Lastly, all optimization efforts encountered

feature only one interest quantity. It is the aim of this thesis fulfill these gaps.

1.3 Objectives

The main aim of this thesis is to find and understand the optimal set of characterizing porous burner parameters that maximize the radiant efficiency and preserve a reasonable solid temperature. This aim can then be divided into the following specific objectives:

- Apply a one-dimensional numerical model to the investigation of the flame behavior of porous burners;

- Perform an optimization study/ progressive parametric study on the effect of several relevant parameters on a porous radiant burner efficiency *versus* maximum solid temperature;

- Develop a simulation management application that can autonomously perform the number of simulations required for the optimization effort, that also deals with failures in convergence, time management and the assignment of input and output information according to the models' complex needs;

- Establish parametric trends of influence and investigate non-linearities and inter-influence between parameters;

1.4 Thesis Outline

The present work is organized in the following manner:

- The first chapter is dedicated to the introduction of the research subject. The motivation and scientific context of the topic is presented, followed by an exposition of the relevant literature. The thesis objectives are then stated, followed by the present outline of the work structure.

- The second chapter features an analysis of porous media combustion. The mathematical model is presented, jointly with a presentation of the sample problem which will be target of the optimization study. Then, focus is given to the solution method employed and the corresponding validation case. The last section is dedicated to the exploration of typical burner flame configurations, limit cases, and overall stability behavior.

- In the third chapter the steps taken in order to implement the investigation efforts are discussed. An introduction to the strategy employed to achieve the main goal is given. The first section deals with design of experiment considerations, followed by a discussion of the structure and nuances of the $\mathrm{Domain\ Exploration}$ code, a management code developed by this thesis author to serve the requirements that the numerical experiments of this work pose.

- The fourth chapter is dedicated to the presentation of the results of the investigations. It is divided into the 3 stages that comprise the $\mathrm{Progressive\ Parametric\ Study}$ conceptualized by this thesis author. A summary of the findings is given.

- The fifth and last chapter features the author's conclusions on the work carried out. Recommendations for future work are given.

Chapter 2

Porous Media Combustion

This chapter presents a study of Porous Media Combustion (PMC), and its objective is to gain insight on the particularities of the phenomena, especially those that can impact the optimization study that is presented in the next chapter. The first section is dedicated to the mathematical model employed in the computations. A presentation of the sample problem is given, along with pertinent simplifying assumptions. An account of the governing equations, boundary conditions and assorted relationships and correlations required to close the mathematical model is given. In the second section the numerical implementation of the model is discussed. The methods used to solve the boundary value problem are presented as well as some particularities regarding the solution method. The section closes with the presentation of the validation of the method. The last section provides a characterization of porous media combustion, using the model presented in the previous sections. An illustrative case is given, along with considerations on flame behavior, stability, and analysis of temperature and species distributions.

2.1 Mathematical Modeling

The modeling of combustion within porous media is in itself a complex effort, as it must adequately capture several coexisting phenomena, from the chemical process of combustion to the radiative, convective and conductive heat transfer interactions between the 2 phases, solid and gas. Several approaches with varying degrees of sophistication have been undertaken by fellow authors, reviewed by Mujeebu *et al.* [23]. With regard to the present work, the model employed by Mendes *et al.* [47] is used, featuring reduced chemical kinetics, local thermal non-equilibrium and radiation. Two energy equations are used, one for the solid and another for the gas phase. What follows is a presentation of the sample problem to which the model is applied and the corresponding governing equations and closure models.

2.1.1 Problem Definition

In order to achieve the goal of the modeling effort it is necessary to capture the behavior of premixed combustion inside a porous radiant burner. In the present work the focus is on the flame-holder (interchangeably referred to as burner for the sake of simplicity) section of a 2-layer burner [33]. The burner

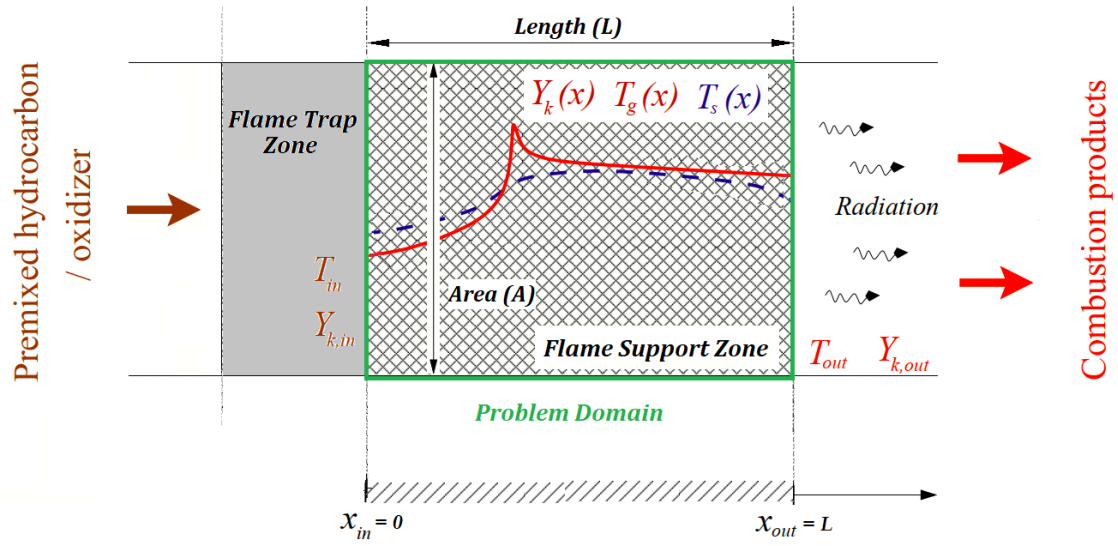

Figure 2.1: Schematic of the PRB reactor system to be modeled, along with the main features and problem variables.

section is cylindrical, having constant cross-sectional area (equal to $1\ \mathrm{m}^2$) and a length, L, much shorter than its diameter. The phenomena plays out as follows: first the fuel and air mixture enters the burner through the inlet, convectively receiving heat from the solid matrix as it passes through its voids, until it reaches the activation temperature for the reaction to occur. Heat is released from the flame and is transported by the gas flow through the remaining of the burner, exiting through the outlet, whilst simultaneously exchanging it back to the solid. In turn, the solid conducts and radiates part of it back upstream, and radiates the rest to the downstream environment. Since upstream the flame-holder it is assumed to be a flame-trap, it is considered that all radiation through the inlet section is reflected. The domain consists on both solid and gas-phase coexisting throughout its entirety, as illustrated in Figure 2.1.

Modeling assumptions

Given the complexity of the described phenomena and the optimization goal previously outlined, it is necessary to introduce some simplifying assumptions, which are as follows: the model is considered to be one-dimensional, as flow is predominantly axial from a macroscopic standpoint and the burner diameter-to-length ratio is high. Heat losses through the burner walls are neglected. Flow is considered laminar throughout the domain, given that flame speeds inside burners are typically low, corresponding to a pore Reynolds well under the transition treshold, $Re = 150$ (with the average pore diameter as the characteristic length) [48]. The burner is considered to be isobaric, due to typical high porosities as well as short burner length and low flow velocity. Gas and solid are considered to be in local thermal non-equilibrium, since there is a great volume of relevant convective interaction between the gas and the solid [49].

The gas-phase is modeled based on the typical assumptions for laminar premixed free-flame com-

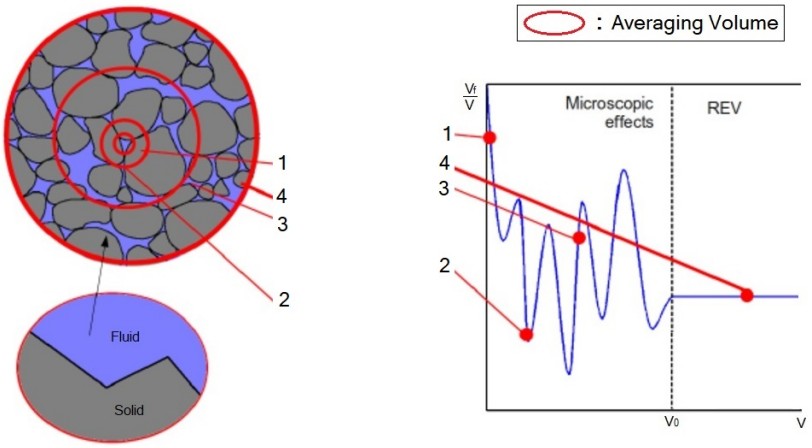

Figure 2.2: Representation of several volumetric elements for two-phase system averaging and corresponding evolution of fluid volume fraction with volumetric element size. V_4 corresponds to the REV [52].

putations [50]: ideal gas, combustion process governed by chemical kinetics, heat conduction governed by Fourrier's law. Mass diffusion due to concentration and thermal gradients, gravity effects and viscous dissipation are neglected. As for the porous media, it is considered to be a homogeneous, isotropic effective media, with negligible catalytic effects and fully static and rigid, as the only relevant phenomena are heat transfer processes such as conduction, convection and radiation, as mentioned earlier.

Regarding the modeling of radiation, the porous media is considered to be a isotropically diffuse, grey medium. The gas-phase is considered to be a non-participating medium, given that the solid's typical emissivity is much higher than the emissivity of the gas (at least 0.2 for solid *versus* 0.031 for $H_2O + CO_2$ in stoichiometric product mixture at $1800\mathrm{K}$ [51]), making solid radiation completely dominant.

2.1.2 Governing Equations

Given the problem at hand and the aforementioned assumptions, we are able to derive the governing equations that rule this system. Starting with the conservation laws, for mass, gas-species, gas energy and solid energy, followed by the rate equations for chemical kinetics, thermodynamic and transport properties and fundamental or correlation-based material related relationships necessary for model closure.

The general approach taken toward the modeling of macroscopic phenomena within porous media, such as combustion and heat transfer, starts with the averaging of the microscopic balance equations over a Representative Elementary Volume (REV), which is defined as the smallest volume that yields statistically meaningful local average properties, such as porosity (Figure 2.2). Further details on the local volume-averaging methodology can be found in [45].

Following the volume-averaging procedure, the balance equations for mass and gas-phase species become:

$$\text{Mass}:$$

$$\frac{\partial\left(\phi A\rho_g\right)}{\partial t}+\frac{\partial\dot{m}}{\partial x}=0 \tag{2.1}$$

$$\text{Gas}-\text{Phase Species}:$$

$$\phi A\rho_g\frac{\partial Y_k}{\partial t}+\dot{m}\frac{\partial Y_k}{\partial x}+\frac{\partial\left(\phi A\rho_g\nu_k Y_k\right)}{\partial x}-\phi A\dot{\omega}_k M_k=0 \tag{2.2}$$

where $\dot{m}=\phi A\rho_g S_L$ is the axial mass flow rate, cross-sectional area $A=1\ \mathrm{m}^2$ considered throughout. x denotes the axial coordinate and t the temporal one. Y_k refers to the mass fraction, ν_k the mass diffusion velocity, $\dot{\omega}_k$ the production rate and M_k the molecular weight of the k^{th} species. ρ_g denotes the gas mixture density. Both (2.1) and (2.2) take the usual free-flame problems formulation, with all fluxes being multiplied by the media porosity, ϕ. The solid and gas phase energy equations, on the other hand, are added an extra term to account for the convective heat exchange between the phases, becoming:

$$\text{Gas}-\text{Phase Energy}:$$

$$\begin{aligned}&\phi A\rho_g C_{p,g}\frac{\partial T_g}{\partial t}+\dot{m}C_{p,g}\frac{\partial T_g}{\partial x}-\frac{\partial}{\partial x}\left(\phi Ak_g\frac{\partial T_g}{\partial x}\right)\\&+\phi A\sum_k\left(\rho_g C_{p,k}\nu_k Y_k\right)\frac{\partial T_g}{\partial x}+\phi A\sum_k\left(\dot{\omega}_k\bar{h}_k\right)+AH_v\left(T_g-T_s\right)=0\end{aligned} \tag{2.3}$$

$$\text{Solid}-\text{Phase Energy}:$$

$$\left(1-\phi\right)A\frac{\partial\left(\rho_s C_{p,s}T_s\right)}{\partial t}-\frac{\partial}{\partial x}\left(Ak_{eff,s}\frac{\partial T_s}{\partial x}\right)+\frac{\partial\left(AQ_r\right)}{\partial x}-AH_v\left(T_g-T_s\right)=0 \tag{2.4}$$

with T_g and T_s the gas and solid phase temperatures, respectively, $C_{p,g}$, $C_{p,k}$ and $C_{p,s}$ the specific heat capacity for the gas mixture, species k and solid phase, respectively. The thermal conductivity of the gas mixture is denoted by k_g, and the effective thermal conductivity of the solid $k_{eff,s}$. $\bar{h_k}$ is the enthalpy of the k^{th} species, ρ_s the density of the solid, H_v the volumetric convective heat transfer coefficient and Q_r the radiative heat flux. The term $H_v\left(T_g-T_s\right)$ corresponds to the convective heat exchange that couples both equations (2.3) and (2.4). These conservation laws, (2.1) through (2.4), have as primary objective the computation of the problem main variables, $\dot{m}$, Y_k, T_g and T_s. The system needs, however, some appropriate boundary conditions, as well as additional sub-models for the missing quantities referenced in the equations in order to close the model, which follow in the next paragraphs.

Boundary conditions

The choice of boundary conditions is a problem specific endeavor, which requires special attention to be given to the particularities of the case. For the gas-phase BCs the usual Dirichlet for the inlet and Neumann for the outlet are used, with the exception of the boundary condition for the energy equation at the outlet. In this case it is added a term which accounts for the convective interaction with the solid.

They are as follows:

$$\text{Gas} - \text{Phase Species BCs}:$$

$$\text{inlet}: Y_k = Y_{k,in} \tag{2.5}$$

$$\text{outlet}: \frac{\partial Y_k}{\partial x} = 0 \tag{2.6}$$

$$\text{Gas} - \text{Phase Energy BCs}:$$

$$\text{inlet}: T_g = T_{g,in} \tag{2.7}$$

$$\text{outlet}: (1-\phi)\, h_s \left(T_g - T_s\right) + \phi k_g \frac{\partial T_g}{\partial x}\Big|_{-} = 0 \tag{2.8}$$

where $h_s = H_v/S_v$ is the PIM surface convective heat transfer coefficient and S_v is the ratio between PIM surface area to volume.

With regard to the mass balance equation (2.1), no pre-determination of the value for $\dot{m}$ at the inlet or outlet is made. Instead, the flame location is prescribed by fixing the gas temperature at a point near the flame front region, as expressed in equation (2.9). This option is made because numerical advantages are to be gained, which are explained further in Section 2.2 [53].

$$T_g\left(x = x_f\right) = T_f \tag{2.9}$$

For the solid-phase energy balance equation (2.4), the inlet and outlet boundary conditions are obtained by performing energy balances at both:

$$\text{Solid} - \text{Phase Energy BCs}:$$

$$\text{inlet}: -k_s \frac{\partial T_s}{\partial x} - h_s \left(T_g - T_s\right) + \varepsilon\sigma\left(T_s^4 - T_{in}^4\right) = 0 \tag{2.10}$$

$$\text{outlet}: k_s \frac{\partial T_s}{\partial x} - h_s \left(T_g - T_s\right) + \varepsilon\sigma\left(T_s^4 - T_{out}^4\right) = 0 \tag{2.11}$$

where T_{in} and T_{out} represent the environment temperatures upstream and downstream of the burner. Note that this is the model of a flame-holder, which means that a flame-trap is assumed to exist upstream from the inlet, considered to be low absorbing and highly scattering [54], leading to the assumption of $\varepsilon_{in} = 0$ in equation (2.10).

Gas-phase related properties

In order to get the density of the gas mixture the ideal gas equation of state is employed:

$$\rho_g = \frac{pM_g}{RT_g} \tag{2.12}$$

where p denotes the environment pressure. The transport and thermodynamic properties of the gas mixture are calculated as function of temperature and mixture composition [50, 55, 56].

Combustion is fundamentally a sequence of net exothermic chemical reactions that are brought about through the interaction between a fuel, an oxidant and an ignitor. In order to compute the net heat release of this process it is necessary to know each species, k, extinction/production rate $\dot{\omega}_k$ and the corresponding enthaply, $h_k = h_k^0 + c_{p,g}T_g$, which take part in equations (2.2) and (2.3). This information is provided by the chemical mechanism employed, that is, the database for the species, reaction steps and rate equations for the reactions to be accounted for in the combustion. The reaction rates are given in the modified Arrhenius form:

$$k_f = AT^b \exp(-E/RT) \tag{2.13}$$

with E as the activation energy, A the pre-exponent and b the temperature exponent. For the present case of methane/air premixed combustion the overall reaction amounts to:

$$CH_4 + 2\lambda\left(O_2 + 3.76N_2\right) \rightarrow CO_2 + 2H_2O + \left(\lambda - 1\right)O_2 + 2\lambda\left(3.76N_2\right) \tag{2.14}$$

where λ is the excess air ratio of the mixture ($\lambda = 1/\Phi$). The mechanism used was the 12-step augmented reduced mechanism described in [57], which is sufficient for this work goals. The use of more complex and time-consuming chemical mechanims, like the GRI 2.1 used in [36], is relegated for studies dedicated to the prediction of pollutant formation, as asserted in [34]. The use of a global one-step mechanism, on the other hand, would be lacking in the accuracy of flame temperature predictions, with the literature reporting over-estimations of flame speeds and adiabatic flame temperatures [3, 34].

Porous Media properties

Porous Media are notorious for the difficulty they provide in the determination of their characteristic properties, due to the complexity and variability of the internal geometry and material composition (Figure 2.3). It is thus necessary to perform some approximations and use experimental correlations in order to be able to provide some satisfying description of its role in a phenomena like porous media combustion.

One such property is the effective thermal conductivity of the solid, $k_{eff,s}$, referenced in equation (2.4), for which the parallel approximation is employed (considering $k_s \gg k_g$) [45]:

$$k_{eff,s} = \phi k_g + \left(1 - \phi\right)k_s \approx \left(1 - \phi\right)k_s \tag{2.15}$$

where k_s depends on the material of choice, as well as ρ_s and $C_{p,s}$. These last two are taken at constant temperature for Silicon Carbide (SiC) foams, since transient analysis is outside the scope of the work, only being used as a numerical tool when needed. The bulk solid thermal conductivity, k_s, shall be given as one of the inputs to the problem.

Regarding the volumetric convective heat transfer coefficient, H_v, various approaches can be taken toward it, when it comes to porous media combustion. From setting a constant value, usually in the

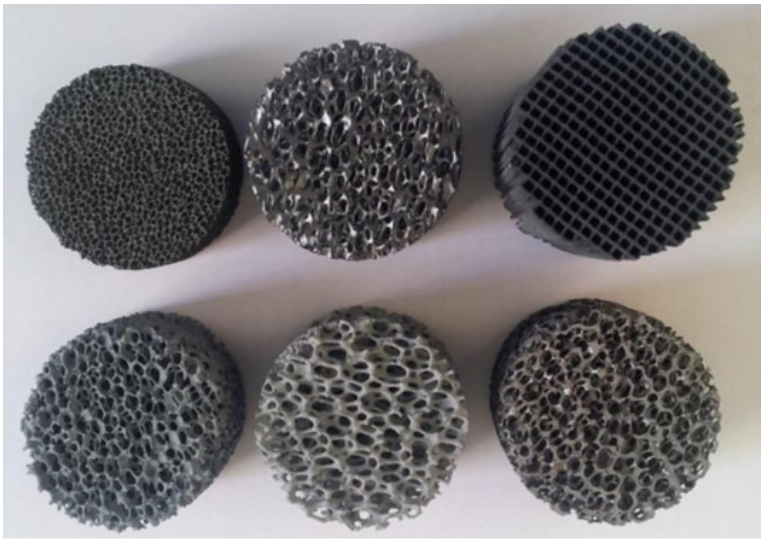

Figure 2.3: Different porous media that can be employed in PMC, varying in material type and internal structure. First line: $a-SiC$, $Si-SiC$, and SiC honeycombs; Second line: SiC + $Al2O3$, $SiC+SiO2+Al2O3$, $ZrB2$ [58].

order of $10^7 - 10^9 \ \ W/m^3.K$ [32, 49], to the use of correlations either for sample problems, such as the flow over a bank of cylinders [59], or specifically developed for porous media like foams or packed beds [14, 15]. The author's choice here is to employ the correlation in equation 2.16 according to [20, 45, 59]:

$$Nu = 0.3 + 0.664 Re^{1/2} Pr^{1/3} \tag{2.16}$$

with the Nusselt number, Nu, the pore Reynolds, $Re_{d_{pc}}$ and Prandtl, Pr being defined as:

$$Nu = \frac{H_v d_{pc}}{k_g S_v} \quad \text{(2.17a)} \qquad Re_{d_{pc}} = \frac{\phi \rho_g u d_{pc}}{\mu_g} \quad \text{(2.17b)} \qquad Pr = \frac{C_{p,g} \mu_g}{k_g} \quad \text{(2.17c)}$$

where d_{pc} is the characteristic pore diameter, u is the flow velocity, S_v the specific surface area of the PIM, μ_g and ρ_g the dynamic viscosity and the density of the gas mixture. The correlation was developed for flow through ducts, and its choice stems from not wanting to restrict the study to one specific type of porous media, for which the typical correlations are developed.

Radiation Modeling

With regard to radiation, it is necessary to compute the term $\partial \left(Q_r A \right) / \partial x$, which can be written as:

$$\frac{\partial \left(A Q_r \right)}{\partial x} = A \frac{\partial Q_r}{\partial x} \tag{2.18}$$

since the burner cross sectional area A is constant. The calculation of the term $\partial Q_r/\partial x$ from equation (2.18) is performed with recourse to the one-dimensional Radiative Transfer Equations (RTE) [60]:

$$\mu \frac{\mathrm{d}I(\tau,\mu)}{\mathrm{d}\tau} + I(\tau,\mu) = (1-\omega) I_b(T_s) + \frac{\omega}{2}\int_{-1}^{1} I(\tau,\mu_i)\,\Phi(\mu,\mu_i)\,\mathrm{d}\mu_i \tag{2.19}$$

$$\frac{\mathrm{d}Q_r}{\mathrm{d}\tau} = (1-\omega)\left(4\pi I_b(T_s) - 2\pi\int_{-1}^{1} I(\tau,\mu)\,\mathrm{d}\mu\right) \tag{2.20}$$

with $\tau = \beta x$ as the optical depth, β the extinction coefficient, and $I_b(T_s) = \sigma T_s^4/\pi$ as the black body intensity. μ_i corresponds to the unit vector for a given direction and Φ is the scattering phase function which is reduced to $\Phi(\mu,\mu_i) = 1$ due to the assumption of isotropic scattering. The corresponding boundary conditions are given by:

$$\tau = 0 \;:\; I(\tau,\mu) = \varepsilon_{in} I_b(T_{in}) - (1-\varepsilon)\,2\int_{-1}^{0} I(\tau,\mu_i)\,\mu_i \mathrm{d}\mu_i,\; 0 < \mu < 1 \tag{2.21}$$

$$\tau = \beta L \;:\; I(\tau,\mu) = \varepsilon_{out} I_b(T_{out}) - (1-\varepsilon)\,2\int_{0}^{1} I(\tau,\mu_i)\,\mu_i \mathrm{d}\mu_i,\; -1 < \mu < 0 \tag{2.22}$$

where $x = 0$ and $x = L$ are illustrated in 2.1 and they specify the inlet and outlet boundaries of the PIM. Both surfaces are considered here to be diffusely radiating grey surfaces each facing the environment, with environment temperatures $T_{in,\infty} = T_{out,\infty} = T_\infty = 300$ K. Regarding the inlet of the PIM, its emissivity is considered to be zero, $\varepsilon_{in} = 0$, which leads to the falling off of the first term in equation (2.21), remaining only the reflective portion of the boundary condition. This approximation of ε_{in} is made on the back of the assumption that upstream of the PIM there is a low absorbing, highly scattering media that serves as a flame-trap, as seen in Figure 2.1. The outlet emissivity is the same as the emissivity of the PIM, $\varepsilon_{out} = \varepsilon$.

With regard to the radiant efficiency, it is defined as the ratio between the radiant flux from the outlet surface to the outlet environment and the thermal load of the combustion reaction:

$$\eta_{rad} = \frac{Q_{rad}}{Q_{comb}}, \tag{2.23}$$

where

$$Q_{rad} = Q_{r,out} + (1-\phi)\,\varepsilon\sigma\left(T_{s,out}^4 - T_\infty^4\right) \tag{2.24}$$

$$Q_{comb} = \phi \rho_g S_L Y_{CH_4} LHV_{CH_4}. \tag{2.25}$$

2.2 Solution Method

The set of governing equations and corresponding sub-models presented in Section 2.1.2 are numerically solved with the in-house code POROUSN, which is an adaptation of the PREMIX [53] code that incorporates the solid-phase energy equation (2.4), convective heat transfer between gas and solid

phases, as well as the radiation model described in equatinos (2.19) and (2.20). The code relies on the CHEMKIN [55] and TRANSPORT [56] library packages for the computation of finite rate chemical kinetics and multicomponent molecular transport coefficients and variables.

In order to transform the boundary value problem posed in Section 2.1.2 into a set of algebraic equations, the finite differences method is applied to the governing equations, (2.1) to (2.4), with an adaptative non-uniform grid as basis. Steady terms are discretized with central differences, except for the convective terms for which first order upwind is used, whilst transient terms are discretized with recourse to backward Euler scheme. Despite the steady state nature of the research, transient terms are in fact not neglected, as they may be needed in order to aid the process of convergence, as is explained in the upcoming paragraphs.

2.2.1 Solution algorithm

In order to attempt the computation of a solution for the algebraic equations above, a damped Newton method is applied. This method is computationally less expensive than a full transient calculation, however it provides a rather limited convergence domain on its own. This is dealt with by performing a given number of time-steps when the Newton method fails, as to lend some physics to the solution and try and approximate it from the Newton's domain of convergence. This allows the overall method to produce converged results more reliably whilst not sacrificing too much computation time.

The method relies on a starting estimate to initiate the calculations, and is most effective when this estimate is close enough to the solution, in the convergence domain. This point is of importance for the assembly of the Domain Exploration code, presented in Section 3.3.

RTE Solution

Regarding the computation of the radiative heat flux, $\partial Q_r/\partial x$ from equation (2.4), the one-dimensional radiative heat transfer integro-differential system of equations has to be numerically solved. The method used is the Discrete Ordinates Method (namely the S_6 approximation) [60]. $\partial Q_r/\partial x$ is computed between every iteration of the main problem, using the previous iteration estimate for the solid-phase temperature.

2.2.2 Fixed Flame Position

Another relevant point that should be taken into account is the choice of boundary condition for equation (2.1). As stated in Section 2.1.2, the typical Dirichlet boundary condition imposed at the inlet is replaced by an implicit boundary condition at the flame-front, prescribing the gas temperature at a required position. This is done in order to avoid convergence problems that would arise otherwise: in order to stabilize a premixed flame at any point it is necessary to match the burning velocity to the flow velocity, and this equilibrium position will by rather sensitive to mass flow fluctuations, as can be seen in the case of freely propagating flames. Also, because of the sharp temperature gradients at the flame front there is a higher mesh density in this area. It follows that if the prescribed mass flow BC does not correspond

to the flame position of the starting estimate, a long time will be spent by the algorithm moving the flame and the mesh adaptation around, making it so that a lot of time will be spent trying to find the new flame position or ultimately lead to a failure in convergence.

The way this approach solves the problem is by eliminating the need for the computation of the flame position, which is set as $T_g\left(x_f\right) = T_f$, making it so that the refined mesh need not be altered and that the starting estimate is likely good. The approach requires though, that one variable be released, otherwise the problem would become over-determined. In this case it is the inlet mass flow rate, $\dot{m}$, which becomes an eigenvalue, to be determined as part of the solution.

The obvious problem that arises then is the impossibility to compute the solution for a specific input mass flow rate/power. The way to deal with this is discussed in the following subsection. It is also worthy of note that the solution computed with this method does not guarantee flame stability, as the flame is being artificially fixed. This topic is further discussed in Section 2.3.

Fixed Mass Flow Interface

Whilst fixing the flame position is a simple way to reduce the numerical complications that the computation of premixed combustion in porous media can entail, it also introduces two important limitations into the model: for one, since the flame position is fixed, the solution of a given case is not suitable to be used as a reasonable initial estimate for the computation of new case with a different flame position, as the temperature profile would be too different due to the high temperature gradients in the flame zone. The second, as mentioned earlier, the extinction of the Dirichlet BC for the mass equation (2.1) makes it so that the input power of the burner cannot be controlled or studied.

To deal with this, an artifice is included that shifts the coordinates of the mesh points from the previous solution, along with corresponding information like temperature and species distributions, to the required location. Points are added/removed from the inlet/outlet according to necessity. It is then possible to employ an iterative search process to find a required mass flow rate, $\dot{m}$ (within a tolerance), provided the assumption that the flame speed increases with increasing flame position, which is valid until it reaches a maximum value [61]. More on this is discussed in Section 2.3.

2.2.3 Model Validation

Having the mathematical model closed and the numerical implementation details ironed out, a validation study is carried out, against the results achieved by Diamantis and Goussis [36]. Temperature distributions for both solid and fluid are compared for different equivalence ratios, as the relationships between both the flame speed ratio, S_L/S_{L0}, and the radiant efficiency, η_{rad}, *versus* the flame position, x_f. The characteristics of the foam studied are presented in Table 2.1.

.

The present model estimates of the temperature distributions are in good agreement with the predictions from Diamantis *et al* [36], as can be seen in Figures 2.5. The slight overestimation downstream the flame can be explained by the fact that with simpler mechanism the transformation of CH_4 into CO_2

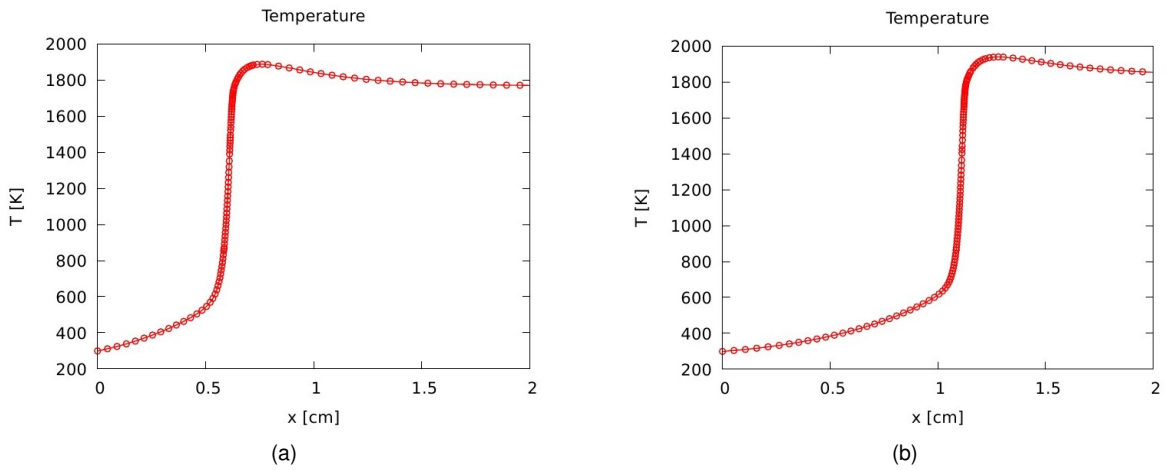

Figure 2.4: Mesh points for two different flame positions shifted by starting estimate moving artifice.

Property	Value	Units
Material	SiC	-
Burner length, L	3	cm
Pores per cm, PPC	8	cm^{-1}
Porosity, ϕ	0.9	-
Emissivity, ε	0.8	-
Scattering albedo, ω	0.8	-
Extinction coefficient, β	2.7	cm^{-1}
Bulk solid thermal conductivity, k_s	1	$\mathrm{W/(m.K)}$
Nusselt , Nu	$\left(0.0426 + \frac{1.236}{L/d_{pc}}\right) Re_{d_{pc}}$	-

Table 2.1: Foam characteristic parameters from the validation case, where $Nu = H_v d_{pc}^2 / k_g$ [36].

happens quicker, with the consequent increase in heat release, while a more complex mechanism CH_4 undergoes several slower transformations until it becomes CO_2. This effect is more noticeable for higher equivalence ratios [62].

The burning velocity is slightly overestimated whilst the radiant efficiency is underestimated. Nonetheless, the general behavior is consistent with the reference case for both quantities as seen in Figures 2.6. This discrepancy toward the reference case can be attributed to the fact that the reference case employs a very complex chemical mechanism and, as explained in Section 2.1.2, it does not benefit the purpose of the present work to sacrifice the required computational time to do so. The use of a simpler mechanism, however, is know to produce overestimation of flame speeds [62], as can be seen in this situation. The difference in radiation model employed is also of significance, since it has been shown how disturbances in the radiative heat transfer cause significant differences in the flame characterization, as seen in [35]. It can also be noted that the overestimation of S_L and underestimation of η_{rad} are consistent with each other: given the definition of radiant efficiency and combustion power provided in equations (2.23) through (2.25), it is straightforward to note that an increase in the first would logically lead to a decrease in the latter.

One can conclude then that the model described in the present chapter provides a good qualitative

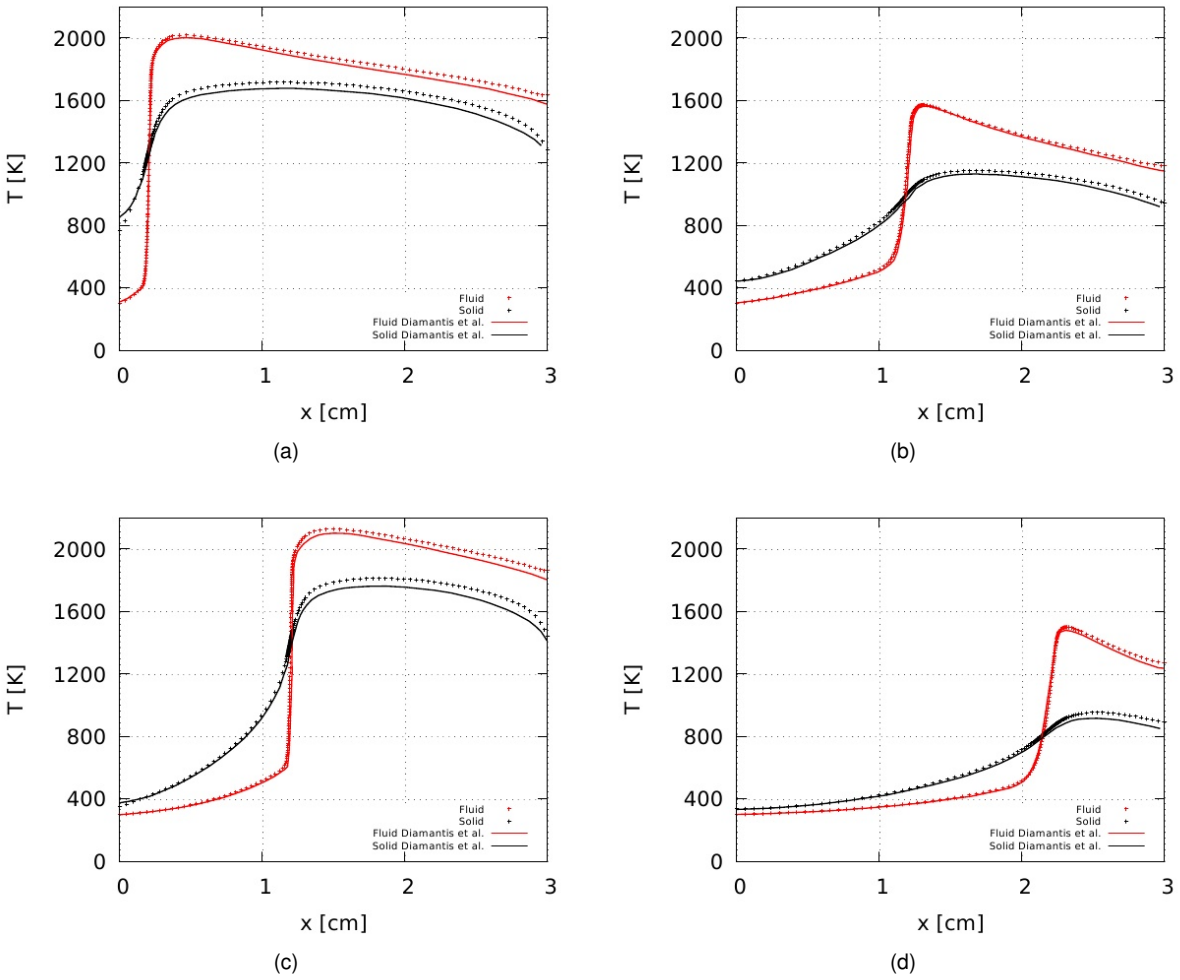

Figure 2.5: Comparisons of the temperature profiles acheived in [36] and by the model employed in this work: (a) $\Phi = 0.9$, $x_f = 0.20$ cm; (b) $\Phi = 0.5$, $x_f = 1.20$ cm;(c) $\Phi = 0.9$, $x_f = 1.19$ cm; (d) $\Phi = 0.5$, $x_f = 2.21$ cm.

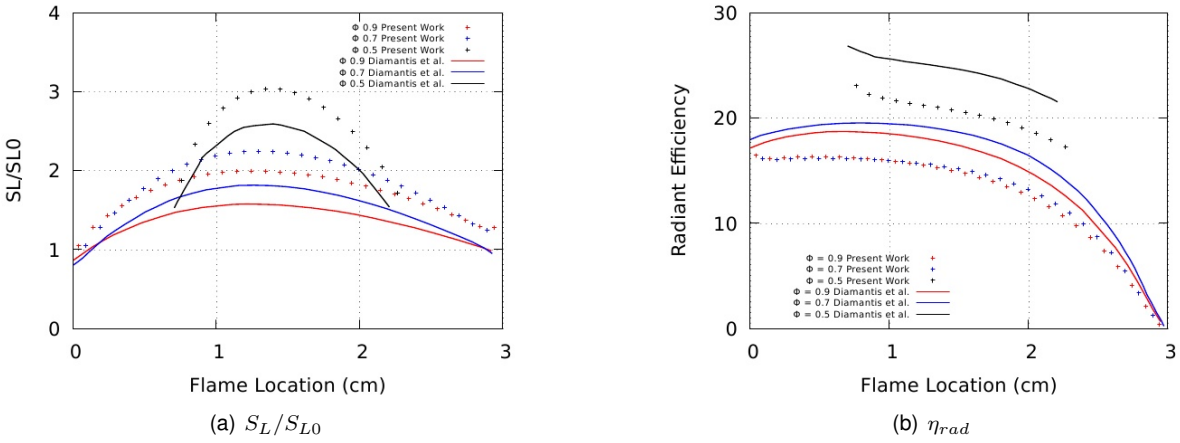

Figure 2.6: Variation of S_L/S_{L0} and η_{rad} with x_f, for equivalence ratios 0.5, 0.7 and 0.9

prediction of the behavior of a porous radiant burner. Despite not reproducing exactly the results from the reference case, the overall behavior of the interest quantities is accurate enough in order for the model to be used for the purpose of this work with sufficient confidence, as the main goal is to investigate the

trends toward optimal radiant behavior.

Thus closes the portion of the thesis dedicated to the building of the mathematical and numerical model of the Porous Radiant Burner. The section that follows provides an overview of the flame behavior within a porous burner, using the model described in these last sections.

2.3 Analysis

In the first two sections of this chapter the mathematical model of the porous burner and respective numerical implementation were introduced. The present section provides an outlook on the general behavior of porous burner's flames. To do so, illustrations of the temperature and species distributions, radiative, convective and conductive fluxes are provided. From there, basic flame characteristics are explained, as well as flame stability behavior and limit cases.

2.3.1 Reference Case

In order to study the relative influence of each and all of the parameters involved in this phenomena a reference case is defined (Table 2.2), hereby referred to as $\mathrm{Case}\ 0$, based on typical values in the literature (more in Section 3.2).

ϕ	S_v	d_{pc}	ε	ω	β	k_s	λ	$\dot{m}$	L	$T_{g,in}$	T_∞
0.85	12.5	0.15	0.75	0.65	5	12.5	1.4	$405-736$	2.0	300	300
-	cm^{-1}	cm	-	-	cm^{-1}	W/m.K	-	g/s	cm	K	K

Table 2.2: $\mathrm{Case}\ 0$ PIM characteristic parameters and operating conditions.

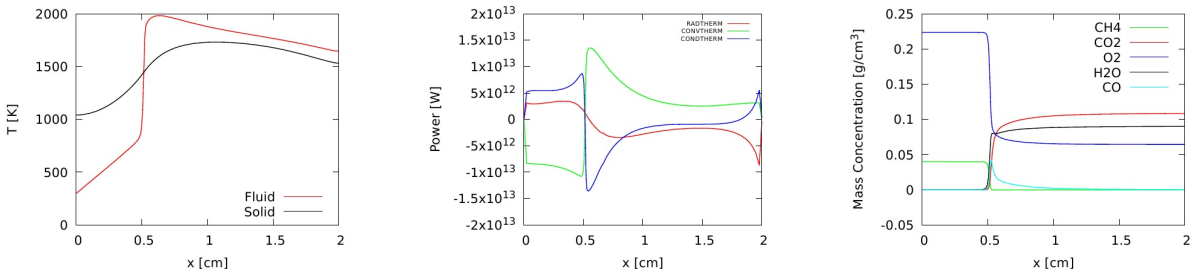

(a) (b) (c)

Figure 2.7: Flame characteristics and heat transfer for Case 0, $x_f = 0.5$ cm: (a) Gas and solid phase temperature distributions; (b) Conductive, convective and radiative heat transfer; (c) Main species mass fraction plus CO.

Figures 2.7 (a) through (c) provide descriptions of the temperatures, species and heat fluxes distributions. The flame, located at $x = 0.53$ cm, can be identified by the sharp gradients in the 3 sets of distributions. Two main regions can be discerned: the first, upstream the flame, is the preheat region. Here, the incoming gas mixture is convectively heated by the solid, until it reaches the activation temperature required for combustion to occur. This zone is characterized by strong convective heat transfer

to the gas-phase, as well as by solid conduction and radiation transfer from downstream the flame. The second region is known as the combustion zone and is where the gas temperature reaches its peak, which for some cases may be in excess of adiabatic flame temperature [4, 6, 24]. It starts at the point where the gas temperature matches that of the solid, and it is characterized by convective heat transfer from the gas mixture to the solid matrix, throughout the rest of the domain. The solid radiates and conducts both upstream and downstream, and at the outlet it radiates to the environment. Energy also leaves the system through the flue gases. Note that CH_4 is completely consumed, as would be expected for lean methane combustion, and CO is almost completely converted back to CO_2, having only a small concentration at the outlet.

2.3.2 Stability

As mentioned in Section 2.2, the fixed flame position method used does not ensure that the flame is stable. This uncertainty is due to the fact that the equilibrium position of the flame is being imposed, rather than being allowed to "naturally" converge towards it. This eliminates any awareness of the resilience toward the perturbations that inevitability exist.

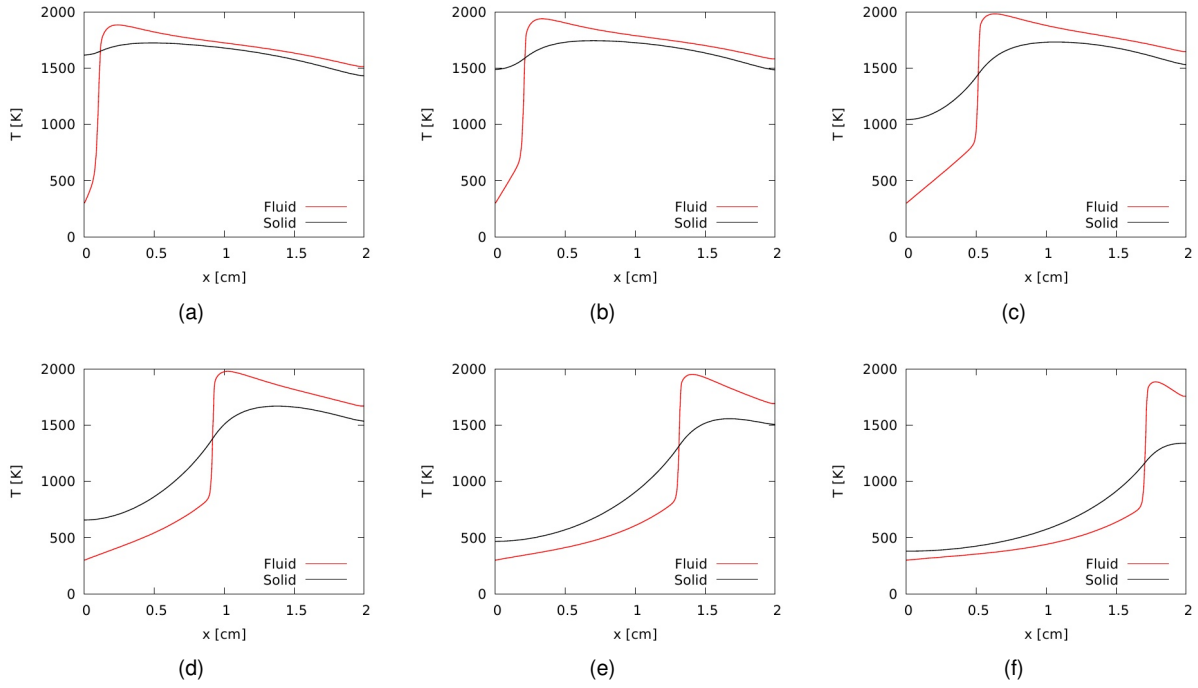

Figure 2.8: Case 0 temperature profiles for different flame positions: (a) $x_f = 0.1$ cm and $\dot{m} = 405$ g/s; (b) $x_f = 0.2$ cm and $\dot{m} = 560$ g/s; (c) $x_f = 0.5$ cm and $\dot{m} = 755$ g/s; (d) $x_f = 0.9$ cm and $\dot{m} = 779$ g/s; (e) $x_f = 1.3$ cm and $\dot{m} = 736$ g/s; (f) $x_f = 1.7$ cm and $\dot{m} = 623$ g/s.

To further understand the stability behavior of the flame in porous media combustion, an analysis of gas and solid phase temperature profiles for different flame positions is carried out. Figure 2.8 presents the temperature profiles achieved for both solid and gas phases for each flame position, as well as the corresponding mass flow rate, $\dot{m}$. It is worthy to note that the flame speed increases with flame position, up until a maximum value (in this case around $x_f = 0.8$ cm, as can be seen in Figure 2.9 (a)), decreasing

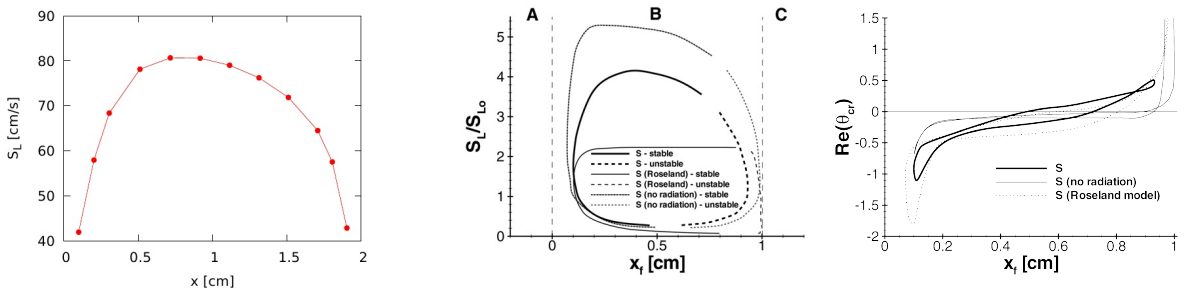

(a) (b)

Figure 2.9: Stability: (a) flame speed *versus* flame position, for $\mathrm{Case}\ 0$; (b) Stability diagrams from Mendes *et al.* [47].

after that. This trend is important in order to understand the stability condition provided by Buckmaster and Takeno [61], whereby it is defined as any flame location on which the gradient $\mathrm{d}S_L/\mathrm{d}x_f$ is positive, that is only flames on the left hand side of the flame speed peak are considered to be stable. There also is be another place where a flame can be stabilized within the porous matrix is at the outlet, but the study of surface flames lies beyond the scope of this work. More recently, Mendes *et al.* [47] have shown that it is possible to obtain stable flames after the peak in the burning velocity (Figure 2.9 (b)). It was also found that, although stable flames were observed beyond maximum burning velocity, the critical eigenvalue for these cases is very close to zero. This means that they are very close to the unstable region, being very susceptible to further perturbations not accounted in those investigation. With this in mind, it is the author's choice to stand by the more conservative criteria from [61].

Another issue regarding the stabilization of a flame within a porous media is the limit conditions for the flame not to flash-back or blow-off. As can be seen in Figure 2.8 (a), if the flow velocity decreases further, the flame will be sucked upstream and leave the domain. In this case, since the problem features the presence of a flame-trap, the flame would be quenched due to the small pores of this section. On the other hand, if the flow velocity increases past the maximum value allowed by the characteristics of the burner, the flame will blow-off, given that it is not possible to achieve the burning velocity required to reach an equilibrium state inside the burner.

As a consequence, in order to perform large-scale numerical simulations of several porous burner scenarios, it is necessary to take into account the points made in this section: ensure that the flame computed is on the left-hand side of the peak burning velocity, and that the limit cases are taken into account, namely the occurrence of blow-off and flash-back.

Chapter 3

Implementation

This chapter is dedicated to the discussion of the $Progressive\ Parametric\ Study$ employed in order to investigate the parametric trends for optimal radiant burner performance. First, an introduction on the structure of the study is given, outlining its different stages and degrees of analysis. Following, is an overview of the steps necessary for its implementation, focusing on the definition of the Parametric Domain featured in the analysis, as well as on the assembly of the $Domain\ Exploration$ code. Lastly, the result section is presented. The outcome of the outlined calculations is offered along with the discussion, in light of the stated goals of the work.

3.1 Progressive Parametric Study (PPS)

As stated in Chapter 1, the problem of multi-parametric optimization is not a trivial one. In a ”thermally” complex system like a porous burner it is unlikely that a simple parametric analysis will be sufficient to understand adequately each parameter influence on the behavior of the interest quantities, owing it to the strong non-linearities and cross-influence from other parameters caused by the multi-mode heat transfer that characterizes it.

The approach taken to tackle the issues that this optimization problem entails consists of the carrying out of a Progressive Parametric Study, which features three main stages: the first one is a $1\mathrm{D}$ Parametric Study, wherein the influence of each individual variable is investigated. For the second stage the complexity is increased, with the domain becoming two-dimensional in order to investigate possible cross-influences between all possible combinations of two parameters. The last stage of the study consists on the extension of the analysis to the full discrete $8\mathrm{D}$ Parametric Domain, where the requisites for optimal performance are investigated. A statistical analysis is performed in order to understand which parameters are driving the interest quantities and evaluate to which degree the trends established on the first and second stage of the analysis can be assumed as general trends.

The implementation of the PPS described in the previous section is presented here in two main phases. Firstly, the design of experiment approach taken regarding the choice of the parametric domain is discussed. From the input parameters introduced by the system of governing equations in Section

2.1.2, the ones that will partake in the analysis are presented, along with their adequate interval of variation and the number of different values to be considered for each parameter or, as they will be referred to henceforth, the number of points. Then, an overview of the Domain Exploration code developed is provided. The goal of this code is to allow the computation of a large number of cases in an autonomous fashion, taking into account details like the routine employed for the computation of each individual case, the provision of adequate starting estimates to POROUSN and the decision method employed when choosing the next case to be computed. This section closes off with a discussion on the time management measures taken in order to make the calculations more time efficient and on the evaluation routine carried out in order to assess stability limit cases, like the ones discussed in Section 2.3.2, occurrence of convergence failure and simulation/case time-out.

3.2 Design of Experiment

In order to study the behavior of the objective quantities it is necessary to define the realm of possible cases on which to perform the investigations. This set of cases constitute the Parametric Domain, which is the discrete N-Dimensional space that defines all the possible combinations of the problem parameters being studied at a given stage of complexity, within the defined bounds for each parameter.

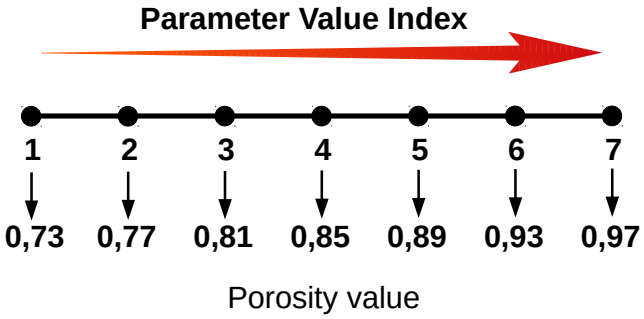

Figure 3.1: Example of the 1D parametric domain for the variation of the solid porosity, ϕ. Values from Table 3.1.

The definition of this domain is presented in Table 3.1. There are 12 main parameters that are required as inputs to the model described in Section 2.1.2, however it is considered 8 of them for the definition of the Parametric Domain (the ones in first 8 columns from Table 2.2). The mass flow rate and the burner length are also studied, although not in the same intensive way as these 8 main parameters. The temperatures both of the incoming gas ($T_{g,in}$) and of the environment (T_{∞}) are not taken into account. More on these parameters is discussed in later paragraphs.

The lower and higher bounds for each of the main parameter are defined, along with the number of points that are considered on that axis, which are uniformly distributed (Table 3.1). The choice of bounds for each parameter is guided by the typical values present in the available literature. The goal when defining each range of variation is to encompass, as much as possible, the full realm of possibilities,

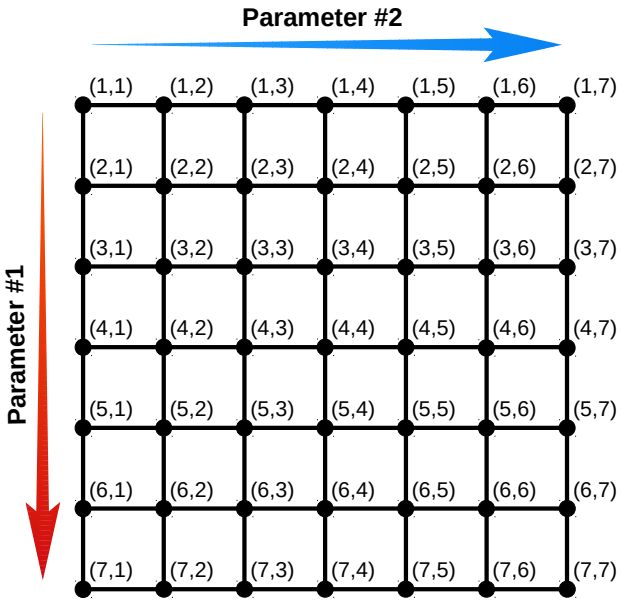

Figure 3.2: Example of a 2D parametric domain.

whilst not foregoing the physical reasonability of it.

Porosity: Diamantis and Goussis [36] worked between $0.8 - 0.9$, whilst Mital and Viskanta [33] used values in the range of $0.8 - 0.87$. Sathe and Tong [49] performed their studies with $\phi = 0.95$.

Specific Surface Area: The literature provides wildly varying values for this parameter. Values ranging from $2\ \mathrm{cm}^{-1}$ to $40\ \mathrm{cm}^{-1}$ are reported [47, 63].

Characteristic Pore Diameter: Younis and Viskanta [14] report pore diameters in the order of $0.03 - 0.15\ \mathrm{cm}$. Mendes' [63] work used values in the range of $0.06 - 0.15\ \mathrm{cm}$.

Emissivity: Typical values range between 0.7 and 0.85 [36, 47].

Scattering Albedo: Values reported in the literature go from 0.5 to 0.88 [4, 49]

Extinction Coefficient: Sathe and Tong [49] report studies with $\beta = 0.2 - 2\ \mathrm{cm}^{-1}$, while Diamantis and Goussis [36] reports results that vary between 1.15 and $50\ \mathrm{cm}^{-1}$. Hsu and Matthews [3] report that values in the range of $1 - 10\ \mathrm{cm}^{-1}$ are representative of typical ceramic foams.

Bulk Solid Thermal Conductivity: Values in the literature range from $1 - 2.6\ \mathrm{W/m.K}$ [36] to $10 - 100\ \mathrm{W/m.K}$ [49].

Excess Air Ratio: Typical values of λ for this type of burners are in the range of $1.1 - 1.8$, as reported by Keramiotis *et al.* [37] and Trimis and Durst [64].

With regard to the "mesh" detail of the Parametric Domain, a smaller number of points is considered for the $8\mathrm{D}$ domain than for the $1\mathrm{D}$ and $2\mathrm{D}$, for computational time reasons. In order to compute one $8\mathrm{D}$

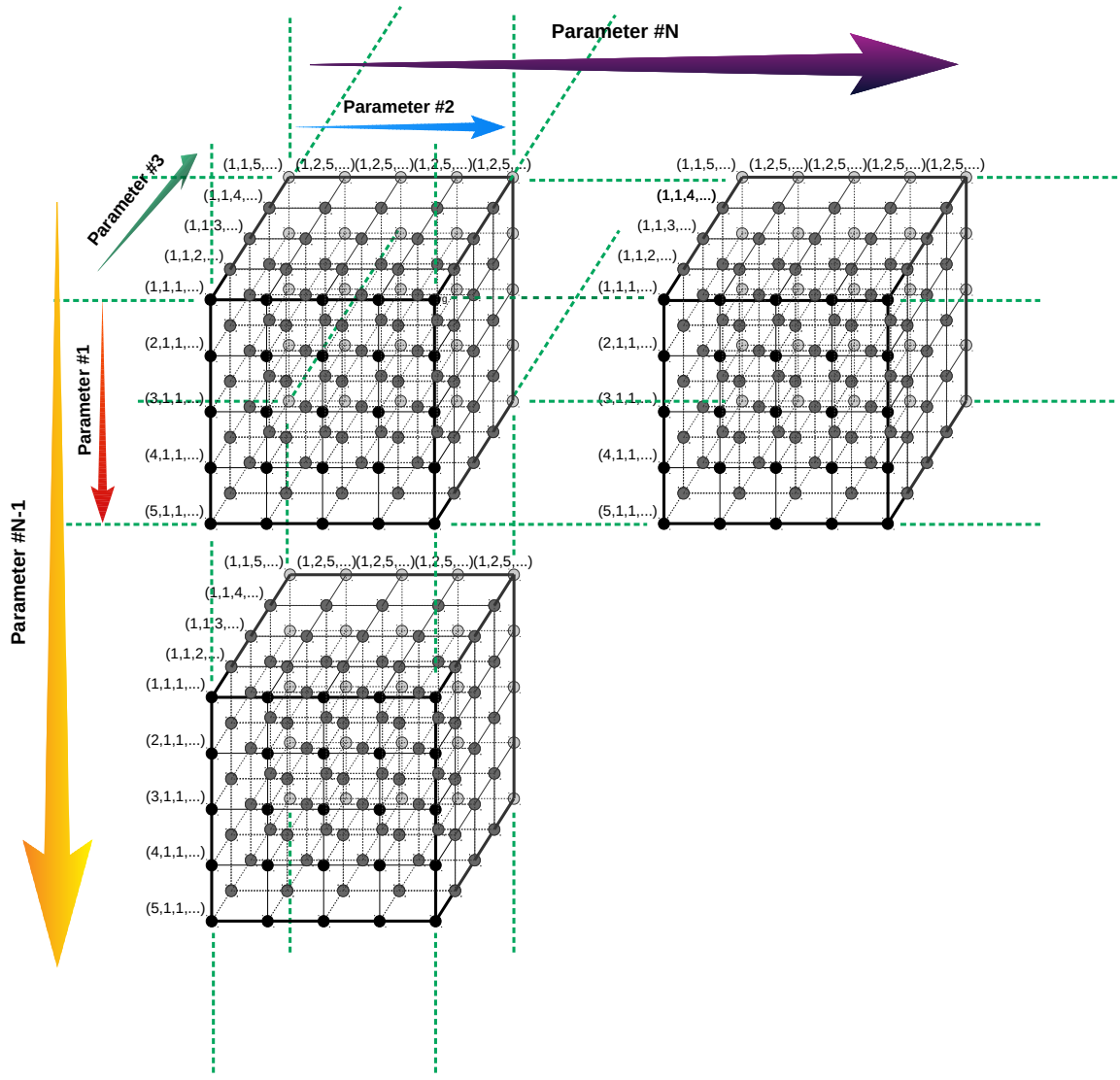

Figure 3.3: Simplified example of an N-D parametric domain.

	1D & 2D			8D		
	Low Bound	High Bound	Points	Low Bound	High Bound	Points
ϕ	0.73	0.97	7	0.75	0.95	5
S_v [cm^{-1}]	2.0	23.0	7	5.0	20.0	5
d_{pc} [cm^{1}]	0.05	0.25	7	0.07	0.23	5
ε	0.55	0.95	7	0.55	0.95	5
ω	0.3	0.9	7	0.3	0.9	5
β [cm^{-1}]	0.5	9.5	7	1.0	9.0	5
k_s [W/mK]	0.3	24.7	7	5.0	20.0	5
λ	1.0	1.8	7	1.2	1.6	5

Table 3.1: Parametric domain for the different stages of the progressive parametric study.

Parametric Domain with 5 points, it may be necessary to compute up to $5^8 = 390\,625$ different cases. For 7 points, this number increases dramatically to $7^8 = 5\,764\,801$, which would not be possible to compute

within reasonable time.

		Input Power, Q_{comb} (kW/m^2)		
		800	1000	1200
Length, L (cm)	1.0	$1D/2D$	$1D/2D/8D$	$1D/2D$
	2.0	$1D/2D/8D$	$1D/2D/8D$	$1D/2D$
	3.0	$1D/2D$	$1D/2D/8D$	$1D/2D$

Table 3.2: Power/Length (PL) Pairs.

Different sets of $1\mathrm{D}$ and $2\mathrm{D}$ Parametric Studies are computed for different combinations of power input, Q_{comb}, and burner length, L. The PL pairs that are considered at each stage are presented in Table 3.2. The analysis of Q_{comb} is performed separately from the main parameters because of its significant impact on flame stability, due to $\dot{m}$ being defined as function of the input power and the excess air ratio, $\dot{m} = f\left(Q_{comb}, \lambda\right)$, thus oscillating significantly with Q_{comb}. It is instead treated as a secondary parameter in the study, investigated only on its general impact, as is done for the burner length, L, assigned to this category due to some $\mathrm{POROUSN}$ code limitations regarding this parameter.

The inlet gas and environment temperatures, $T_{g,in}$ and T_{∞}, one the other hand, are situational and depend on the intended use, which for a radiant burner can range from a household heating application to a industrial furnace. For this reason it is taken at a constant value, $T_{\infty} = 300K$. As for the gas mixture inlet temperature, it is also considered to be at environment temperature ($T_{g,in} = T_{\infty}$), as to change this temperature the fuel mixture would need to be heated, altering the energy efficiency balance of the problem.

The baseline case for this study is $\mathrm{Case}\ 0$, presented in Section 2.3. It lies approximately at the mid point of the $8\mathrm{D}$ Parametric Domain defined in Table 3.1. This case is defined with the goal of existing at the center of stable burner cases' domain, so that variations to either side are able to produce, as much as possible, solutions that correspond to stable existing flames.

Having the design of experiment details clear, it is possible to construct the code that is responsible for performing the case-to-case simulations.

3.3 Code Structure

The $\mathrm{Domain\ Exploration}$ code goal is to autonomously perform the calculations necessary to cover the Parametric Domain under analysis at each given stage of the $\mathrm{Progressive\ Parametric\ Study}$. This driver code is programmed in MATLAB, in conjunction with a set of sh scripts that provide the interface between the $\mathrm{POROUSN}$ code ($\mathrm{FORTRAN}\ 77$) and the driver. The code uses a Systems of Decision approach in order to manage the large-scale computation of inter-dependent burner cases, for 8 simultaneously varying parameters, and with the capability of dealing with non-linear convergence patterns,

dynamic restart estimate assignment and effective case sequencing. The application code also included time management measures, developed to make more efficient use of computational time.

As stated, for the most complex Parametric Domain considered, up to a few hundred thousand individual cases may be computed for a single Power/Length pair . In order to deal with such large number of cases it is necessary to develop an algorithm that allows for the smooth, autonomous calculation of these cases without allowing that a failure in convergence to foil the whole process.

The algorithm is conceptually divided in two main parts/levels (Figure 3.4): the lower level corresponds to the section that deals with the computation of each individual case. It performs the routine necessary to attain case convergence and runs an evaluation of the outcome of the calculation. The upper level is tasked with the management of the calculation flow of the code, by deciding which case is to be calculated after each "iteration", dealing with the input/output of $\mathrm{POROUSN}$ and keeping track of the calculations and evaluations that have already been performed.

3.3.1 Individual Case level

The computation of each individual case requires two main steps to be performed: first, it is necessary to perform the fixed flame calculation of the Parametric Domain point in question, ignoring Q_{comb} and $\dot{m}$ at this stage. The solution of this intermediate is then used as starting estimate for the $\mathrm{Mass\ Flow\ Interface}$, in order to achieve the value of $\dot{m}$ that corresponds to the Q_{comb} and λ of said case. The separate computation of the parameter value change and the required mass flow is done in the interest of reducing the computational time for each case, since $\mathrm{POROUSN}$ converges faster when the changes from the restart estimate are made incrementally.

Each individual case is identified by its case ID, which corresponds to its coordinates in the Parametric Domain outlined in Section 3.2. The routine consists on the following steps:

1 - A first call to $\mathrm{POROUSN}$ is made, in order to obtain a fixed flame solution for the corresponding burner setup (case);

2 - Evaluation of the success status of the simulation is made: if the result is negative $\mathrm{End\ of\ Case}$ is declared and the algorithm gives control back to the Case Management level; If the result is positive, solution is fed to the next phase. In both cases available solution files are saved according to simulation ID and error status;

3 - If the first call is successful, its solution is used as starting estimate for the $\mathrm{Mass\ Flow\ Interface}$, where the required mass flow rate (according to $\dot{m} = Q_{comb}/Y_{CH4}LHV_{CH4}$), is iteratively computed.

4 - Evaluation of the success status of the $\mathrm{Interface}$ call is made. Solutions are saved as described in point 2.

The evaluation of the success status of a case consists on the de-codification of key $\mathrm{POROUSN}$ output files, and its result provides, in case of failure, the specification of which type of failure has occurred.

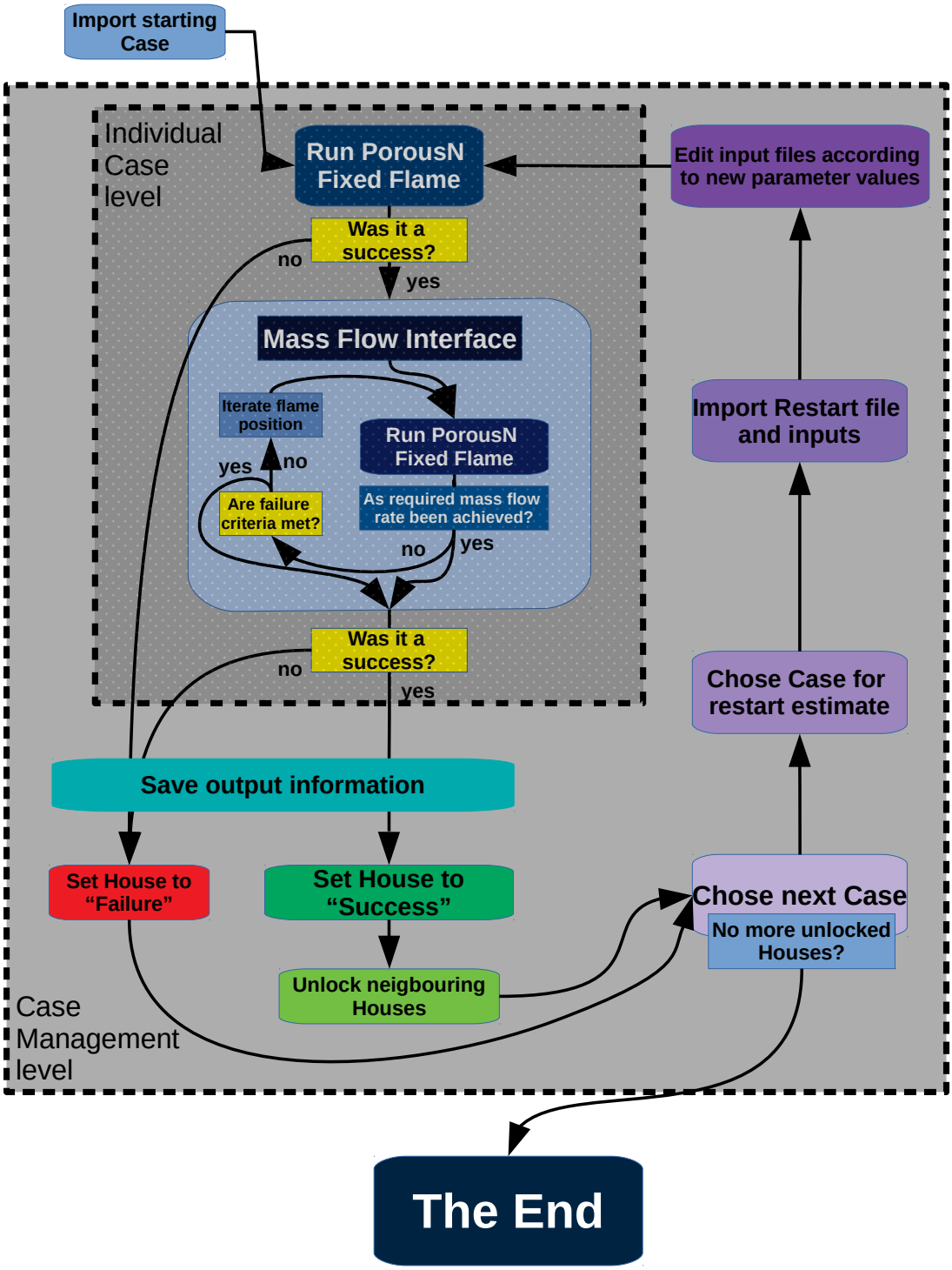

Figure 3.4: Flowchart of the Domain Exploration code.

The possibilities include inability to converge, time-out or one of the stability limit situations described in Subsection 2.3.2.

Besides informing on the solution of the present case, the evaluation of a case is also the means

through which new cases are unlocked to be calculated. More on this is explained in the following paragraphs.

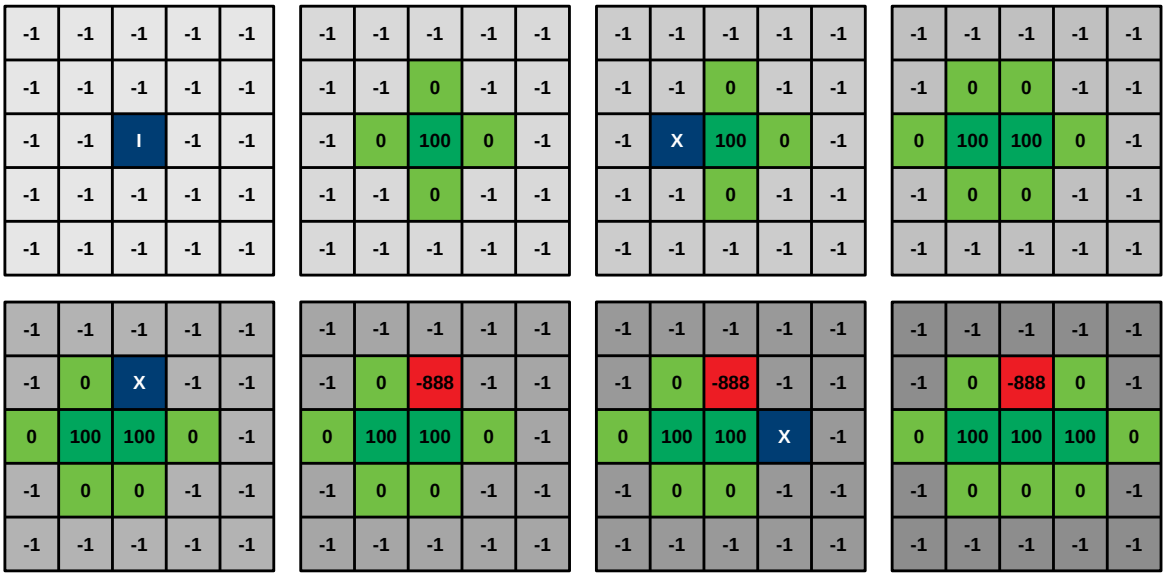

Figure 3.5: Evolution of an example of a 2D parametric domain over the study of 4 cases: I - initial case; X - current case. Blue houses correspond to the case being computed at a given time, light green to the avaliable houses, green to the successful computed cases and red to the cases that failed.

3.3.2 Case management Level

In order to provide a grounding structure for the calculation flow of the Parametric Domain, a domain map is defined. It consists of a N-dimensional matrix, being N the number of parameters under analysis. Each dimension is divided into P points, corresponding to the number of different values considered for each parameter. Each coordinate set of the matrix, taking the form of $C = (x_1, x_2, ..., x_N)$, corresponds to a different burner case, with its different defining parameter values.

Figure 3.5 illustrates a possible progression of the case computation: at the initialization phase all houses are set to -1, signaling to the algorithm unavailability to be calculated. The process starts by prescribing a starting point, $\mathrm{Case\ I}$, for which the solution is already known. This case is computed once more (going into the $\mathrm{Individual\ Case}$ routine) allowing the algorithm to unlock the neighboring houses that satisfy $||C_I - C_{neighbour}|| \leq 1$, by setting them to $\mathbf{0}$ and the initial case to $\mathbf{100}$. This is done due to the fact that a close restart estimate is necessary for the cases to converge: once a successful case is computed it becomes a viable starting estimate, which means that the cases in the vicinity meet the conditions to be calculated. In the event of failure in the computation a negative code is assigned to the corresponding house, specifying the type of failure that occurred (Table 3.3), and no new neighboring houses are unlocked.

The following step is to select from the unlocked houses ($\mathbf{0}$s) the one that is to be calculated next. The strategy employed for the selection of cases is $\mathrm{First\ Come\ First\ Served}$. Then, an adequate case is selected to be the restart estimate. The criteria used was that this case must be within a certain distance

from the case that is to be computed, that is: $\|C_{current} - C_{estimate}\| <= 1$. The goal of this condition is, as mentioned earlier, to assure that the restart estimate is close enough to the current case, so that convergence can be as speedy as possible.

Once the choices for the following case are made, the input files are edited to match the parameter values of the new case and fed, along with the restart estimate, to the code. control is given to the $\mathrm{Individual\ Case}$ level, restarting the cycle.

3.3.3 Evaluation routine and time management

Two important aspects of the development of the $\mathrm{Domain\ Exploration}$ code still remain to be discussed. As stated, stability limits and overall failures in convergence must be taken into account in order to assure the smooth flow of the code. Also, it has been found that most of the cases that are successfully computed take a short time to converge. This is, when a simulation takes more than a given time it is most likely to fail. In order to take advantage of this fact, a trigger was included on the code so that when this time limit is exceeded it aborts the simulation, saving computational time.

From there control is passed to the evaluation routine. It is the goal of the evaluation routine to assess the success status of the simulation and check the cause of failure if it is not successful. The outcomes of the evaluation are presented in Table 3.3.

Occurrence	Evaluation	Description
Case Success	100	Case computation is successfully completed.
Flash-back	-414	Fixed flame temperature point left the domain. Assumed Flash-back.
No Convergence	-666	$\mathrm{POROUSN}$ did not converge.
POROUSN Time-out	-777	Mass flow iteration took too long. Assumed near boundary (Flash-back).
Blow-off	-888	Mass flow rate diverged for 3 straight iterations. Assumed Blow-off.
INTERFACE Time-out	-999	Numerical issues in the iterative process led to infinite loop.

Table 3.3: Possible occurrences of success and failure within the evaluation routine.

The structure of the $\mathrm{Domain\ Exploration}$ is fully defined, along with the Parametric Domain and conditions for the experiments. What follows is the presentation of the studied cases and a detailed analysis and comparison of the results obtained across levels of complexity.

Chapter 4

Results

The results of the investigations undertaken in the Thesis are presented in this chapter starting with the presentation of the reference case and baselines based on their Power/Length combination. Then the results of the $1\mathrm{D}$ *Parametric Study are presented, for several input powers and burner lengths. The* 2^{nd} *stage of the* PPS.

4.1 Introduction

The present section delves into the outcomes of the investigations carried out in the pursuit of this works goals. Over *1 million* different burner configurations/operating conditions were computed, for a total over 30000 CPU hours. The simulations were ran on multiple machines at the same time, one with an AMD Ryzen 7 2700x eight-core processor with $1.8\ \mathrm{GHz}$ frequency and other three with Intel Xeon E5420 four-core processor, $2.5\ \mathrm{GHz}$, both in hyper-threading, with the full set of runs taking two months to complete.

Figure 4.1: Three batches of simulations running simultaneously on different machines, at LASEF.

First and foremost, it is necessary to define a set of center/baseline conditions to compare the obtained results to. These baselines are defined by the set of 8 main parameters that is prescribed for $\mathrm{Case}\ 0$, presented in Table 2.2. The way in which they differ lies in their characterization with regard to input power (Q_{comb}) and burner length (L). Each of these baseline cases serves as the starting point for a set of Parametric Studies, as presented in Table 3.2. The values of the interest quantities of the problem, η_{rad} and $T_{s,max}$, for different combinations of input power and burner length are given in Table 4.1.

		Input Power, Q_{comb} $\left(kW/m^2\right)$					
		800		1000		1200	
		$\eta_{rad}\,(\%)$	$T_{s,max}\,(K)$	$\eta_{rad}\,(\%)$	$T_{s,max}\,(K)$	$\eta_{rad}\,(\%)$	$T_{s,max}\,(K)$
Length, L (cm)	1.0	20.79	1561	17.83	1562	14.56	1527
	2.0	21.82	1723	**19.33**	**1738**	17.41	1746
	3.0	22.05	1788	19.56	1805	17.69	1817

Table 4.1: Baseline Conditions for several Power/Length Pairs.

The reference case for this study is characterized by a radiant efficiency of $\eta_{rad} = 19,33\%$ and maximum solid temperature of $T_{s,max} = 1738\ K$, and corresponds to an input power of $1000\ \mathrm{kW}$ and burner length of $2.0\ \mathrm{cm}$ (highlighted in Table 4.1). This choice is grounded in stability concerns, standing in the middle of the stability domain. This mid-point is derived through an experimental heuristic, developed with the observation of the flame behavior across several different cases.

For the $1\mathrm{D}$ and $2\mathrm{D}$ phases of the $\mathrm{Progressive\ Parametric\ Study}$, 9 sets of Parametric Studies, for different combinations input powers and burner lengths, are computed, in order to add understanding on how does each parameter's impact vary with different burner length and power.

4.2 One-Dimensional Parametric Study

Here the impact of the parameters in the interest quantities is assessed. A qualitative analysis of the behavior of each parameter is given, along with graphic representation of the cases studied in the output domain, in order to grasp towards which direction does each parameter swing the interest quantities. Then the impact of each of the parameters is quantified, with the aid of 2 evaluating quantities: the ratio of coefficients of variation (c_{v_r}), between each quantity and the parameter in question, and the trend direction angle (α_{trend}). The goal of the c_{v_r} (equation 4.2) is to quantify the magnitude of the impact of each parameter, whilst the objective of the trend direction angle is to ascertain if the evolution of a given parameter is direct or inverse, that is, if an improvement is made in one of the quantities leads to an improvement or to a penalty in the other interest quantity.

The ratio of coefficient of variation, c_{v_r}, is defined as:

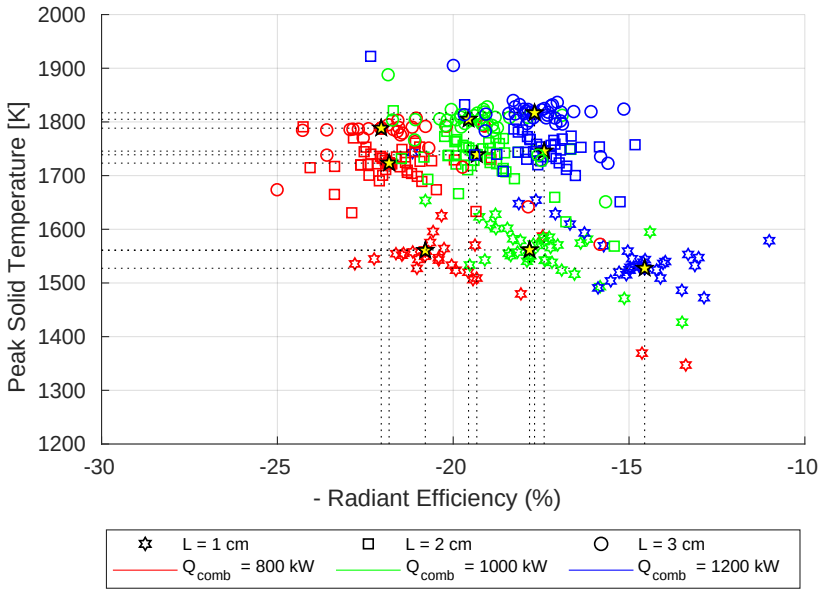

Figure 4.2: Cases computed for the $1\mathrm{D}$ stage according to the input power and burner length.

$$c_{v_r}\left(Q_{interest}/Parameter_i\right) = \frac{c_v\left(Q_{interest}\right)}{c_v\left(Parameter_i\right)} \times 100 \tag{4.1}$$

where $Q_{interest}$ is one of the interest quantities and $Parameter_i$ is each of the 8 problem's parameters. The coefficient of variation, the standard deviation and expected value for the distribution of each quantity are:

$$c_v = \frac{\sigma}{\mu}, \qquad \sigma = \sqrt{\frac{1}{N-1}\sum_i^N \left(x_i - \mu\right)^2}, \qquad \mu = \frac{\sum_i^N x_i}{N} \tag{4.2}$$

where N is the total number of cases taken into account for the calculation of a given c_{v_r}.

The trend angle direction angle is derived from a linear fit, performed over the results of the $1\mathrm{D}$ parametric study of each parameter, with each case point placed on the Output Domain, a $2\mathrm{D}$ plane defined by $T_{s,max}$ vs $-\eta_{rad}$, where the radiant efficiency is examined as negative for analysis purposes. It follows that for a parameter with a direct trend, α_{trend} belongs to either the 1^{st} or the 3^{rd} quadrant (with the parameter value increasing away from the origin of the Output Domain or towards it, respectively), while an inverse trend is represented by a trend direction angle in the 2^{nd} or 4^{th} quadrants, likewise increasing in the direction which the angle points.

4.2.1 Qualitative Analysis

Figure 4.2 presents all of the computed 1D cases on the domain defined by the interest quantities ($T_{s,max}$ *vs.* $-\eta_{rad}$). It can be can be observed that the higher radiant efficiencies are achieved by the lowest input powers, consistent with what is reported in the literature [37, 38]. An increase burner length, on

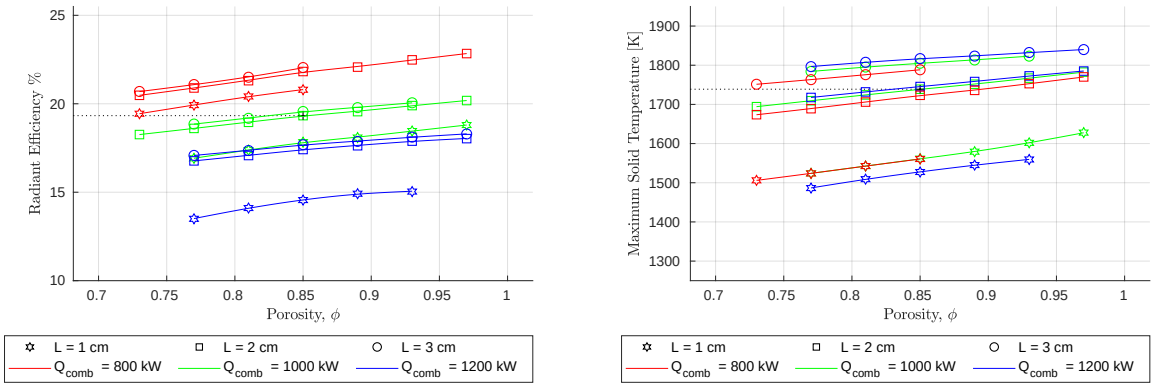

(a)

(b)

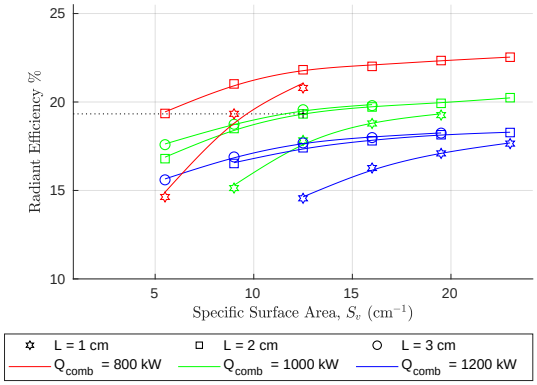

(c)

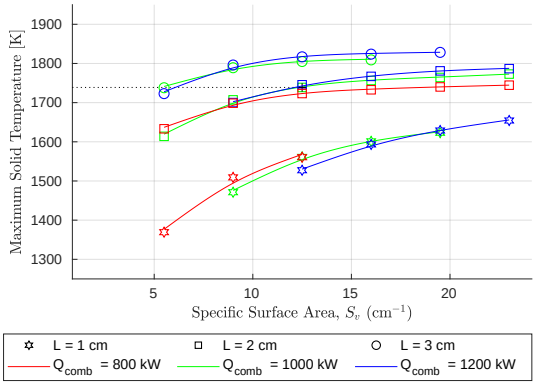

(d)

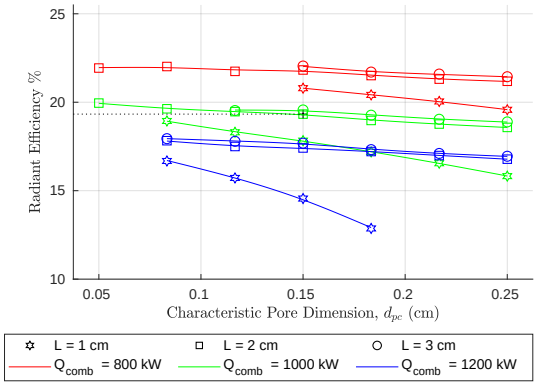

(e)

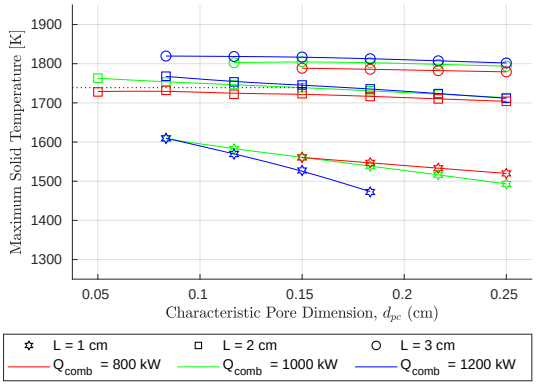

(f)

Figure 4.3: Interest quantities *versus* geometric parameters.

the other hand, leads to an increase in both radiant efficiency and peak solid temperature.

Upon observation of Figure 4.3 some conclusions can be drawn regarding the behavior of the geometric parameters, ϕ, S_v and d_p. Regarding the porosity, radiant efficiency increases with an increase in ϕ. This increase is mirrored by the increase in maximum solid temperature, making that an improvement in one objective quantity leads to a penalty in the other. This trend stand across all values of Q_{comb}

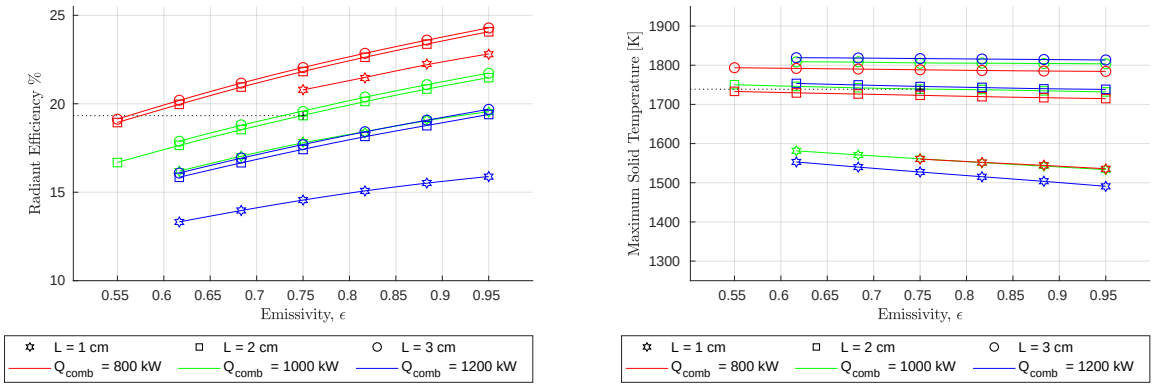

(a)

(b)

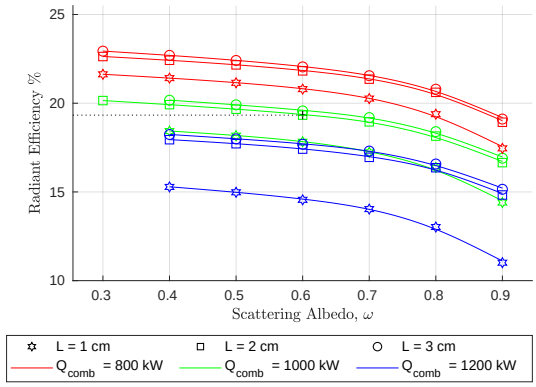

(c)

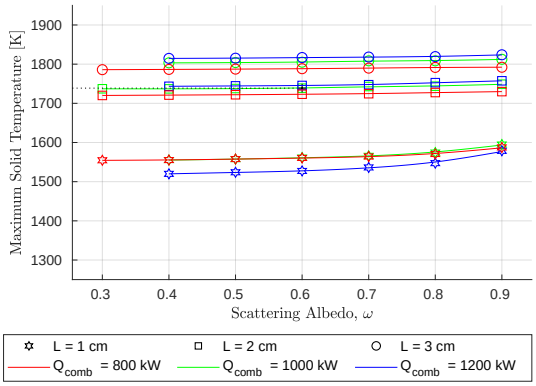

(d)

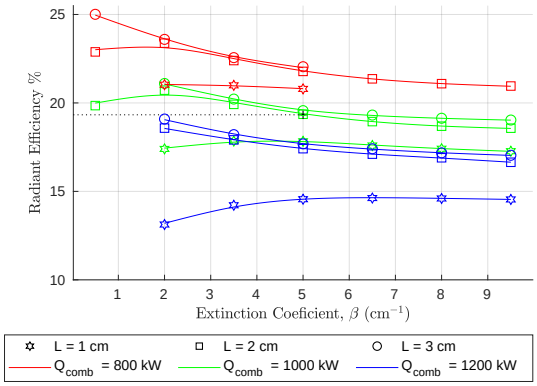

(e)

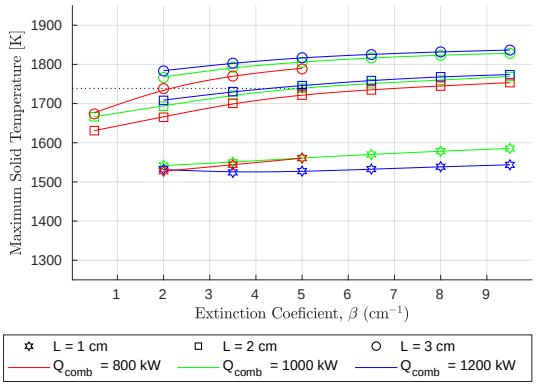

(f)

Figure 4.4: Interest quantities *versus* radiative parameters.

and L. The specific surface area, S_v, also presents an inverse relation between both interest quantities, with the trend common to η_{rad} and $T_{s,max}$ being that an increase in surface area leads to an increase in the quantities, whilst a decrease leads to a sharp growing decrease. Lastly, with regard to the pore diameter one can see that an increase in this quantity leads to a slight decrease in radiant efficiency. Once more, this trend mimics the other geometric parameters, in that the maximum solid temperature

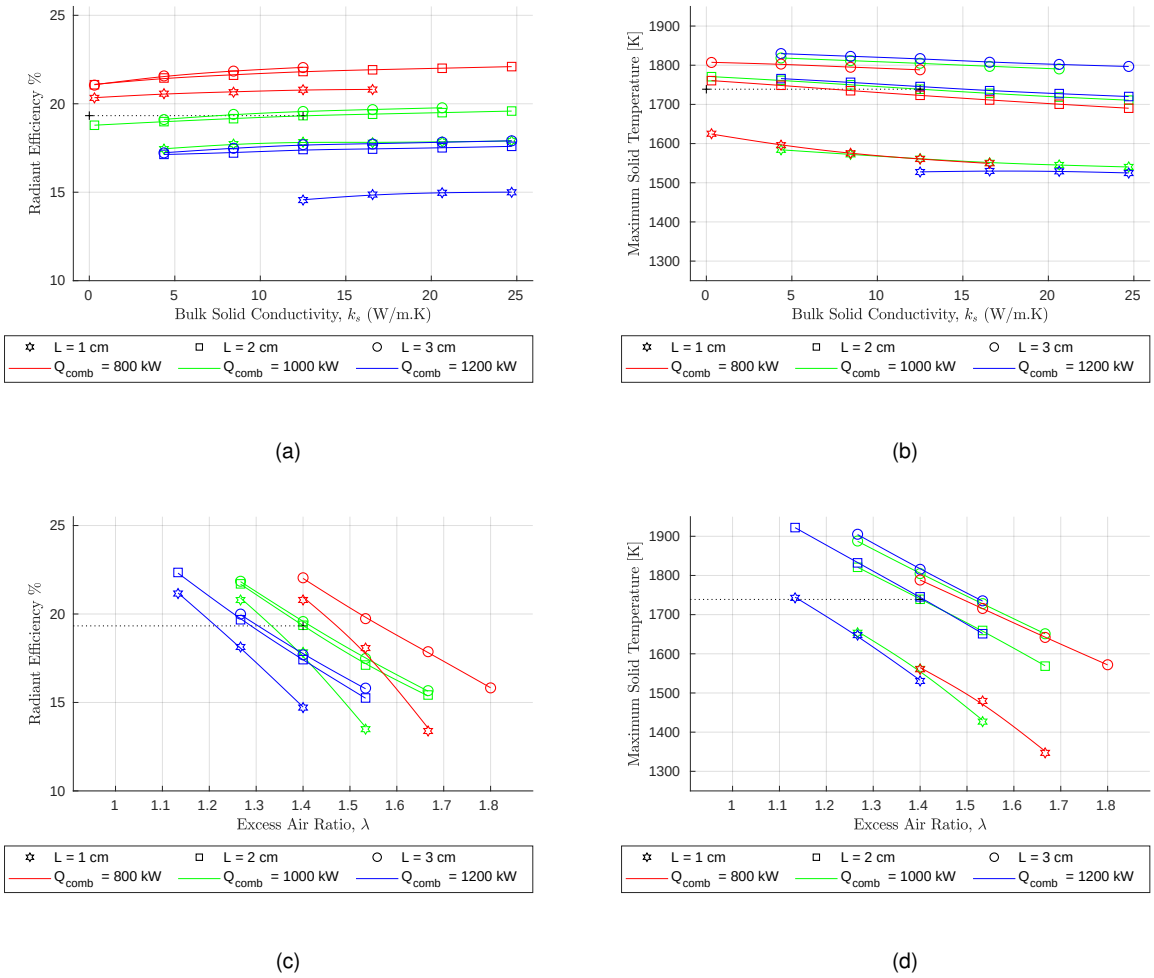

Figure 4.5: Interest quantities *versus* k_s and λ.

also decreases. This parameter has a mild impact on the interest quantities, except for the case with $L = 1.0$ cm and $Q_{comb} = 1200$ kW, where the decrease in the interest quantities is more substantial.

Moving on to the radiative parameters, ε, ω and β, the following behaviors can be found: the porous media emissivity has a positive impact impact on the radiant efficiency, whilst having a slight negative impact on the maximum solid temperature. It is for the lower values of the scattering albedo that the radiant efficiency is higher. Also, for the higher range of ω it is observed a significant drop in η_{rad}. Maximum solid temperature is stagnant in the lower range, rising slightly for the upper values of the albedo, more significantly for $L = 1$ cm. The dip in radiant efficiency is also more pronounced for this burner length. Lastly, higher values of the extinction coefficient produces decreasing radiant efficiency and increasing in maximum solid temperature, across all powers and lengths. The lower section of β is not as straightforward: for burner length equal to 3cm, radiant efficiency increases with the decrease of the extinction coefficient. For $L = 2$ cm, however, an inflection point emerges, with a maximum for η_{rad} at $\beta = 2.0$ cm^{-1}. This trend is not observable for $Q_{comb} = 1200$ kW due to the fact that the point that would correspond to $\beta = 1.0$ cm^{-1} is not stable. For the shorter burner length there is a slight increase in η_{rad} for the lower power, an inflection curve with maximum on the baseline case for the mid range Q_{comb} and a downward trend for the higher input power. Like in the case of the geometric properties, the

radiative parameters of the media also presents consistent relationships between the interest quantities, all presenting a direct relationship between the interest quantities. The only exception is the lower range of the extinction coefficient, where the behavior of the curves is more sensitive to the variation of Q_{comb} and L.

With regard to the bulk solid thermal conductivity, it is observable in Figure 4.5 (a) that high k_s produces increases in radiant efficiency and decrease in maximum solid temperature. However this effect is not very pronounced. The only outlier to this soft impact is the solid temperature for the lowest power and lowest length, that suffers a sharper increase for the lower values of k_s. Finally, lower excess air (more fuel percentage) produces higher radiant efficiencies, along with an equally sharp increase in the maximum solid temperature (Figure 4.5 (b)).

4.2.2 Quantitative Analysis

Attention is now given to the values of c_{v_r} and α_{trend}. Table 4.6 presents the results of these quantities for every parameter and Power/Length combination. The averages across constant Q_{comb} and L are also provided. For each parameter and Power/Length pair, the evaluating quantities ($c_{v_r}\,(\eta_{rad})$, $c_{v_r}\,(T_{s,max})$ and α_{trend}) are highlighted, being the more saturated color coded according to their relative distribution. The results presented confirm the trends established earlier, providing a condensed summary of the impact quantification of each of the problem's parameters.

4.3 Two-Dimensional Parametric Study

The purpose of this section of the work is to understand the interactions between the problem's parameters, and whether the behaviors ascertained in Section 4.2 are reiterated when two parameters are varied simultaneously or if, instead, the variation of one leads to a change in behavior of the other.

These interactions are studied through the examination of the Output Image of the cases covered by both parameters' ranges: if the parameters are linearly independent, the shape of the curve of a given parameter is maintained across all values of the other, with the Output Image appearing as the shape defined by the linear combination of both $1\mathrm{D}$ curves and the c_{v_r} remaining constant. Instead, if the parameters produce a cross-influence effect on each other the shape of the $1\mathrm{D}$ curves becomes distorted and the c_{v_r} is altered.

A total of 28 combinations of parameters are computed, for each of the 9 combinations of Power/Length, which can be consulted in length in Appendix A.1. The upcoming subsection delves into the parametric combinations for the reference PL case, $Q_{comb} = 1000\ \mathrm{kW}$ and $L = 2.0\ \mathrm{cm}$, establishing the standard behavior of the parametric interaction. Then, the influence of input power and burner length is studied, focusing on the general impact on η_{rad} and $T_{s,max}$ and on its effect on the parametric $2\mathrm{D}$ combinations. The section closes with a brief summary of main conclusions.

		CV ratio (η_{rad}/Parameter)				CV ratio ($T_{s,max}$/Parameter)				Trend Direction Angle -η_{rad} vs. $T_{s,max}$				
	Q_{comb} (kW) / L (cm)	800,00	1 000,00	1 200,00	Average	800,00	1 000,00	1 200,00	Average	800,00	1 000,00	1 200,00	Average	
Solid Porosity	1,0	44,77	44,98	58,82	49,52	23,47	28,36	25,43	25,75	113,41	107,45	110,88	110,58	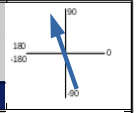
	2,0	38,65	35,34	32,08	35,35	19,71	17,79	16,77	18,09	113,12	110,81	108,31	110,75	
	3,0	41,50	32,97	30,01	34,83	13,79	11,36	10,24	11,79	122,11	118,46	116,28	118,95	
	avg	41,64	37,76	40,30	39,90	18,99	19,17	17,48	18,55	116,21	112,24	111,83	113,43	
Specific Surface Area	1,0	45,37	32,76	32,33	36,82	17,20	13,52	13,51	14,74	119,31	115,42	112,92	115,88	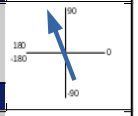
	2,0	11,96	14,50	11,54	12,67	5,33	7,50	5,77	6,20	115,99	110,33	109,11	111,81	
	3,0	24,26	12,55	13,96	16,92	11,36	4,36	5,47	7,06	113,07	118,26	113,40	114,91	
	avg	27,20	19,94	19,28	22,14	11,30	8,46	8,25	9,34	116,12	114,67	111,81	114,20	
Characteristic Pore Diameter	1,0	11,98	17,62	33,99	21,20	5,28	7,37	11,76	8,14	-62,79	-65,05	-64,19	-64,01	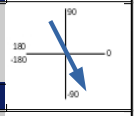
	2,0	3,07	5,33	5,79	4,73	1,20	2,10	3,14	2,15	-60,73	-64,08	-72,44	-65,75	
	3,0	5,51	5,37	6,12	5,67	1,05	0,88	1,03	0,99	-40,71	-39,67	-44,63	-41,67	
	avg	6,85	9,44	15,30	10,53	2,51	3,45	5,31	3,76	-54,74	-56,27	-60,42	-57,14	
Emissivity	1,0	39,82	43,95	41,24	41,67	6,76	7,23	9,53	7,84	-145,25	-140,60	-125,96	-137,27	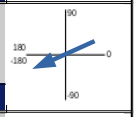
	2,0	44,39	46,78	47,04	46,07	2,03	1,93	2,08	2,01	-168,13	-167,89	-165,89	-167,30	
	3,0	44,09	45,39	47,04	45,50	1,01	0,75	0,77	0,85	-173,81	-175,44	-174,54	-174,60	
	avg	42,76	45,37	45,10	44,41	3,27	3,30	4,13	3,57	-162,40	-161,31	-155,46	-159,72	
Scattering Albedo	1,0	20,07	30,53	39,91	30,17	2,06	3,25	4,92	3,41	24,56	29,53	38,47	30,85	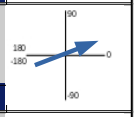
	2,0	16,77	17,88	23,66	19,44	0,57	0,71	1,08	0,79	8,89	11,71	15,18	11,93	
	3,0	17,13	22,09	23,15	20,79	0,38	0,66	0,64	0,56	5,67	8,97	9,58	8,07	
	avg	17,99	23,50	28,91	23,47	1,00	1,54	2,21	1,59	13,04	16,74	21,08	16,95	
Extinction Coefficient	1,0	1,42	2,79	8,37	4,19	2,52	2,17	0,95	1,88	81,91	61,98	171,90	105,26	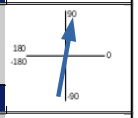
	2,0	6,54	6,16	8,40	7,03	4,07	3,34	2,92	3,44	68,78	66,70	63,60	66,36	
	3,0	7,97	8,25	8,86	8,36	4,11	2,60	2,25	2,99	65,82	58,97	56,31	60,37	
	avg	5,31	5,73	8,54	6,53	3,57	2,70	2,04	2,77	72,17	62,55	97,27	77,33	
Bulk Solid Thermal Condutivity	1,0	1,23	1,80	4,81	2,61	2,49	2,06	0,55	1,70	-96,41	-100,83	-176,39	-124,54	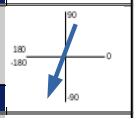
	2,0	2,35	2,13	1,91	2,13	2,11	1,81	1,91	1,94	-103,99	-102,81	-99,95	-102,25	
	3,0	2,43	2,60	2,71	2,58	0,57	1,20	1,33	1,03	-133,16	-112,61	-109,73	-118,50	
	avg	2,00	2,18	3,14	2,44	1,72	1,69	1,26	1,56	-111,19	-105,41	-128,69	-115,10	
Excess Air Ratio	1,0	247,44	221,92	170,20	213,19	84,74	77,40	61,53	74,55	-59,04	-60,96	-62,36	-60,78	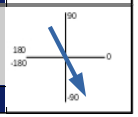
	2,0	106,08	126,47	126,20	119,58	38,44	54,25	50,32	47,67		-66,34	-65,65	-43,99	
	3,0	130,73	121,94	123,44	125,37	51,66	48,96	49,06	49,89	-63,85	-65,61	-66,94	-65,47	
	avg	161,42	156,77	139,95	152,71	58,28	60,20	53,64	57,37	-40,96	-64,30	-64,98	-56,75	

Figure 4.6: Overview of the individual effect of each parameter on the interest quantities, for different combinations of Q_{comb} and L, featuring the coefficients of variation ratios between $-\eta_{rad}$ and $T_{s,max}$ and each parameter, along with the trend direction angle. This angle is computed considering an non-dimensional temperature, adimensionalised by the maximum allowable temperature, $T_{s,limit} = 1750\ K$.

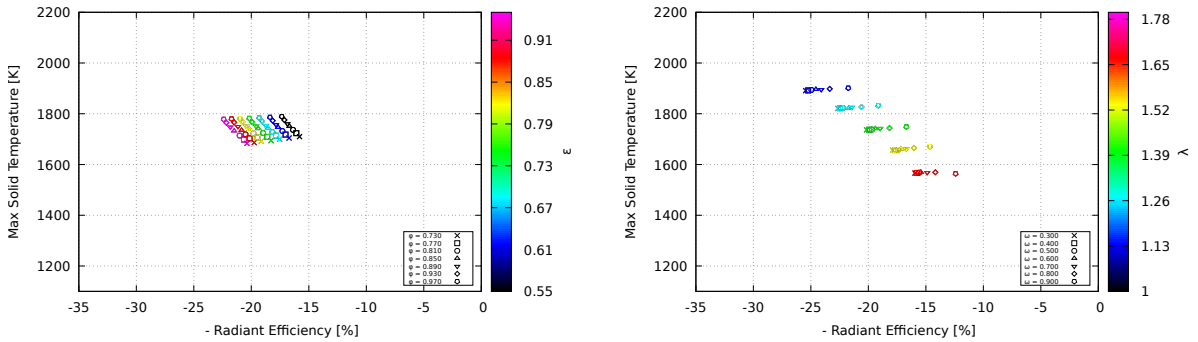

(a) (b)

Figure 4.7: Projection of the $2\mathrm{D}$ Parametric Domain for (a) ϕ *vs.* ε and (b) ϕ *vs.* ε on the Output Domain ($T_{s,max}$ *vs.* $-\eta_{rad}$): examples for linearly independent parameters.

4.3.1 Parametric Combinations

As discussed, one possible finding of the $2\mathrm{D}$ Parametric Study is that a given pair of parameters are linearly independent. Figure 4.7 presents two examples of this interaction on the Output Domain, for the combinations Porosity-Emissivity and Scattering Albedo-Excess Air Ratio. In each graph, changing colors corresponds to changing ε and λ, respectively, and changing symbols to ϕ and ω. The linear independence of the parameters is attested by noting that every row of equal symbols mimics the row with upward triangles (which corresponds to the $1\mathrm{D}$ curve for ε and λ), and every row with constant color mimics the green row (corresponding to ϕ and ω's $1\mathrm{D}$ curve). If this behavior were to occur for all parametric combinations it could be hypothesized that the linear combination of all the problem's parameters would yield an accurate Output Image, becoming needless to perform further case computations in order to find the parametric characteristics for the optimal performance of the PRB.

There are, however, some cases where the linear combination of the $1\mathrm{D}$ curves does not predict the results of the combination between parameters. Figure 4.8 provides a qualitative identification of parameter cross-influence: each curve correponds to the evolution of the $c_{v_r}(Q_{interest}/Parameter_i)$ with the variation of of a second parameter. For example, Figure 4.8 (c) shows how the coefficient of variation ratio of the radiant efficiency over the scattering albedo ($c_{v_r}(\eta_{rad}/\omega)$) changes with the variation of each of the remaining problem parameters.

One such case is represented in Figure 4.9 (a), which shows the interaction between the specific surface area and the pore diameter. Both of these parameters have an inverse trend, resulting in the superposition of the curves in the Output Domain, in which an expansion in the curves also occurs: when S_v takes lower values the impact of d_{pc} on the radiant efficiency increases. Likewise, when d_{pc} increases the impact of the specific surface area on η_{rad} is also increased. This behavior is captured in Figure 4.8 (a), which shows that impact magnitude of S_v on the radiant efficiency ($c_{v_r}(\eta_{rad}/S_v)$) is lowest for shorter pore diameters and highest for higher d_{pc}. These alterations the behavior are, however, towards the direction of lower efficiencies.

The cross-influence effect can also be observed in the interaction between the scattering albedo and the extinction coefficient (Figure 4.9 (b)): low values of extinction coefficient increase the impact

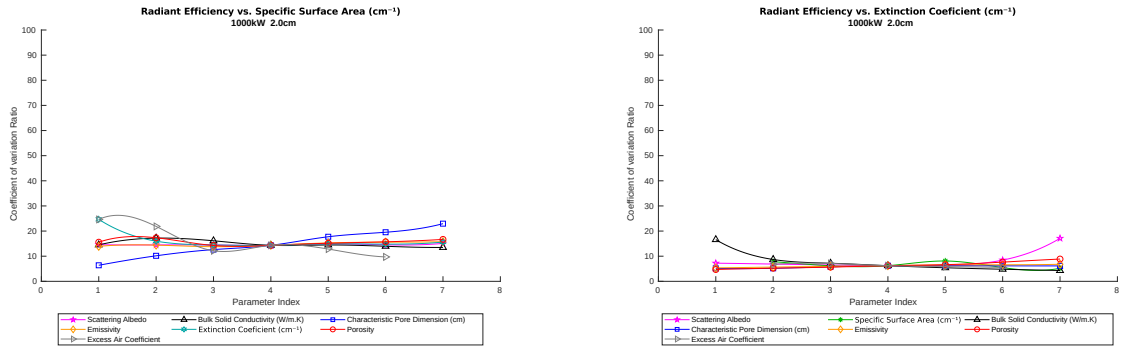

(a) $c_{v_r}\,(\eta_{rad}/S_v)$

(b) $c_{v_r}\,(\eta_{rad}/\beta)$

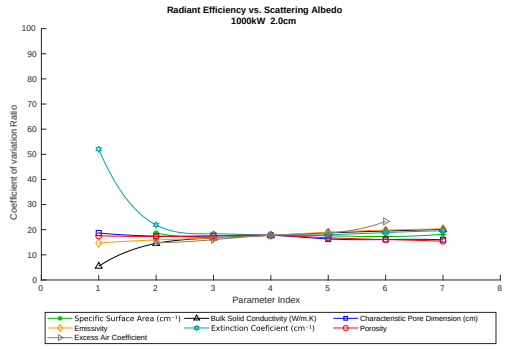

(c) $c_{v_r}\,(\eta_{rad}/\omega)$

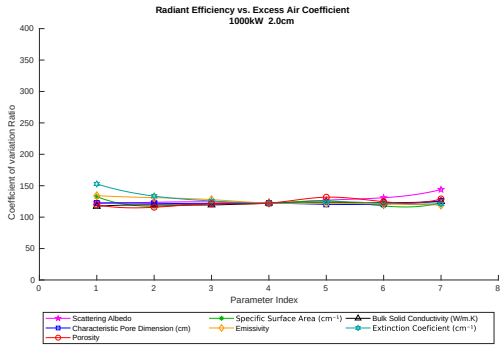

(d) $c_{v_r}\,(\eta_{rad}/\lambda)$

Figure 4.8: Evolution of $c_{v_r}(\eta_{rad})$ with the problem's parameters.

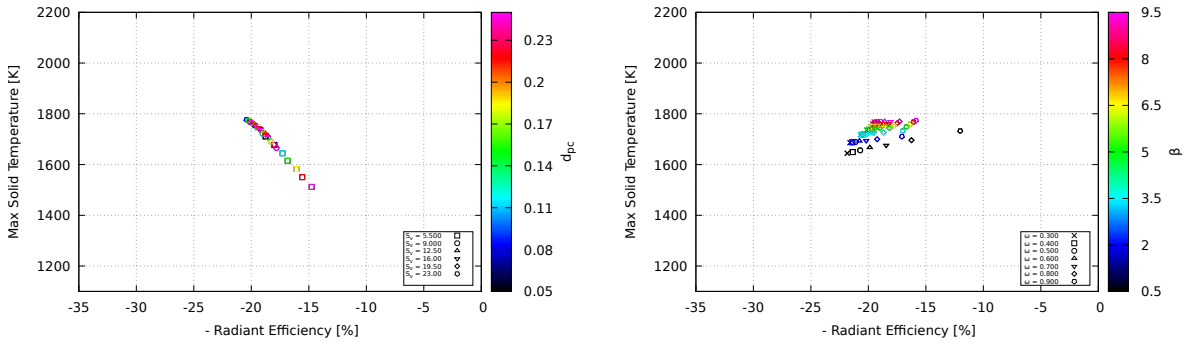

(a) (b)

Figure 4.9: Projection of the $2\mathrm{D}$ Parametric Domain for (a) S_v *vs.* d_{pc} and (b) ω *vs.* β on the Output Domain ($T_{s,max}$ *vs.* $-\eta_{rad}$): examples for parameters with cross-influence.

magnitude of the scattering albedo, an increase which serves once more to emphasize the negative effects of high ω on the radiant efficiency. With regard to β, it is also clear that the curve that describes the individual behavior of this parameter becomes distorted with changing ω: for lower values it becomes straighter in the low range of β, moving it towards a desirable zone of the Output Domain, whilst for higher ω the curvilinear shape at the bottom of β's range becomes more emphasized, increasing the penalty on η_{rad} and $T_{s,max}$. This particular case illustrates plainly how a given parameter value (in this case $\beta = 0.5\ \mathrm{cm}^{-1}$) can be very desirable for a given burner configuration (where $\omega < 0.4$), but can become undesirable for another ($\omega > 0.6$), a prime example of the non-linear nature of porous media combustion.

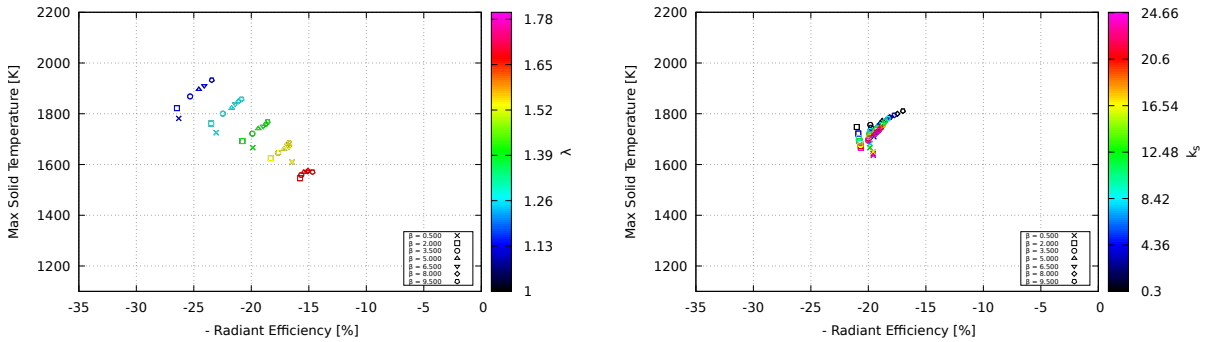

Figure 4.10: Projection of the $2\mathrm{D}$ Parametric Domain for (a) β *vs.* λ and (b) β *vs.* k_s on the Output Domain ($T_{s,max}$ *vs.* $-\eta_{rad}$): examples for parameters with cross-influence.

It is relevant to note that the extinction coefficient is involved in many of the cross-influences observed. Another case where the β is influenced by changes in the behavior of a parameter is in the combination with the excess air ratio. As seen in Figure 4.10 (a), with decreasing excess air both the shape of β's curve and the length in the η_{rad} axis is changed: the range of radiant efficiencies achieved is larger, and the penalty for the lower values of β is attenuated and eventually reversed. The interaction between the extinction coefficient and the solid conductivity (Figure 4.10 (b)) showcases one last example of the "interactive" nature of β: the η_{rad} range achieved by β becomes shorter with increasing k_s. This alteration in behavior is also captured in the behavior of c_{v_r} (η_{rad}/β) for the lower ranges of the solid conductivity (Figure 4.8 (b)). The volatility of β's behavior when combined with other parameters changes its status from a parameter with a meek impact and relevance to one of the most determinant parameters, as is seen in further in the next stage of the $\mathrm{Progressive\ Parametric\ Study}$.

4.3.2 Input Power and Burner Length

A look on the influence of the input power and the burner length is necessary, given that these parameters are left out of the main analysis but still play an important role in the process. In Section 4.2 the impact of these parameters on the $1\mathrm{D}$ Parametric Study for each of the 8 problem's parameters is touched on, but their influence on η_{rad} and $T_{s,max}$ still remains to be asserted. Furthermore, it is relevant to understand how do these parameters impact the $2\mathrm{D}$ parametric interactions.

Figure 4.11 shows the scatter of all computed cases on the Output Domain, for both the $1\mathrm{D}$ and $2\mathrm{D}$ stages of the study across all the PL combinations, along with the corresponding center cases (introduced in Table 4.1). An increase of Q_{comb} is shown to produce an overall decrease in radiant efficiency across all burner lengths, whilst having little to no effect on the peak solid temperature. An increase in burner length, on the other hand, influences positively η_{rad}, albeit not significantly. Its effect on $T_{s,max}$, however, is stronger, producing a temperature increase of around $250\ \mathrm{K}$ with increasing L for the baseline cases and an increase in incidence of cases above the maximum allowable temperature ($1750\ \mathrm{K}$, [13, 20]), especially for $L = 3.0\ \mathrm{cm}$. This is likely caused by the increase in surfaces available for convective heat transfer from the gas, allowing more energy to be transferred to the solid, without

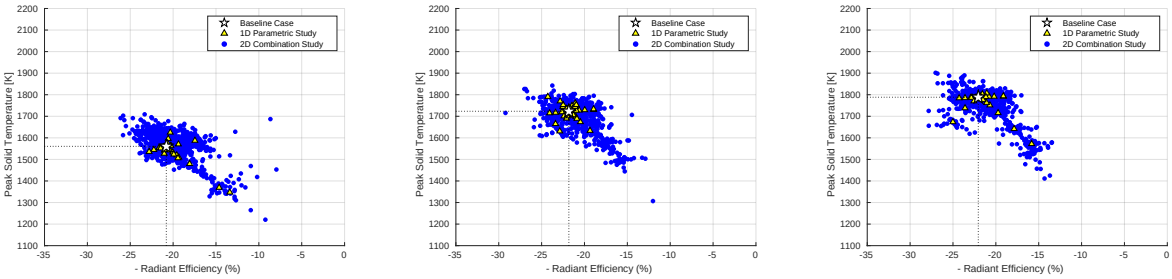

(a) $Q_{comb} = 800$ W and $L = 1.0$ cm. (b) $Q_{comb} = 800$ kW and $L = 2.0$ cm. (c) $Q_{comb} = 800$ kW and $L = 3.0$ cm.

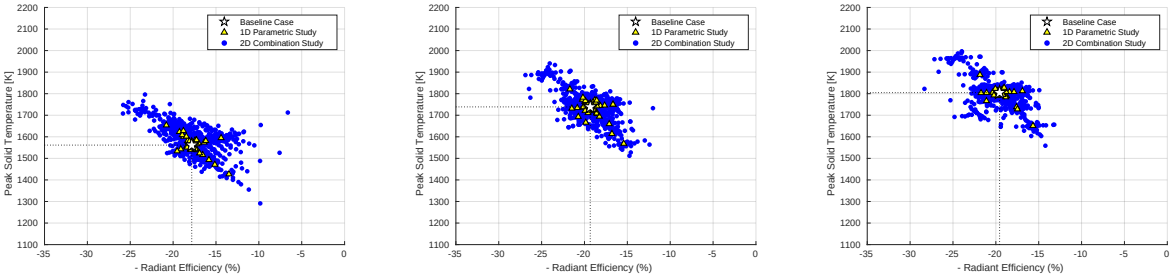

(d) $Q_{comb} = 1000$ kW and $L = 1.0$ cm. (e) $Q_{comb} = 1000$ kW and $L = 2.0$ cm. (f) $Q_{comb} = 1000$ kW and $L = 3.0$ cm.

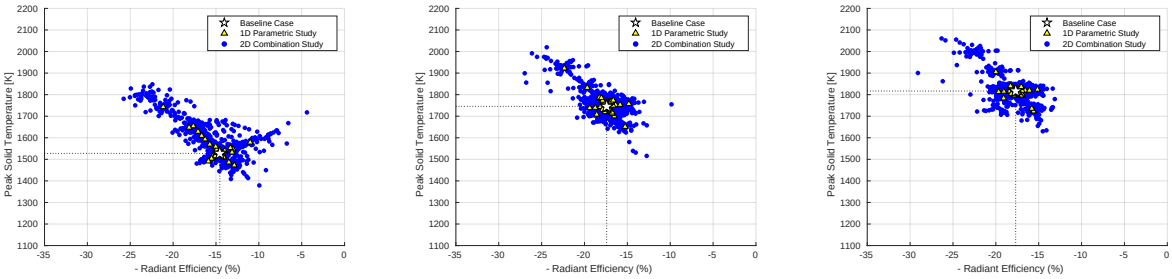

(g) $Q_{comb} = 1200$ kW and $L = 1.0$ cm. (h) $Q_{comb} = 1200$ kW and $L = 2.0$ cm. (i) $Q_{comb} = 1200$ kW and $L = 3.0$ cm.

Figure 4.11: Output Image of the cases computed for the $1\mathrm{D}$ and $2\mathrm{D}$ Parametric Study, for all input powers and burner lengths.

there being a matching outlet mechanism for this energy. This analysis is observable for the bulk of the cases' swarm for each Power/Length combination, despite there being some outliers with more irregular behavior. On the whole, the most desirable PL pair for the purposes of this work is the case with $Q_{comb} = 800$ kW and $L = 2.0$ cm, with high radiant efficiencies, as found in the literature review, and peak solid temperatures below the limit.

Given that both the input power and the burner length have some impact on the interest quantities, it is relevant to ask how the parametric interactions established in the previous section fare with the variation of these secondary parameters.

Figure 4.12 provides a comparison of the interactions between the emissivity and the excess air ratio for different values of Q_{comb} and L, two of the most influential parameters in the study, and that are linearly independent. It is shown that the input power does not introduce changes in the interaction between these parameters, with the parameters' curves maintaining their shape in with the variation of Q_{comb}. The burner length, on the other hand, induces changes: higher L leads to a reduced impact of ε on the maximum solid temperature, which is consistent with the findings of Section 4.2. Furthermore,

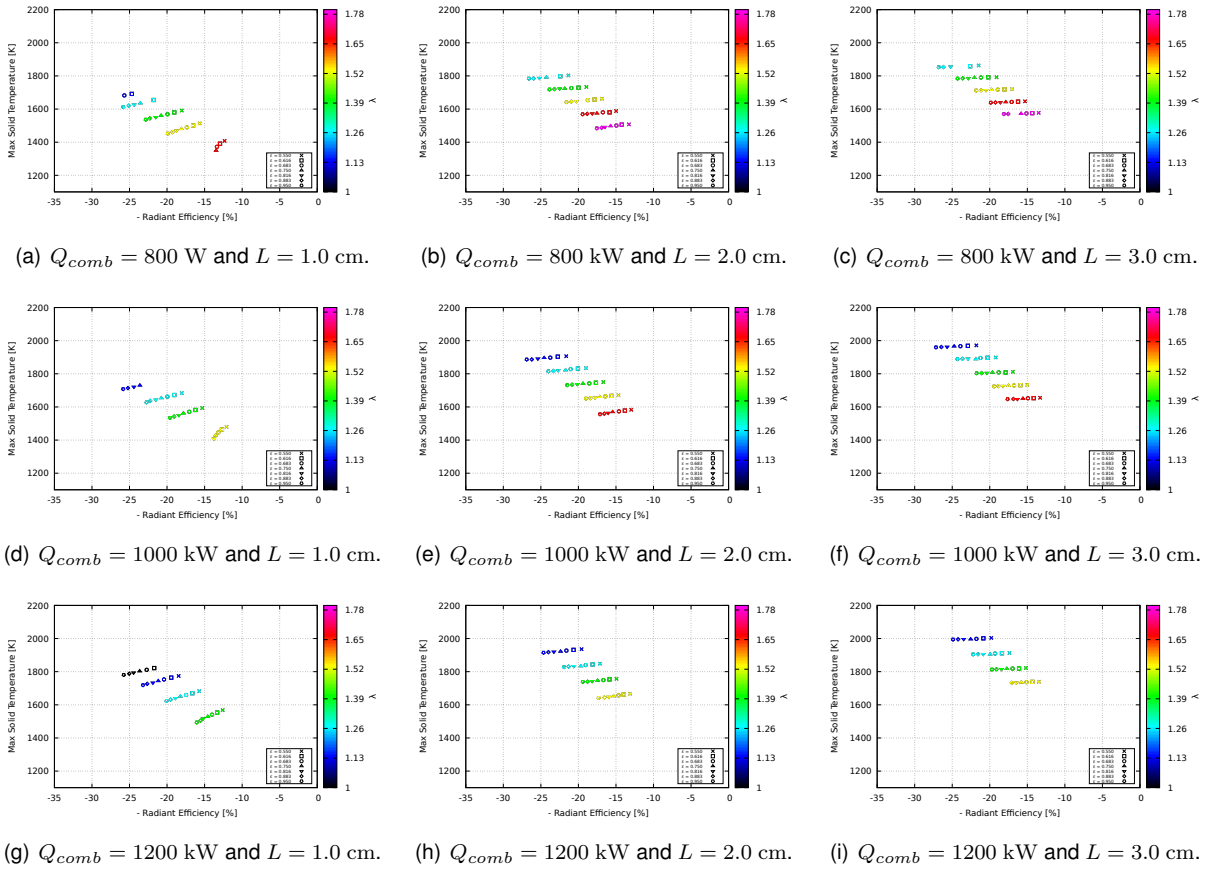

(a) $Q_{comb} = 800$ W and $L = 1.0$ cm. (b) $Q_{comb} = 800$ kW and $L = 2.0$ cm. (c) $Q_{comb} = 800$ kW and $L = 3.0$ cm.

(d) $Q_{comb} = 1000$ kW and $L = 1.0$ cm. (e) $Q_{comb} = 1000$ kW and $L = 2.0$ cm. (f) $Q_{comb} = 1000$ kW and $L = 3.0$ cm.

(g) $Q_{comb} = 1200$ kW and $L = 1.0$ cm. (h) $Q_{comb} = 1200$ kW and $L = 2.0$ cm. (i) $Q_{comb} = 1200$ kW and $L = 3.0$ cm.

Figure 4.12: Output Image $Q_{comb} = 1000$ kW and $L = 2.0$ cm for the combination ε *vs.* λ , across all input powers and burner lengths.

for $L = 1.0$ cm a distortion in the behavior of the emissivity is introduced, for the higher values of λ. This occurrence is not captured for $Q_{comb} = 1200$ kW because those cases do not present a stable flame and thus were not computed. This is to be expected for this burner length which has naturally a shorter length on where the flame can be stabilized, increasing the occurrence of cases that are not computed.

The interaction between the extinction coefficient and the excess air ratio, presented in Figure 4.13, exhibits a similiar logic, despite the different nature of the parametric combination: the general behavior of the two parameters is kept across variations of Q_{comb}, but not for L. A decrease in the burner length further penalizes low values of β when λ is highest, emphasizing the warp that characterizes the behavior of the extinction coefficient. Another observable consequence of decreasing L is, once more, the increase of unstable cases, for the reason stated earlier. Note that, as can be attested from figures 4.12 and 4.13, whilst the overall range of η_{rad} achieved by λ is not changed across Q_{comb}, lower values of input power allow for higher radiant efficiencies with leaner mixtures.

Lastly, the combination between d_{pc} and ε, besides reiterating the behavior of the emissivity with Q_{comb} and L, also sheds light on the increase in $c_{v_r}(\eta_{rad}/d_{pc})$ observed in Table 4.6: both input power and burner length are shown to increase the impact of the parameter (Figure 4.14), with $L = 1$ cm introducing the most palpable changes. This increase in impact, however, moves in the direction of lower radiant efficiencies (and also lower $T_{s,max}$). This behavior is observed for most of d_{pc}'s interactions, as well as for S_v, which are both connected to the convective heat transfer between the gas and solid-

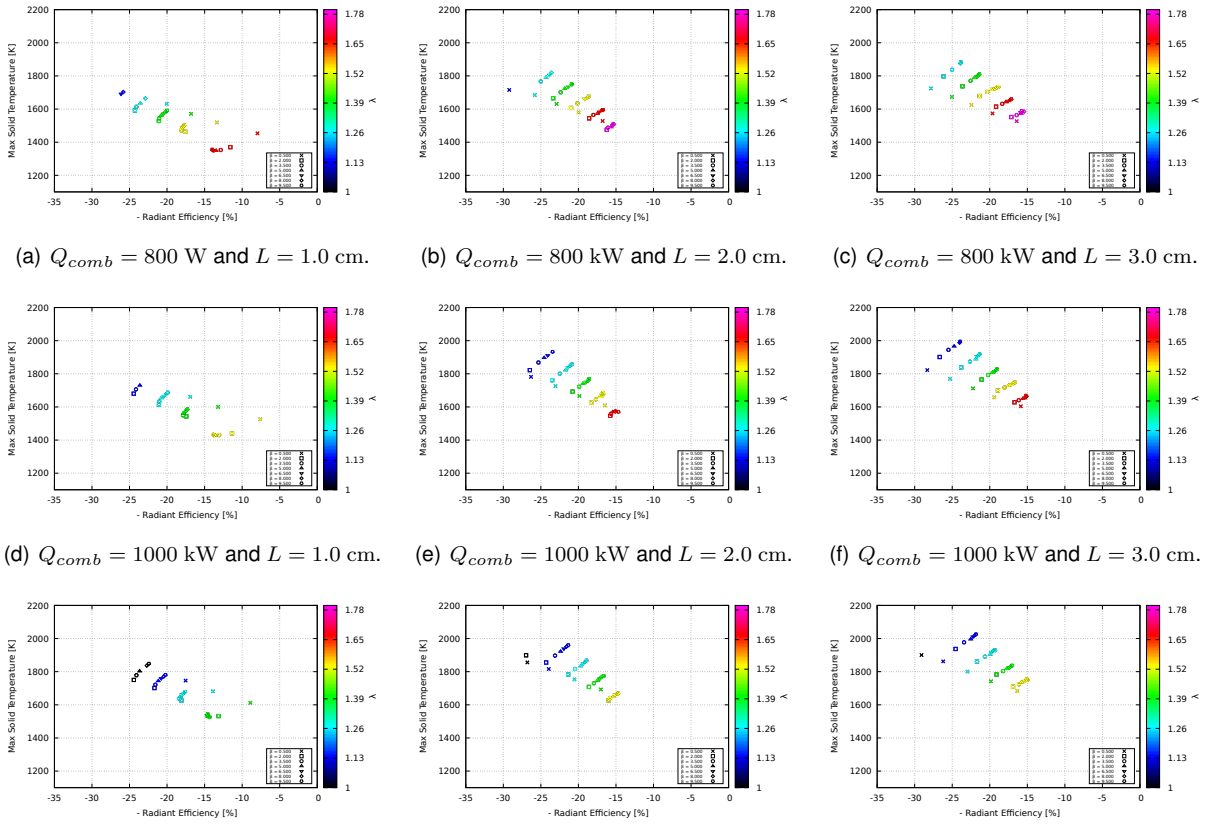

(a) $Q_{comb} = 800$ W and $L = 1.0$ cm. (b) $Q_{comb} = 800$ kW and $L = 2.0$ cm. (c) $Q_{comb} = 800$ kW and $L = 3.0$ cm.

(d) $Q_{comb} = 1000$ kW and $L = 1.0$ cm. (e) $Q_{comb} = 1000$ kW and $L = 2.0$ cm. (f) $Q_{comb} = 1000$ kW and $L = 3.0$ cm.

(g) $Q_{comb} = 1200$ kW and $L = 1.0$ cm. (h) $Q_{comb} = 1200$ kW and $L = 2.0$ cm. (i) $Q_{comb} = 1200$ kW and $L = 3.0$ cm.

Figure 4.13: Output Image $Q_{comb} = 1000$ kW and $L = 2.0$ cm for the combination β *vs.* λ , across all input powers and burner lengths.

phases. This means that for lower lengths the impact of the convective heat transfer becomes more significant as far as reducing the performance of the burner (but does not improve it).

As illustrated by these examples, supported by the remaining data in Appendix A.1, it becomes apparent that the full 8D analysis is required in order to learn how to get to the best radiant burner in terms of radiant efficiency. Despite there being many parameters that present an almost linearly independent combination across their domain, there are some that do not follow this rule, especially around the fringe values of the parameters. This means that a linear combination of the 1D results could probably produce accurate predictions for the points near the center of the parametric domain, but since the purpose of this work is to find the fringe situation that produces the highest radiant efficiency, it becomes necessary to use a model that allows a more accurate prediction of these interactions.

4.4 Full 8-Dimensional Parametric Combination

A grand total of 1012793 different cases were computed in this stage of the optimization effort, for 3 different burner lengths and 2 different input powers. Figure 4.15 illustrates the placement of these cases on the Output Domain along with the cases from the previous stages of the $\mathrm{Progressive\ Parametric\ Study}$.

A larger range within the Output Domain is achieved, when compared to the previous stage, both towards desirable and undesirable results of both interest quantities, as would be expected. For all sets

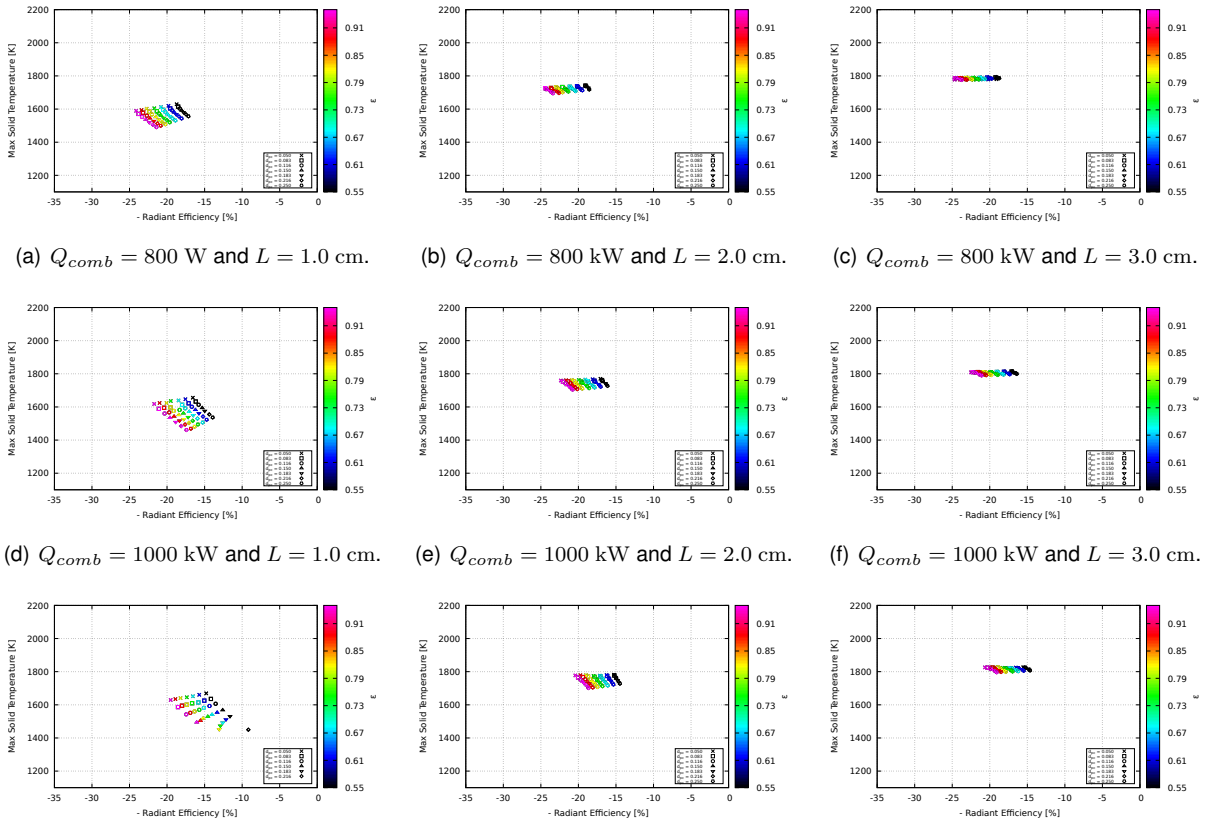

(a) $Q_{comb} = 800$ W and $L = 1.0$ cm. (b) $Q_{comb} = 800$ kW and $L = 2.0$ cm. (c) $Q_{comb} = 800$ kW and $L = 3.0$ cm.

(d) $Q_{comb} = 1000$ kW and $L = 1.0$ cm. (e) $Q_{comb} = 1000$ kW and $L = 2.0$ cm. (f) $Q_{comb} = 1000$ kW and $L = 3.0$ cm.

(g) $Q_{comb} = 1200$ kW and $L = 1.0$ cm. (h) $Q_{comb} = 1200$ kW and $L = 2.0$ cm. (i) $Q_{comb} = 1200$ kW and $L = 3.0$ cm.

Figure 4.14: Output Image $Q_{comb} = 1000$ kW and $L = 2.0$ cm for the combination d_{pc} *vs.* ε , across all input powers and burner lengths.

of cases an increase of at least 10% in η_{rad} ($\sim 50\%$ relative improvement) is achieved when compared to the respective center case. The set with $L = 1.0$ cm confirms the tendency established in Section 4.3 for this burner length, where the parametric interactions tend to produce poorer results with regard to the radiant efficiency, with a large portion of the cases in the 8D study falling to the lower side of η_{rad} when compared to the cases in the earlier stages.

Overall, the behavior of the input power and burner length defined in Section 4.3 is confirmed. The case with $L = 3.0$ cm presents similar radiant efficiencies to the reference $Q_{comb} = 1000$ kW and $L = 2.0$ cm, however more than half the cases are above the temperature limit for the solid. The case with $L = 1.0$ cm presents good peak temperature values in its highest η_{rad} zone, but falls short in the radiant efficiency when compared to its counterparts. With regard to the differences between the two input powers, the case with $Q_{comb} = 800$ kW reaches higher radiant efficiencies than all other PL combinations, all well within the required temperature limits, once more sustaining that this is the most desirable Power/Length combination for the purposes of this work.

It is also relevant to note that the Pareto front, the set of points that constitutes the optimal combination between the two interest quantities (low $-\eta_{rad}$ and low $T_{s,max}$), is linear and has similar a slope for all four sets of studies in Figure 4.15. The points at the possibility of a relationship between the peak solid temperature and and the radiant efficiency (equivalente to radiant output in this case) that defines the ceiling of these two quantities from an optimization standpoint.

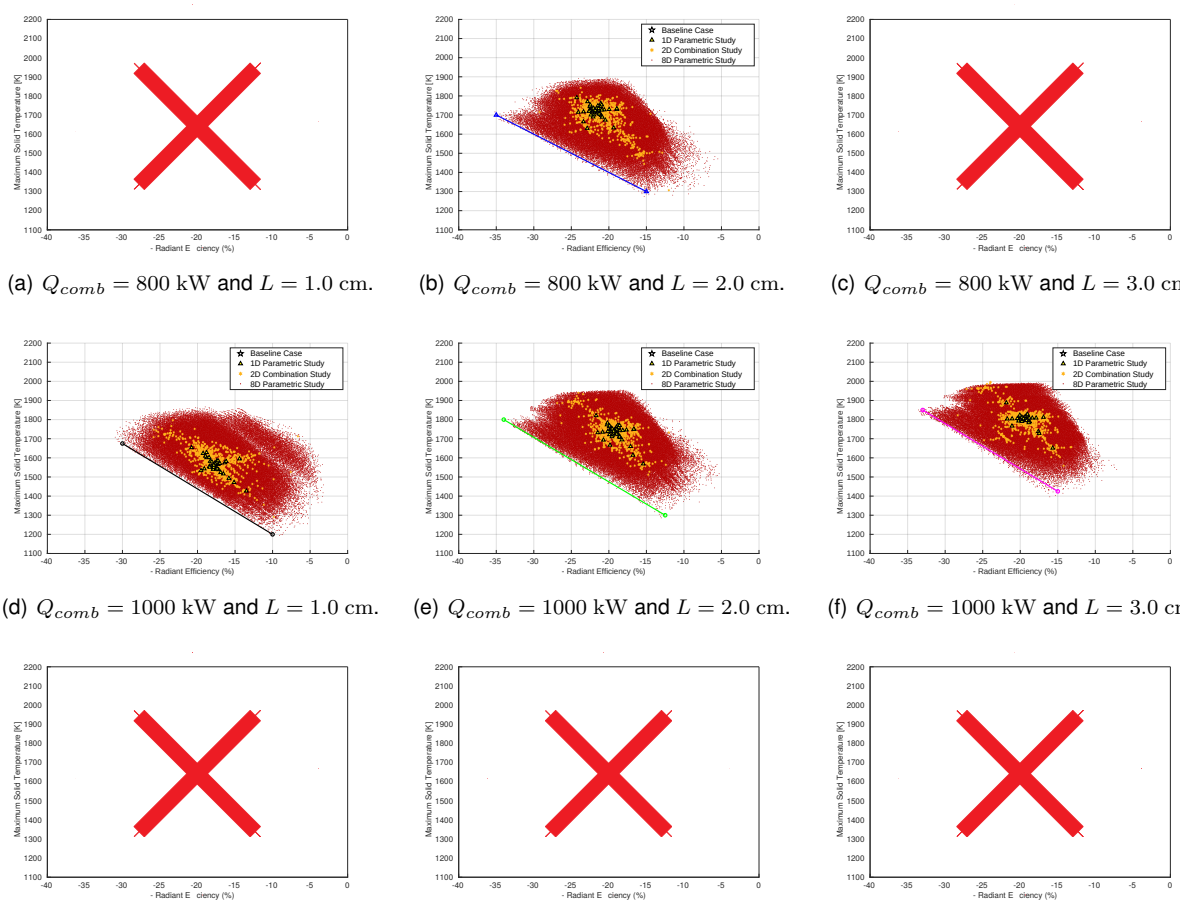

(a) $Q_{comb} = 800$ kW and $L = 1.0$ cm. (b) $Q_{comb} = 800$ kW and $L = 2.0$ cm. (c) $Q_{comb} = 800$ kW and $L = 3.0$ cm.

(d) $Q_{comb} = 1000$ kW and $L = 1.0$ cm. (e) $Q_{comb} = 1000$ kW and $L = 2.0$ cm. (f) $Q_{comb} = 1000$ kW and $L = 3.0$ cm.

(g) $Q_{comb} = 1200$ kW and $L = 1.0$ cm. (h) $Q_{comb} = 1200$ kW and $L = 2.0$ cm. (i) $Q_{comb} = 1200$ kW and $L = 3.0$ cm.

Figure 4.15: Scatter map of the distinct phases of the $\mathrm{Progressive\ Parametric\ Study}$ for 4 different Power/Length combinations, including the respective center/baseline cases and pareto front (the red cross signals PL combinations that were left aside).

In the interest of defining the parametric characteristics that a porous radiant burner must possess in order to achieve this level of performance several strategies are employed, with the purpose of tackling the complex nature of the results in this stage of the study. The following of assessments are carried out for the reference Power/Length combination ($Q_{comb} = 800$ kW and $L = 2$ cm) as well as for $Q_{comb} = 1000$ kW and $L = 2$ cm, the two best performing sets of $8\mathrm{D}$ studies.

4.4.1 Parameter Scatter Visualization

A visualization of the Output Domain according to the indexes of each parameter is presented, with the aim of providing a visual understanding of how the problem's parameters relate to the position of each case in the interest quantity domain, and drawing parallels, when possible, to the results achieved in the previous stages of the PPS.

Figures 4.16 (a) and (b) show the excess air ratio evidencing a clearly defined behavior with regard to the interest quantities. The distribution of λ is well sorted, showing that this parameter is very determinant to the placement of a given case in the Output Domain, which is to say, to the performance of a porous burner. This distribution mimics faithfully the behavior established in Section 4.2, with an

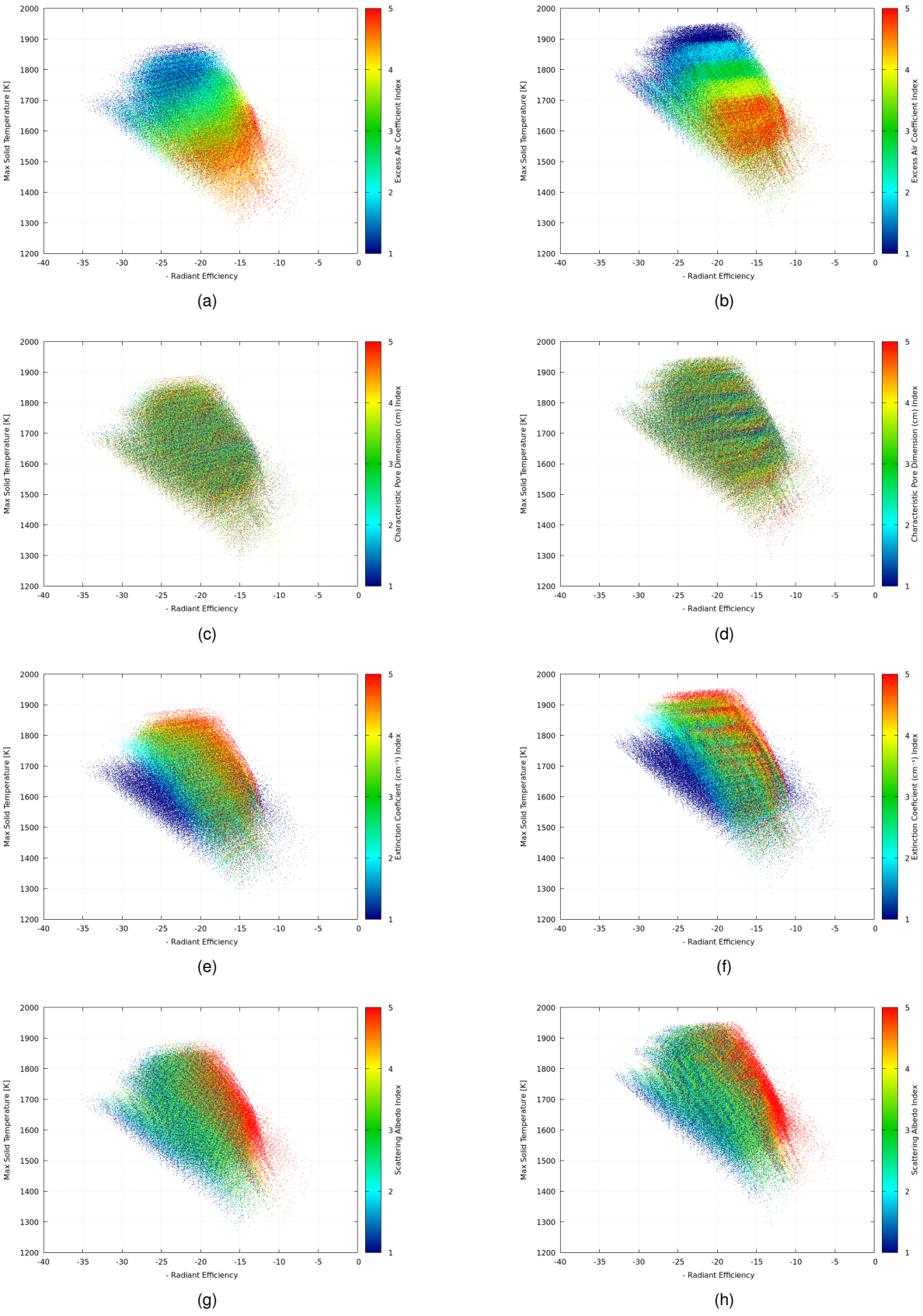

Figure 4.16: Examples of parametric distributions on the Output Domain, for $Q_{comb} = 800$ kW - $L = 2.0$ cm and $Q_{comb} = 1000$ kW - $L = 2.0$ cm, respectively: (a) and (b) Excess Air Ratio; (c) and (d) Characteristic Pore Diameter; (e) and (f) Extinction Coefficient; (g) and (h) Scattering Albedo.

indirect trend where the lower values of λ yield high radiant efficiencies and peak solid temperatures. The set with $Q_{comb} = 800\ \mathrm{kW}$ does not present as many cases with λ_1 as the reference PL due to the proximity the stability limits and consequently the occurrence of flashback. It is confirmed that for lower input powers it is possible to achieve similar radiant efficiencies with leaner fuel mixtures.

The characteristic pore diameter is presented in figures 4.16 (c) and (d) as an inconsequential parameter, when compared to its counterparts. The swarm of cases is nearly homogeneous, for both values of Q_{comb}, meaning that the placement of the cases in the Output Domain, and thus the interest quantities η_{rad} and $T_{s,max}$, are independent from this parameter.

A parameter which presents an interesting distribution is the extinction coefficient, already established an important parameter due to its highly variable influence on the interest quantities, especially when in tandem with other parameters. Figure 4.16 (e) and (f) showcase this importance, with the Pareto front of both sets being clearly dictated by $\beta = 1.0\ \mathrm{cm}^{-1}$. It is also worthy to note that a portion of the cases with lower η_{rad} also have $\beta = 1.0\ \mathrm{cm}^{-1}$, which is in consonance with the findings in Section 4.3 regarding the extinction coefficient ability to either improve or worsen the overall performance of the burner depending on its conjugation with other parameters. This conjugation effect is most clearly observed in the combination with ω, in figures 4.16 (g) and (h), with the points with low β mentioned earlier corresponding to the points with higher scattering albedo ($\omega = 0.9$), once more in concordance with the conclusions drawn from the $\mathrm{2D}$ study between these parameters.

4.4.2 Desirable Zone Analysis

In this section the analysis is centered on the Desirable and the Most Desirable zones of the Output Domain, that are located on the Pareto front of the parametric distribution. For the purposes of this work, the Desirable Zone is defined as the set of case points, for each PL pair, that have a radiant efficiency above 25%, the maximum achieved in previous stages of the study, which coincides with the efficiency mark that is widely reported in the literature [33, 36–38]. The ceiling for the maximum solid temperature is set at $1750\mathrm{K}$, based on the commercial and cientific reference values in the literature [13, 20]. The Most Desirable Zone is an approximation made to the ”optimal point” with regard to radiant efficiency and solid maximum temperature. It is defined as a rectangle (1% by $10\ \mathrm{K}$) that lies on the Pareto front, at the zone with the highest radiant efficiency that is below the temperature ceiling. Another criteria is that the point density must be sufficient and balanced. Figure 4.17 shows the full domains for both powers ((a) and (d)), zooming on the Desirable Zone ((b) and (e)), and finally zooming on the optimal point, the Most Desirable Zone ((c) and (f)).

Upon observation it is clear that the zone for $Q_{comb} = 800\ \mathrm{kW}$ has significantly more points in the Desirable zone. This is consequence of the already established behavior of the input power (both in the literature and in the present investigations) that lower Q_{comb} lead to higher radiant efficiencies. On the other hand, the cases for this power exhibit an important decrease in peak solid temperature. This is due to the possibility of stabilizing leaner flames (with lower flame temperatures) in the burner when the input power is lower, established both in the $\mathrm{1D}$ and $\mathrm{2D}$ stages of the study.

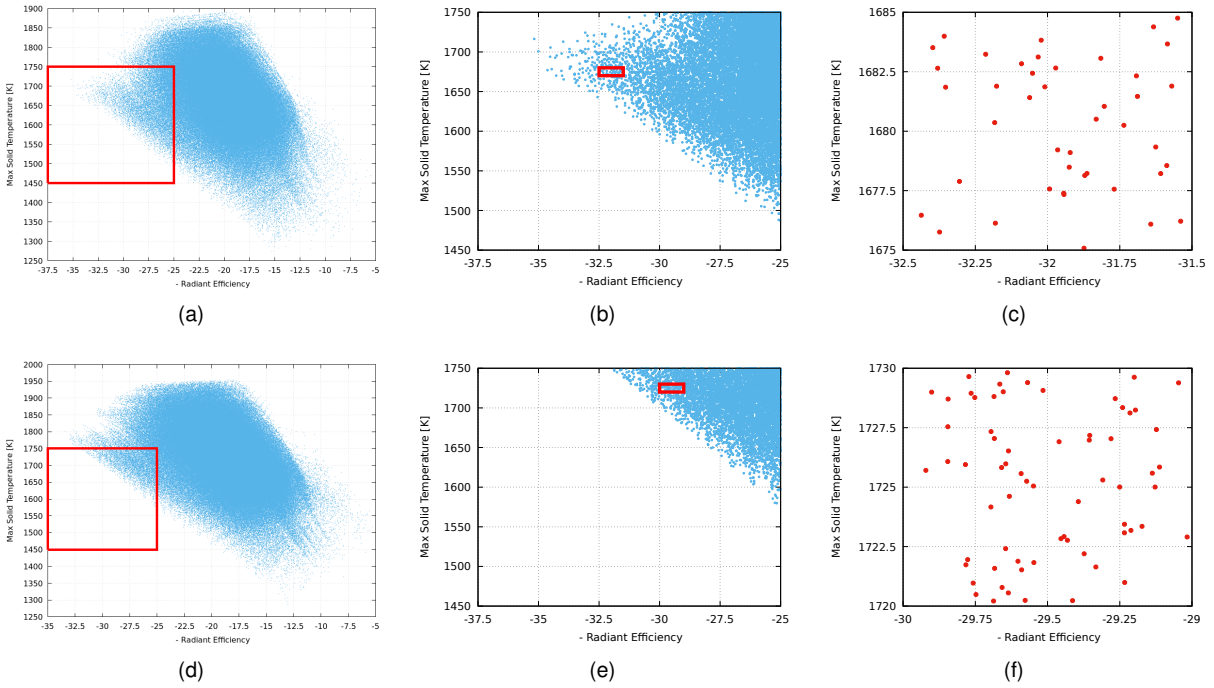

Figure 4.17: Illustration of the Desirable (middle) and the Most Desirable (right) zones for the two input powers, taken from each original case set (left): (a) - (c) $Q_{comb} = 800$ kW ; (d) - (f) $Q_{comb} = 1000$ kW.

Parametric Probability Distribution

A statistical analysis is performed on the Desirable and Most Desirable zones in order to carve out what are the parameters actually determinant for the performance purposes of this work. This analysis is essentially a quantification of the parameter distribution plots (Figure 4.16), that takes the form of the discrete Probability Distribution Function (PDF). The index distribution of each parameter is explicitly defined, and the results for both the Desirable and the Most Desirable zones are compared.

The extinction coefficient is the most polarized parameter, with a clear preference for the lower values in the Desirable zone and a 100% incidence of $\beta = 1.0$ cm^{-1} on the Most Desirable zone for both input powers. Likewise, the emissivity has a strong preference for the higher values in the Desirable zone, and a severe preference for $\varepsilon = 0.9$ for both Q_{comb} in the Most Desirable zone. In the Desirable zone the excess air is more frequently towards the lower values (the fact that λ_1 is less probable than λ_2 for $Q_{comb} = 800$ kW is due to the fact that not many of these cases are not stable, as evidenced by the decrease of dark blue cases in Figure 4.16 (a) when compared to (b)). The scattering albedo is more successful for its lower values in both zones, with $\omega = 0.9$ being the undesirable one.

Note that the preference for low β and high λ, as well as the need to avoid ω is in complete concordance with the findings in the 2D parametric study. Indeed it is these 3 parameters, along with ε that are the ones that drive the radiant performance and temperature of a porous radiant burner.

The remaining parameters have a weak influence. The characteristic pore diameter and the thermal conductivity of the solid are once more shown to have no determinant effect on the interest quantities, exhibiting nearly even distributions for all values in both input powers. With regard to S_v, there is a small preference for higher values in $Q_{comb} = 1000$ kW, avoiding the situation where $S_v < 8.75$ cm^{-1}. For

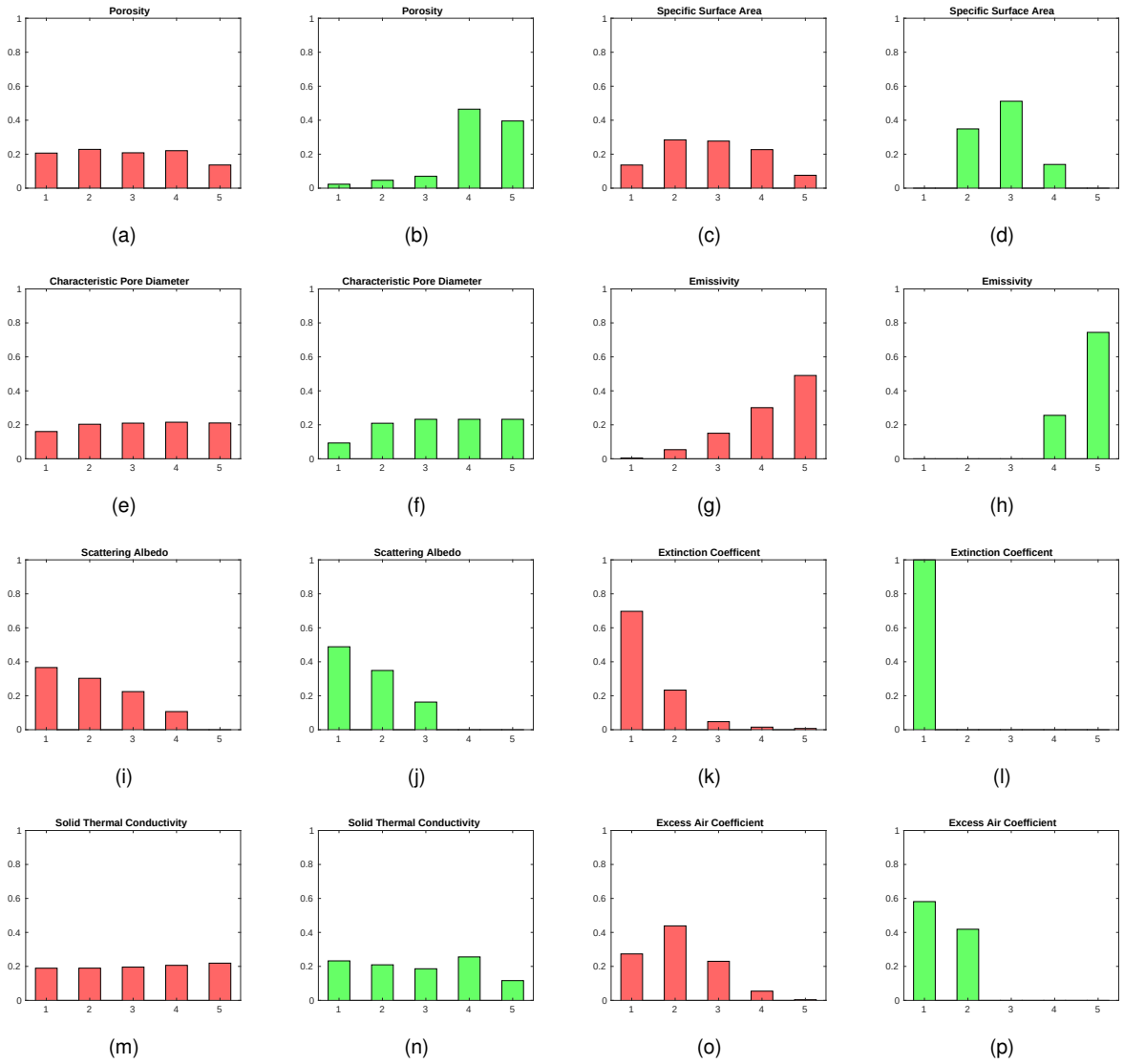

Figure 4.18: Probability Distribution Function (PDF) *vs.* problem parameter indices, in the Desirable and Most Desirable zones, respectively, for $Q_{comb} = 800\,\mathrm{kW}$: (a) and (b) Porosity; (c) and (d) Specific Surface Area; (e) and (f) Characteristic Pore Diameter; (g) and (h) Emissivity; (i) and (j) Scattering Albedo; (k) and (l) Extinction Coefficient; (m) and (n) Solid Thermal Conductivity; (o) and (p) Excess Air Ratio.

the set with $Q_{comb} = 800\ \mathrm{kW}$ the preference lies within the mid range, but it it is not very convincing. The same occurs with the porosity, where there is also more incidence of the higher values of ϕ, but all instances are present in both zones.

Case Fitness

The previous section provided a clear-cut direction to follow in order to achieve peak PRB performance, as defined in this work. However, issues like material availability, ability to control material properties and even inevitable model uncertainties likely will not allow the exact reproduction of these results. This is dealt with through a fitness analysis to the cases in the Desirable zone. The fitness is defined as the negative distance between a given case and the centroid of the Most Desirable zone (for each of the input powers considered) and its goal is to provide a more robust design estimate for the parameters. It

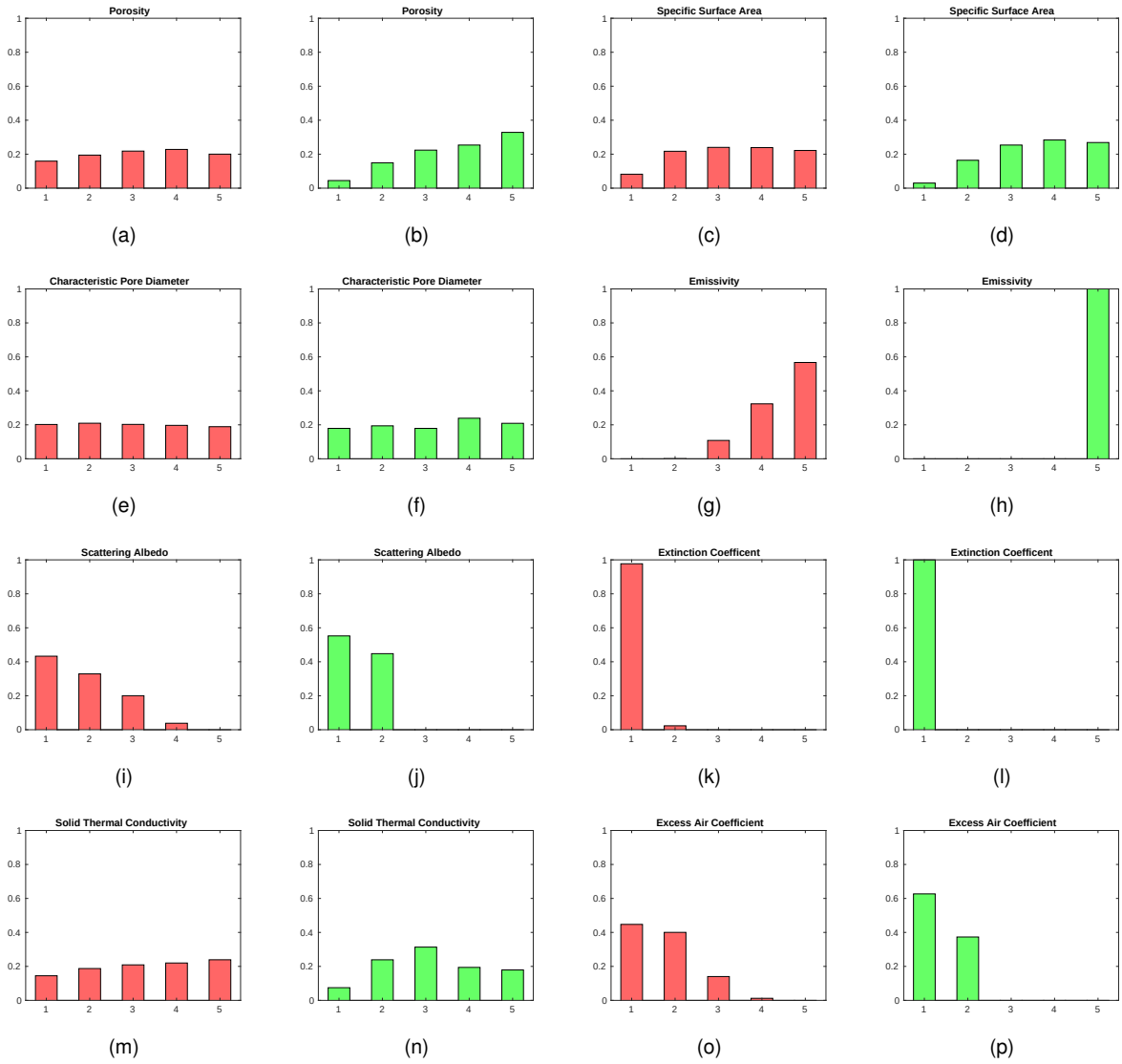

Figure 4.19: Probability Distribution Function *vs.* problem parameter indices, in the Desirable and Most Desirable zones, respectively, for $Q_{comb} = 1000\ \mathrm{kW}$: (a) and (b) Porosity; (c) and (d) Specific Surface Area; (e) and (f) Characteristic Pore Diameter; (g) and (h) Emissivity; (i) and (j) Scattering Albedo; (k) and (l) Extinction Coefficient; (m) and (n) Solid Thermal Conductivity; (o) and (p) Excess Air Ratio.

can be defined as:

$$fit_i = -\left\|C_{i,D} - C_{c,MD}\right\| \tag{4.3}$$

where fit_i corresponds to the fitness of a given case i in the Desirable Zone, $C_{i,D}$ corresponds to the coordinates of case i in the Output Domain referential ($-\eta_{rad}$, $T_{s,max}$) and $C_{c,MD}$ is the coordinates of the centroid of the Most Desirable zone (Figure 4.17). The closer to zero this quantity is, the closer to the optimal configuration a given case is: $fit_i|_{MD} = 0$.

The results for $Q_{comb} = 800\ \mathrm{kW}$ and $Q_{comb} = 1000\ \mathrm{kW}$ powers are presented in figures 4.20 and 4.21, respectively. Each subfigure presents a "bubble histogram" of the fitness distribution for each parametric index, where the diameter of the bubble is equivalent to the height of a typical histogram. The classes, set on the vertical axis, evaluate the distribution of fitness according to each parameter value (horizontal axis). For example, in Figure 4.20 (f) a large bubble in the $0 - 20$ class for the index 1 means that there

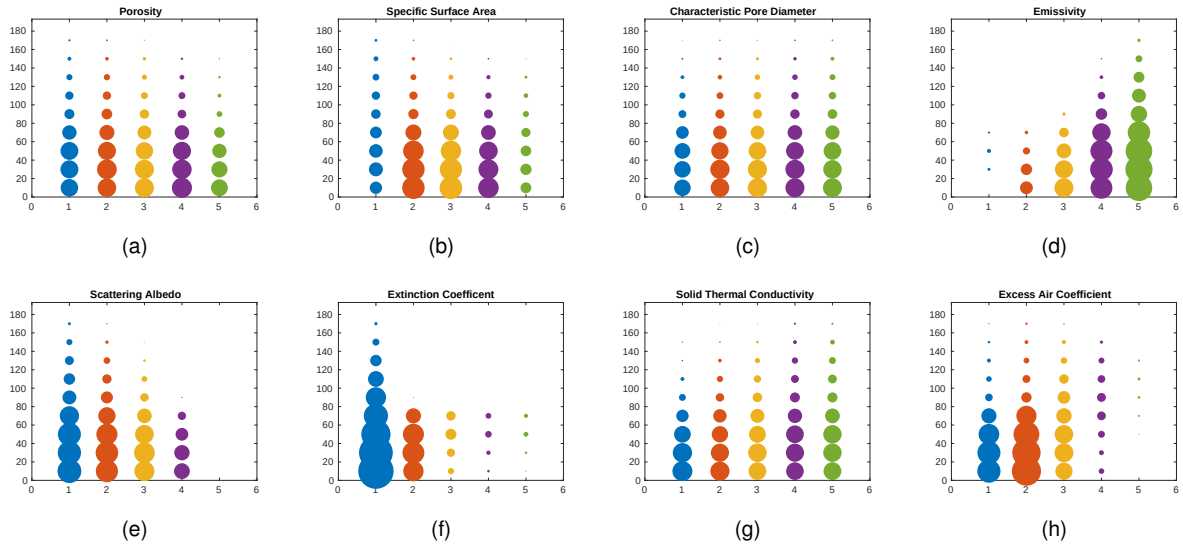

Figure 4.20: Fitness distribution *vs.* problem parameter indices, $Q_{comb} = 800$ kW: (a) Porosity; (b) Specific Surface Area; (c) Characteristic Pore Diameter; (d) Emissivity; (e) Scattering Albedo; (f) Extinction Coefficient; (g) Solid Thermal Conductivity; (h) Excess Air Ratio.

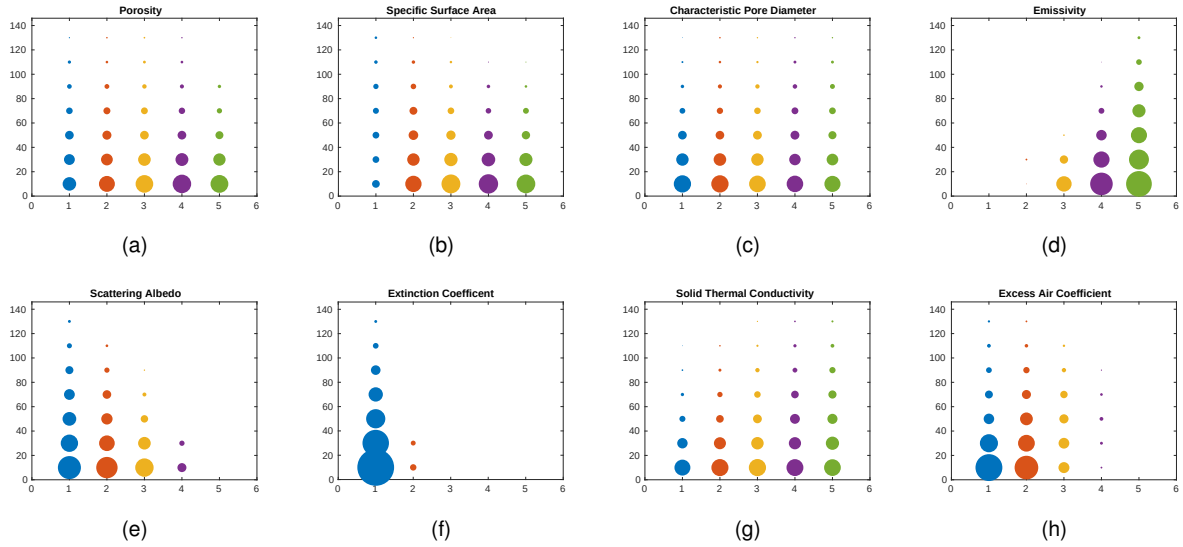

Figure 4.21: Fitness distribution *vs.* problem parameter indices, $Q_{comb} = 1000$ kW: (a) Porosity; (b) Specific Surface Area; (c) Characteristic Pore Diameter; (d) Emissivity; (e) Scattering Albedo; (f) Extinction Coefficient; (g) Solid Thermal Conductivity; (h) Excess Air Ratio.

is a large amount of cases with $\beta_1 = 1$ cm^{-1} that have a fitness inferior to 20. Conversely, the bubble in the $0 - 20$ class for the index 4 shows that there are very few cases with less β_4 and $fit_i < 20$. Note that for each parameter, the total bubble diameter is linearly tied to the number of cases in the Desirable zone, for each 8D set.

With this in mind, it is clear once more that the set with $Q_{comb} = 800$ kW presents significantly more cases in the Desirable zone than its counterpart. Still, the conclusions drawn from this part of the analysis are similar for both input powers. The porosity, characteristic pore diameter and thermal solid conductivity all have several cases in the highest fitness class throughout their entire range. For the lower input power, S_v reiterates the preference for mid range values, whilst for $Q_{comb} = 1000$ kW it is

only the lower value of the surface area that has poor representation in the highest fitness class. With regard to the more determinant parameters, this analysis gives strength to the conclusions drawn by the probability density functions. The emissivity, despite presenting a strong preference for $\varepsilon = 0.9$ in both Most Desirable zones is shown to be able to reach good fitness with inferior values. For λ and ω the low range established in the PDFs is confirmed, and so is the need for both these parameters to avoid higher values. The once situation where the fitness study does not prove to be forgiving in the requirements for optimal performance is in the case of the extinction coefficient. Especially for $Q_{comb} = 1000\ \mathrm{kW}$, there are very few cases in the high fitness class, or any other, other that $\beta = 1.0\ \mathrm{kW}$. The situation is not as extreme for $Q_{comb} = 1000\ \mathrm{kW}$, which presents a more forgiving distribution of fitness for the extinction coefficient.

Chapter 5

Conclusions

This chapter closes the Thesis. First, a reflection on the work's goals is given, along with a discussion on the challenges encountered. Then, a summary of the results from Chapter 4, followed by some concluding remarks on the outcomes of the investigations. The chapter closes with some recommendations for future work.

5.1 Achievements

A series of tasks have been carried out with the purpose of fulfilling the main goal of this Thesis: the multi-parametric performance optimization of the radiation efficiency and maximum solid temperature of a Porous Radiant Burner. A one-dimensional model for the methane/air combustion within porous media, with multi-step kinetics, radiation heat transfer modeled with the S_6 approximation and two energy equations for gas and solid phases was employed.

Preliminary investigations allowed the author to gain sensitivity to the particularities of the model and to the flame behavior in porous inert media, especially with regard to stability. This knowledge was paramount for the successful development of the $\mathrm{Domain\ Exploration}$ code, an application of the numerical model, a $\mathrm{FORTRAN\ 77}$ code, programmed in MATLAB and with sh scripts, for the interface between them. The code uses a Systems of Decision approach in order to manage the large-scale computation of inter-dependent burner cases, for 8 simultaneously varying parameters, and with the capability of dealing with non-linear convergence patterns, dynamic restart estimate assignment and effective case sequencing. The application code also included time management measures, developed to make more efficient use of computational time.

A Progressive Parametric Study was conceptualized, with the goal of capturing the shifting influence of each of the 8 main parameters as more variables were added to the study. The domains of each parameter were based on the available literature and a series of experiments were devised, with increasing degrees of complexity, and taking into consideration different values of input power and burner length. What follows is a summary of the results of this optimization effort.

5.1.1 Result Summary

1D The excess air coefficient and the emissivity are the two most individually influential parameters. Scattering albedo has a modest influence, with a benefiting direct trend angle. Porosity and surface area have both an inverse impact on the interest parameters, doing better in terms of impact magnitude for lower burner lengths. The individual study of β shows promise of it playing a more important role in the achievement of a higher radiant efficient burner, due to the unpredictability and volatility of its behavior. Characteristic diameter has a weak influence, when compared to other parameters, and the impact of the thermal conductivity of the solid is negligible. The input power has a negative impact on the radiation efficiency, as seen in the literature, and negligible impact on the maximum solid temperature. The increase of the burner length increases slightly the radiant efficiency and the maximum temperature of the solid increases significantly.

2D The interactions between parameters can take one of two forms: linear combination, when the parameters are linearly independent (such as ϕ vs. ε and ω vs. λ), or distortion inducing, when one or both of the parameters introduce a change in the individual behavior of the other (d_{pc} vs. S_v or any combination with β). The effects of cross-influence in the distortion inducing combinations can swing the results toward either better or worse radiant efficiency, sometimes happening both for the same combination (ω vs. β). The input power, as found in the literature, is negatively correlated with the radiant efficiency and has little to no effect on the burner temperature. Increasing burner length leads to a significant increase of peak solid temperature and to a small increase in η_{rad} The shape of the combinations is not changed significantly across Q_{comb}, but suffers some impact from the burner length. $L = 1.0\ \mathrm{cm}$ enhances the ranges of η_{rad} and $T_{s,max}$ achieved by each parameter, however this increase is mostly toward lower radiant efficiencies. An improvement of the maximum solid temperature is also observed.

8D The behavior of power and length is confirmed. $Q_{comb} = 800\ \mathrm{kW}$ and $L = 2.0\ \mathrm{cm}$ is the best Power/Length combination for the purposes of the work. The excess air coefficient and the emissivity present a well delimited distribution on the interest quantities' domain, confirming their relevance. The extinction coefficient is paramount for the definition of the Pareto front and the Desirable zone. High values of scattering albedo severely penalize the performance of the burner. The characteristic pore diameter and solid thermal conductivity have no bearing on the interest quantities when compared to the other parameters; The impact of the porosity and specific surface area is not determinant to the performance outcome. Optimal performance and low peak solid temperatures are achieved with low λ, high ε, $\omega < 0.75$ and $\beta = 1.0\ \mathrm{cm}^{-1}$. Most of the determinant parameters exhibit robustness in the desirable values, allowing for design flexibility, with the exception of the extinction coefficient.

5.1.2 Concluding Remarks

The Progressive Parametric Study confirms the importance of the most influential parameters throughout all three stages. The excess air ratio and the emissivity have a high coefficient of variation ratio its relationship with η_{rad}: ($c_{v_r}(\eta_{rad}/\lambda)= 126.47$ and $c_{v_r}(\eta_{rad}/\varepsilon)= 46.78$, respectively, for the reference Power/Length combination, Table 4.6), which is maintained when other parameters are introduced in the analysis. The excess air ratio produces an enhancing effect on the impact of lower extinction coefficient values, which is mimicked in the full 8D parametric analysis. The extinction coefficient presents a weak impact on the interest quantities in the 1D analysis, but is prone to introduce cross-influences when combined with other parameters. One example is the combination with the scattering albedo, combination that both can lead to improvement or significant penalty on the radiant efficiency and peak solid temperature. Overall, excess air ratio, emissivity, extinction coefficient and scattering albedo are the parameters that are fundamental in order to achieve improvements in the PRB radiant performance. For the reference Power/Length combination an improvement of 50% in the radiant efficiency was obtained, for maximum solid temperatures below $1750\ \mathrm{K}$. It was also found that these trends do not change significantly with the power density of the burner, in opposition to the flame-holder length, which induces changes in the variables impact for shorter lengths.

5.2 Future Work

Following the multi-parametric analysis of PRBs presented in this dissertation, it would be of interest to study the influence of porous media with axially varying properties on the efficiency and durability of the burner. Also, an extension of this analysis to 3D models, in order to find which porous media geometric configurations would best reproduce the results obtained in this work.

Bibliography

[1] BP statistical review of world energy. Technical Report 67th Edition, BP p.l.c., June 2018.

[2] A. Pettinau, M. Mureddu, and F. Ferrara. Carbon dioxide conversion into liquid fuels by hydrogenation and photoelectrochemical reduction: Project description and preliminary experimental results. *Energy Procedia*, 114:6893 – 6904, 2017.

[3] P.-F. Hsu, J. Howell, and R. Matthews. A numerical investigation of premixed combustion within porous inert media. *Journal of Heat Transfer - Transactions of the Asme*, 115:744–750, 08 1993.

[4] J. Howell, M. Hall, and J. Ellzey. Combustion of hydrocarbon fuels within porous inert media. *Progress in Energy and Combustion Science*, 22(2):121 – 145, 1996.

[5] F. Durst and D. Trimis. Combustion by free flames versus combustion reactors. *Clean Air*, 3(1): 1–20, 2002.

[6] S. Wood and A. T. Harris. Porous burners for lean-burn applications. *Progress in Energy and Combustion Science*, 34(5):667 – 684, 2008.

[7] X. Zhou and J. Pereira. Numerical study of combustion and pollutants formation in inert nonhomogeneous porous media. *Combustion Science and Technology*, 130(1-6):335–364, 1997.

[8] R. G. V. Khanna and J. L. Ellzey. Measurements of emissions and radiation for methane combustion within a porous medium burner. *Combustion Science and Technology*, 99(1-3):133–142, 1994.

[9] W. M. Mathis and J. L. Ellzey. Flame stabilization, operating range, and emissions for a methane/air porous burner. *Combustion Science and Technology*, 175(5):825–839, 2003.

[10] S. Sathe, R. Peck, and T. Tong. A numerical analysis of heat transfer and combustion in porous radiant burners. *International Journal of Heat and Mass Transfer*, 33(6):1331 – 1338, 1990.

[11] S. Sathe, M. Kulkarni, R. Peck, and T. Tong. An experimental and theoretical study of porous radiant burner performance. *Twenty-Third Symposium (International) on Combustion*, 23(1):1011 – 1018, 1991.

[12] M. A. Mujeebu, M. Abdullah, M. A. Bakar, A. Mohamad, R. Muhad, and M. Abdullah. Combustion in porous media and its applications – a comprehensive survey. *Journal of Environmental Management*, 90(8):2287 – 2312, 2009.

[13] *M High Intensity Heater*. GoGaS Goch GmbH and Co. KG, Zum Ihnedieck 18, 44265 Dortmund, Germany.

[14] L. Younis and R. Viskanta. Experimental determination of the volumetric heat transfer coefficient between stream of air and ceramic foam. *International Journal of Heat and Mass Transfer*, 36(6): 1425 – 1434, 1993.

[15] R. V. X.Fu and J. Gore. Measurement and correlation of volumetric heat transfer coefficients of cellular ceramics. *Experimental Thermal and Fluid Science*, 17(4):285 – 293, 1998.

[16] M. A. Mendes, V. Skibina, P. Talukdar, R. Wulf, U. Gross, D. Trimis, and S. Ray. Experimental validation of simplified conduction–radiation models for evaluation of effective thermal conductivity of open-cell metal foams at high temperatures. *International Journal of Heat and Mass Transfer*, 78:112 – 120, 2014.

[17] G. Bianchi, S. Gianella, and A. Ortona. Design and additive manufacturing of periodic ceramic architectures. *Journal of Ceramic Science and Technology*, 8:59–66, 03 2017.

[18] M. Samoilenko. Design of porous medium burners by means of additive manufacturing. Master's thesis, École de Technologie Supérieure Université du Québec, 2018.

[19] A. Ortona, S. Pusterla, P. Fino, F. R. A. Mach, A. Delgado, and S. Biamino. Aging of reticulated Si-SiC foams in porous burners. *Advances in Applied Ceramics*, 109(4):246–251, 2010.

[20] M. Scheffler and P. Colombo. *Cellular Ceramics: Structure, Manufacturing, Properties and Applications*. Weinheim: Wiley-VCH, 2005.

[21] A. Horsman and K. Daun. Design optimization of a two-stage porous radiant burner through response surface modeling. *Numerical Heat Transfer; Part A: Applications*, 60(9):727–745, 2011.

[22] V. K. Mishra, S. C. Mishra, and D. N. Basu. Simultaneous estimation of parameters in analyzing porous medium combustion—assessment of seven optimization tools. *Numerical Heat Transfer, Part A: Applications*, 71(6):666–676, 2017.

[23] M. Mujeebu, M. Abdullah, A. Mohamad, and M. Bakar. Trends in modeling of porous media combustion. *Progress in Energy and Combustion Science*, 36(6):627–650, 2010.

[24] F. J Weinberg. Combustion temperatures: The future? *Nature*, 233:239–41, 10 1971.

[25] D. R. Hardesty and F. J. Weinberg. Burners producing large excess enthalpies. *Combustion Science and Technology*, 8(5-6):201–214, 1973.

[26] T. Takeno and K. Sato. An excess enthalpy flame theory. *Combustion Science and Technology*, 20 (1-2):73–84, 1979.

[27] T. Takeno, K. Sato, and K. Hase. A theoretical study on an excess enthalpy flame. *Eighteenth Symposium (International) on Combustion*, 18(1):465 – 472, 1981.

[28] T. Takeno and K. Hase. Effects of solid length and heat loss on an excess enthalpy flame. *Combustion Science and Technology*, 31(3-4):207–215, 1983.

[29] R. Echigo, K. Ichimiya, M. Kurusu, and Y. Yoshizawa. Combustion augmentation of extremely low calorific gases: application of the effective energy conversion method from gas enthalpy to thermal radiation. In *Proceedings of the ASME– JSME Thermal Engineering Joint Conference, Honululu*, volume 4, pages 99–104, 1983.

[30] M. M. Kamal and A. A. Mohamad. Combustion in porous media. *Proceedings of the Institution of Mechanical Engineers, Part A: Journal of Power and Energy*, 220(5):487–508, 2006.

[31] T. W. Tong and S. B. Sathe. Heat transfer characteristics of porous radiant burners. *Journal of Heat Transfer*, 113(2):423–428, 05 1991.

[32] P.-F. Hsu, W. D. Evans, and J. R. Howell. Experimental and numerical study of premixed combustion within nonhomogeneous porous ceramics. *Combustion Science and Technology*, 90(1-4):149–172, 1993.

[33] R. Mital, J. Gore, and R. Viskanta. A study of the structure of submerged reaction zone in porous ceramic radiant burners. *Combustion and Flame*, 111(3):175 – 184, 1997.

[34] X. Zhou and J. Pereira. Comparison of four combustion models for simulating the premixed combustion in inert porous media. *Fire and Materials*, 22(5):187–197, 1998.

[35] I. Malico and J. C. F. Pereira. Numerical study on the influence of radiative properties in porous media combustion. *Journal of Heat Transfer*, 123(5):951–957, 03 2001.

[36] E. M. D.J. Diamantis and D. Goussis. Simulations of premixed combustion in porous media. *Combustion Theory and Modelling*, 6(3):383–411, 2002.

[37] C. Keramiotis, B. Stelzner, D. Trimis, and M. Founti. Porous burners for low emission combustion: An experimental investigation. *Energy*, 45(1):213 – 219, 2012.

[38] C. Keramiotis, M. Katoufa, G. Vourliotakis, A. Hatziapostolou, and M. Founti. Experimental investigation of a radiant porous burner performance with simulated natural gas, biogas and synthesis gas fuel blends. *Fuel*, 158:835 – 842, 2015.

[39] S. A. Hashemi, M. Nikfar, and R. Motaghedifard. Experimental study of operating range and radiantion efficiency of a metal porous burner. *Thermal Science*, 19(1):11–20, 2015.

[40] H. S. Nejad, S. A. G. Nassab, and E. J. Javaran. Numerical study on radiant efficiency of a porous burner under different conditions. *Journal of Thermophysics and Heat Transfer*, 32(2):475–482, 2018.

[41] H. Liu, S. Dong, B.-W. Li, and H.-G. Chen. Parametric investigations of premixed methane–air combustion in two-section porous media by numerical simulation. *Fuel*, 89(7):1736 – 1742, 2010.

[42] J. Randrianalisoa, Y. Bréchet, and D. Baillis. Materials selection for optimal design of a porous radiant burner for environmentally driven requirements. *Advanced Engineering Materials*, 11(12): 1049–1056, 2009.

[43] P.-F. Hsu and J. R. Howell. Measurements of thermal conductivity and optical properties of porous partially stabilized zircoina. *Experimental Heat Transfer*, 5(4):293–313, 1992.

[44] B. Dietrich, T. Fischedick, S. Heissler, P. Weidler, C. Wöll, and M. Kind. Optical parameters for characterization of thermal radiation in ceramic sponges – experimental results and correlation. *International Journal of Heat and Mass Transfer*, 79:655 – 665, 2014.

[45] M. Kaviany. *Principles of heat transfer in porous media / M. Kaviany*. Springer-Verlag New York, 1991.

[46] M. Akbari and P. Riahi. Investigation of the structural and reactants properties on the thermal characteristics of a premixed porous burner. *Applied Energy*, 87(4):1433 – 1440, 2010.

[47] M. Mendes, J. Pereira, and J. Pereira. A numerical study of the stability of one-dimensional laminar premixed flames in inert porous media. *Combustion and Flame*, 153(4):525 – 539, 2008.

[48] M. J. Hall and J. P. Hiatt. Measurements of pore scale flows within and exiting ceramic foams. *Experiments in Fluids*, 20(6):433–440, Apr 1996.

[49] S. B. Sathe, R. E. Peck, and T. W. Tong. Flame stabilization and multimode heat transfer in inert porous media: A numerical study. *Combustion Science and Technology*, 70(4-6):93–109, 1990.

[50] S. R Turns. *An Introduction to Combustion: Concepts and Applications*. McGraw Hill Education Europe, London, United States, January 2000.

[51] R. Siegel and J. R. Howell. *Thermal radiation heat transfer*. Hemisphere Pub. Corp New York, 2d ed. edition, 1981.

[52] K.-A. Lie and B. T. Mallison. *Mathematical Models for Oil Reservoir Simulation*, pages 850–856. Springer Berlin Heidelberg, Berlin, Heidelberg, 2015.

[53] R. J Kee, J. F Grcar, M. D Smooke, J. A Miller, and E. Meeks. *PREMIX: a fortran program for modeling steady laminar one-dimensional premixed flames*. Sandia National Laboratories, 01 1985.

[54] M. Kulkarni and R. Peck. Analysis of a bilayered porous radiant burner. *Numerical Heat Transfer, Part A: Applications*, 30(3):219–232, 1996.

[55] R. Kee, F. Rupley, and J. Miller. *Chemkin-II: A Fortran chemical kinetics package for the analysis of gas-phase chemical kinetics*. Sandia National Laboratories, 9 1989.

[56] R. J. Kee, G. Dixon-lewis, J. Warnatz, M. Coltrin, and J. A. Miller. *A Fortran Computer Code Package For The Evaluation Of Gas-Phase, Multicomponent Transport Properties*. Sandia National Laboratories, 08 1996.

[57] C. Sung, C. Law, and J.-Y. Chen. An augmented reduced mechanism for methane oxidation with comprehensive global parametric validation. *Twenty-Seventh Symposium (International) on Combustion*, 27(1):295 – 304, 1998.

[58] S. Mey-Cloutier, C. Caliot, A. Kribus, Y. Gray, and G. Flamant. Experimental study of ceramic foams used as high temperature volumetric solar absorber. *Solar Energy*, 136:226 – 235, 2016.

[59] V. Gnielinski. New equations for heat and mass transfer in turbulent pipe and channel flow. *International Chemical Engineering*, 16:359–368, 1976.

[60] M. F. Modest. *Radiative Heat Transfer*. Academic Press, Boston, third edition, 2013.

[61] J. Buckmaster and T. Takeno. Blow-off and flashback of an excess enthalpy flame. *Combustion Science and Technology*, 25(3-4):153–158, 1981.

[62] P.-F. Hsu and R. Matthews. The necessity of using detailed kinetics in models for premixed combustion within porous media. *Combustion and Flame*, 93(4):457–466, 1993.

[63] M. Mendes. *Modeling and Simulation of Hydrocarbon Oxidation Processes within Porous Inert Media*. PhD thesis, Instituto Superior Técnico, Lisbon, 2010.

[64] D. Trimis and F. Durst. Combustion in a porous medium-advances and applications. *Combustion Science and Technology*, 121(1-6):153–168, 1996.

Appendix A

Progressive Parametric Study plots

A.1 2D Parametric Combinations Plots

A.1.1 Parametric Interactions

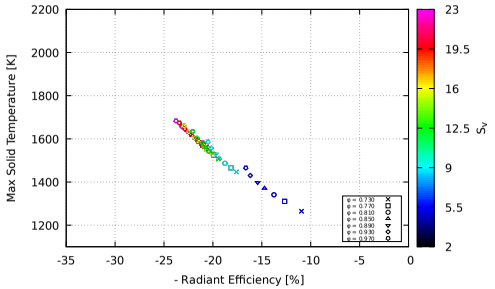

(a) $Q_{comb} = 800$ W and $L = 1.0$ cm.

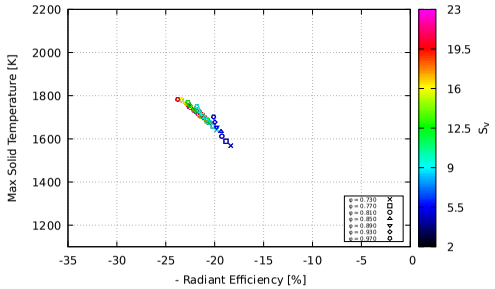

(b) $Q_{comb} = 800$ kW and $L = 2.0$ cm.

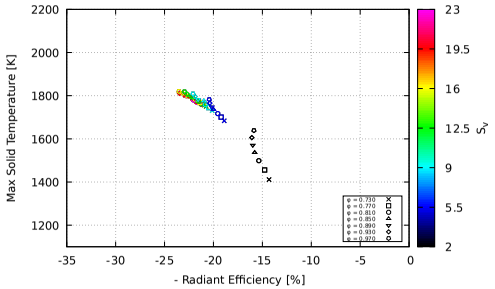

(c) $Q_{comb} = 800$ kW and $L = 3.0$ cm.

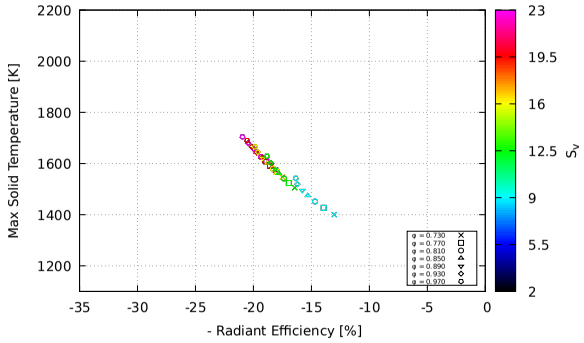

(d) $Q_{comb} = 1000$ kW and $L = 1.0$ cm.

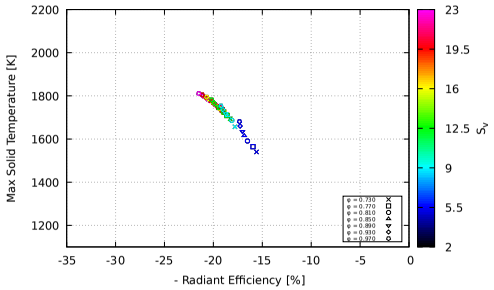

(e) $Q_{comb} = 1000$ kW and $L = 2.0$ cm.

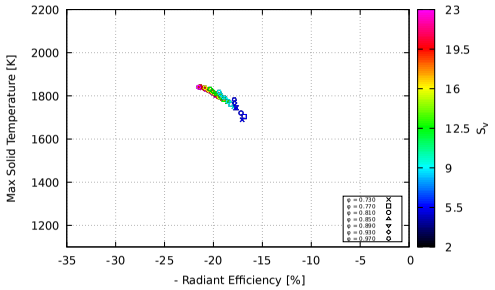

(f) $Q_{comb} = 1000$ kW and $L = 3.0$ cm.

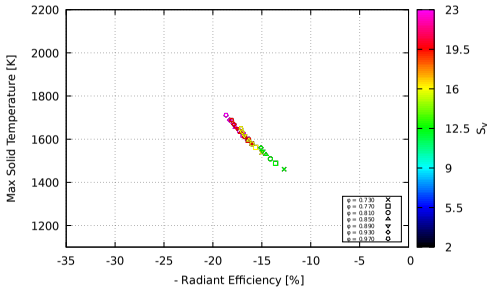

(g) $Q_{comb} = 1200$ kW and $L = 1.0$ cm.

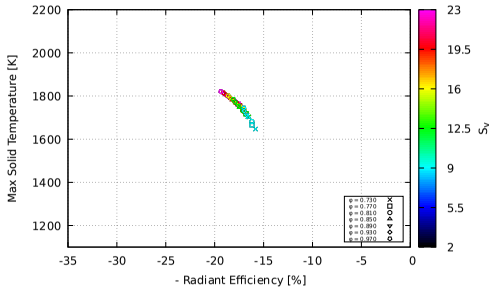

(h) $Q_{comb} = 1200$ kW and $L = 2.0$ cm.

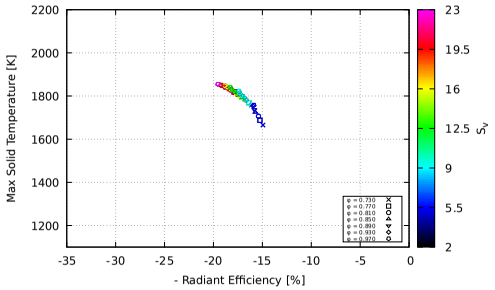

(i) $Q_{comb} = 1200$ kW and $L = 3.0$ cm.

Figure A.1: Interaction between ϕ and S_v across Power/Length combinations.

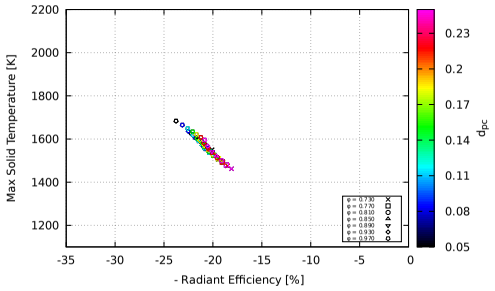

(a) $Q_{comb} = 800$ W and $L = 1.0$ cm.

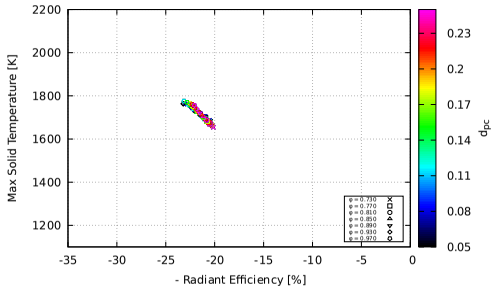

(b) $Q_{comb} = 800$ kW and $L = 2.0$ cm.

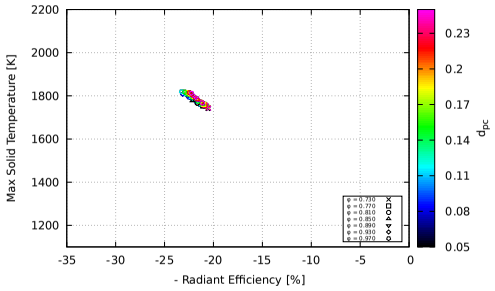

(c) $Q_{comb} = 800$ kW and $L = 3.0$ cm.

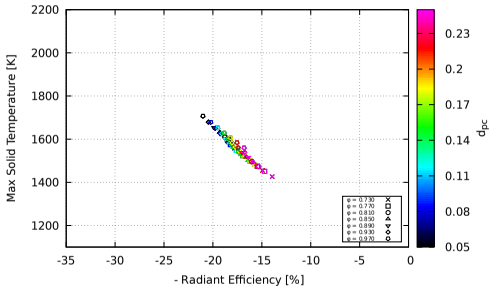

(d) $Q_{comb} = 1000$ kW and $L = 1.0$ cm.

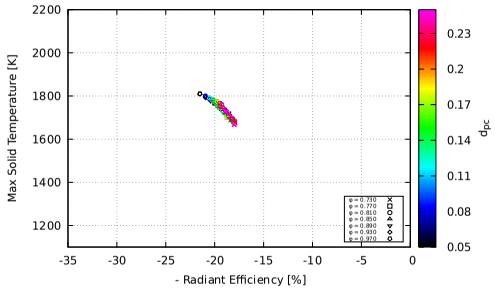

(e) $Q_{comb} = 1000$ kW and $L = 2.0$ cm.

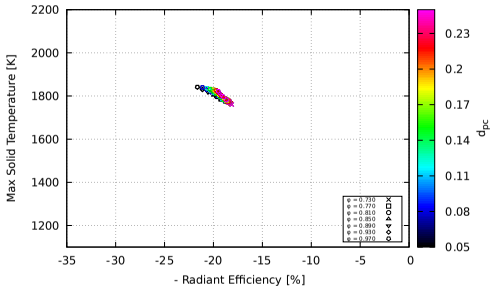

(f) $Q_{comb} = 1000$ kW and $L = 3.0$ cm.

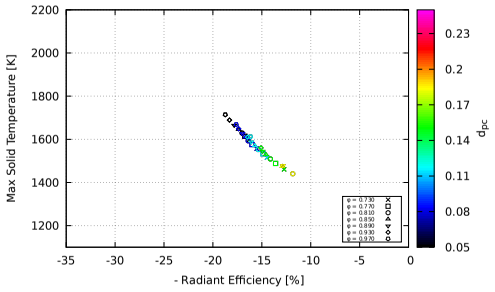

(g) $Q_{comb} = 1200$ kW and $L = 1.0$ cm.

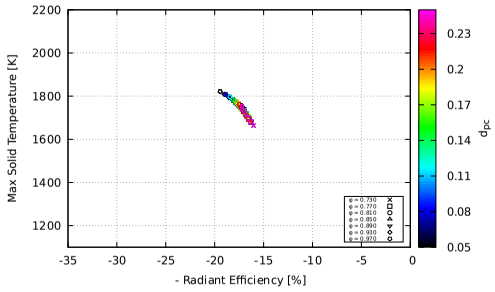

(h) $Q_{comb} = 1200$ kW and $L = 2.0$ cm.

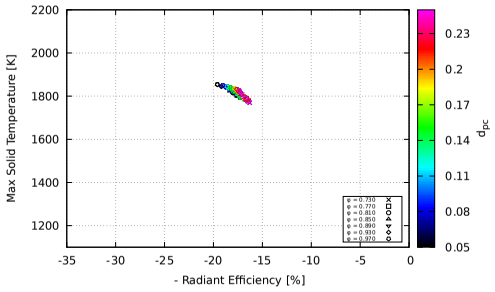

(i) $Q_{comb} = 1200$ kW and $L = 3.0$ cm.

Figure A.2: Interaction between ϕ and d_{pc} across Power/Length combinations.

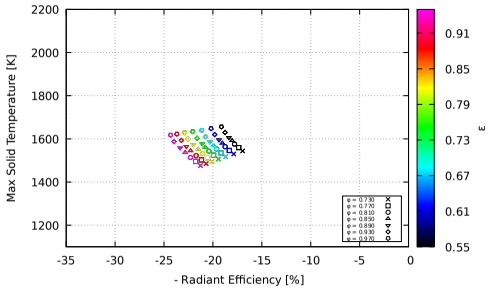

(a) $Q_{comb} = 800$ W and $L = 1.0$ cm.

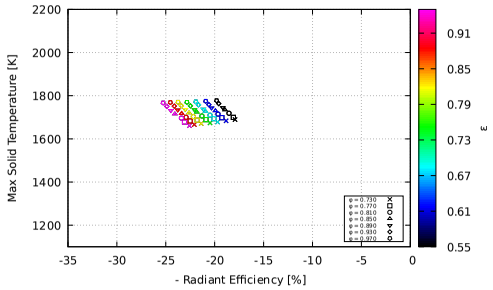

(b) $Q_{comb} = 800$ kW and $L = 2.0$ cm.

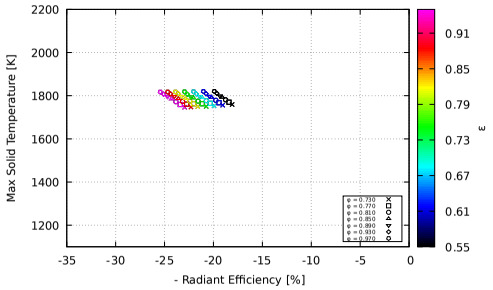

(c) $Q_{comb} = 800$ kW and $L = 3.0$ cm.

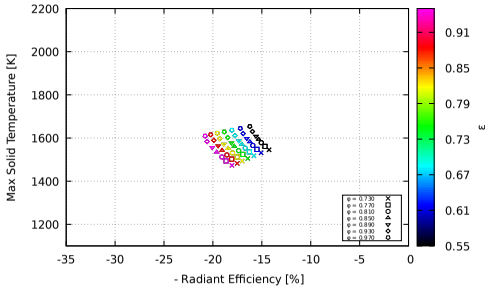

(d) $Q_{comb} = 1000$ kW and $L = 1.0$ cm.

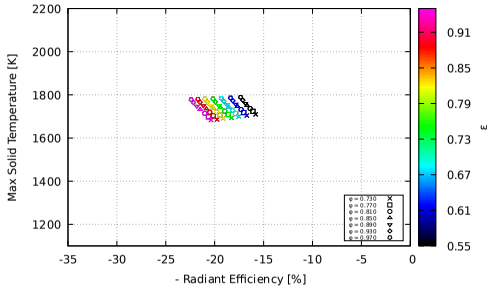

(e) $Q_{comb} = 1000$ kW and $L = 2.0$ cm.

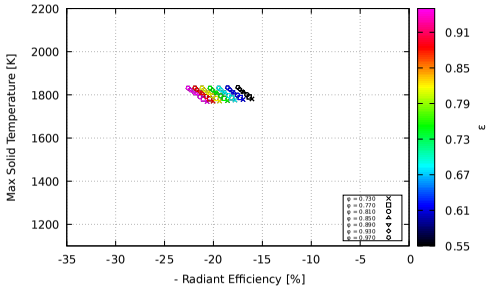

(f) $Q_{comb} = 1000$ kW and $L = 3.0$ cm.

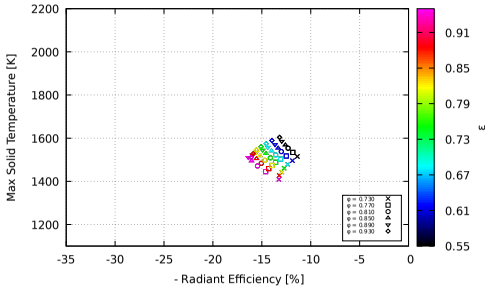

(g) $Q_{comb} = 1200$ kW and $L = 1.0$ cm.

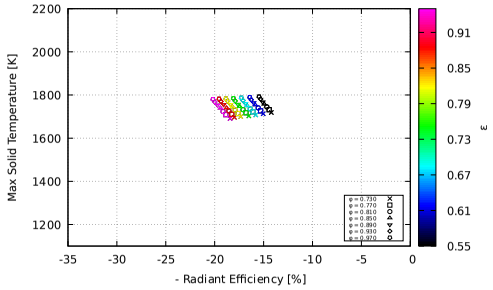

(h) $Q_{comb} = 1200$ kW and $L = 2.0$ cm.

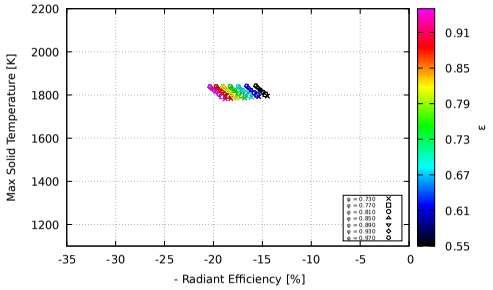

(i) $Q_{comb} = 1200$ kW and $L = 3.0$ cm.

Figure A.3: Interaction between ϕ and ε across Power/Length combinations.

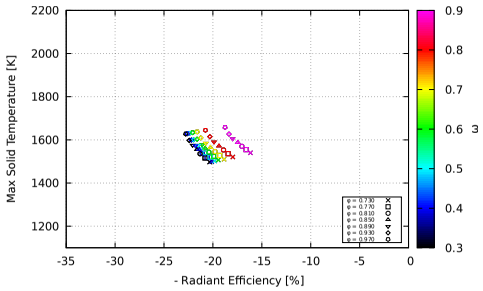

(a) $Q_{comb} = 800$ W and $L = 1.0$ cm.

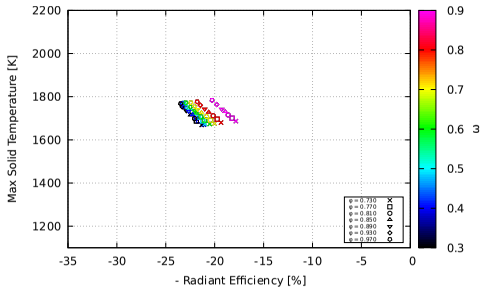

(b) $Q_{comb} = 800$ kW and $L = 2.0$ cm.

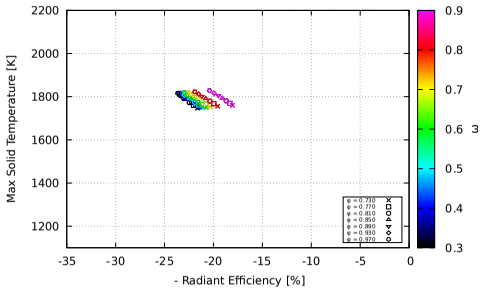

(c) $Q_{comb} = 800$ kW and $L = 3.0$ cm.

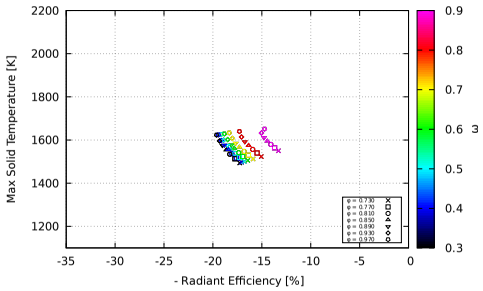

(d) $Q_{comb} = 1000$ kW and $L = 1.0$ cm.

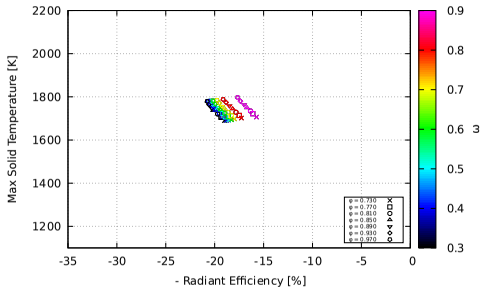

(e) $Q_{comb} = 1000$ kW and $L = 2.0$ cm.

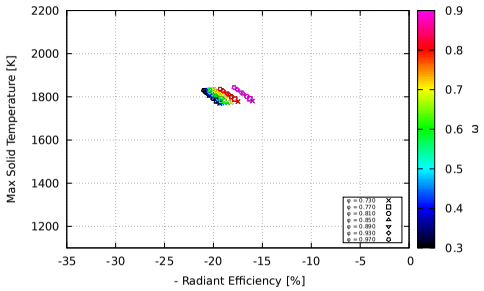

(f) $Q_{comb} = 1000$ kW and $L = 3.0$ cm.

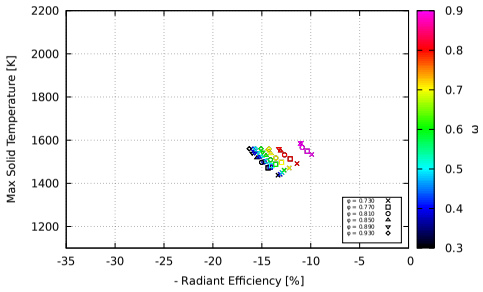

(g) $Q_{comb} = 1200$ kW and $L = 1.0$ cm.

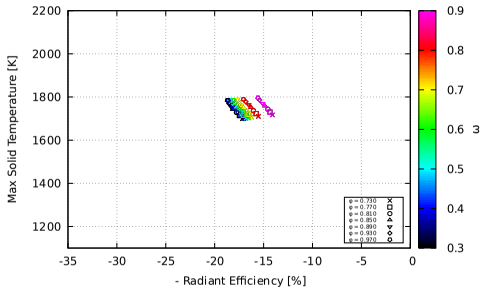

(h) $Q_{comb} = 1200$ kW and $L = 2.0$ cm.

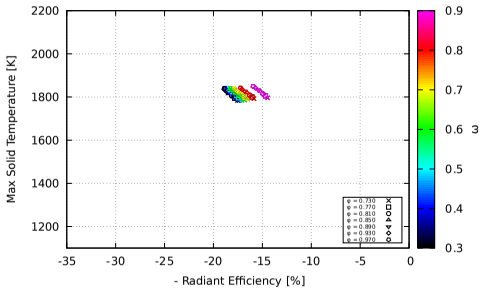

(i) $Q_{comb} = 1200$ kW and $L = 3.0$ cm.

Figure A.4: Interaction between ϕ and ω across Power/Length combinations.

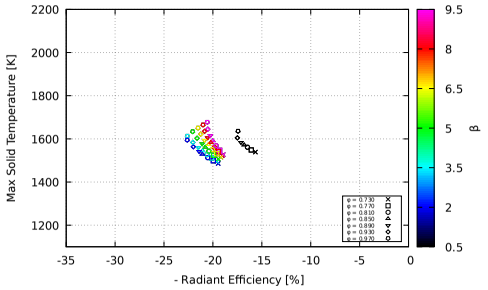

(a) $Q_{comb} = 800$ W and $L = 1.0$ cm.

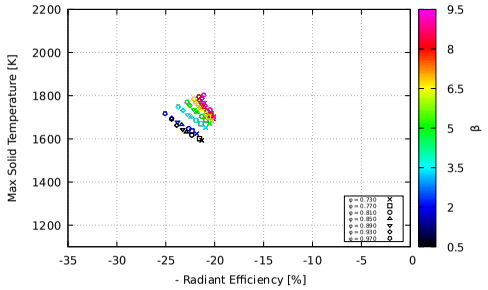

(b) $Q_{comb} = 800$ kW and $L = 2.0$ cm.

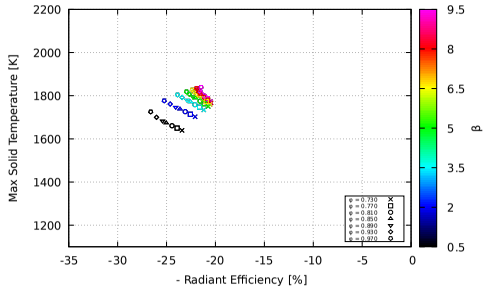

(c) $Q_{comb} = 800$ kW and $L = 3.0$ cm.

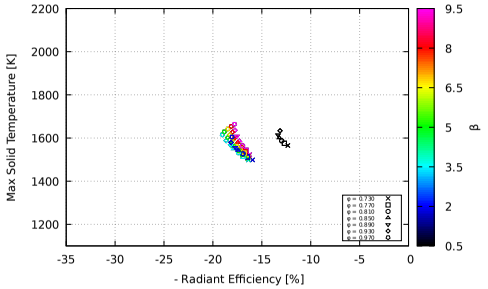

(d) $Q_{comb} = 1000$ kW and $L = 1.0$ cm.

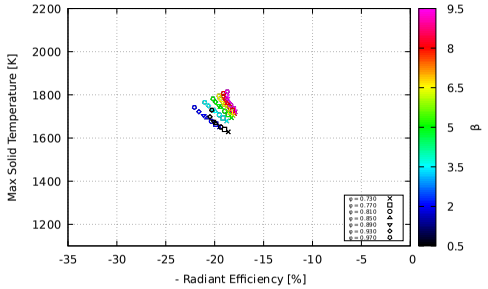

(e) $Q_{comb} = 1000$ kW and $L = 2.0$ cm.

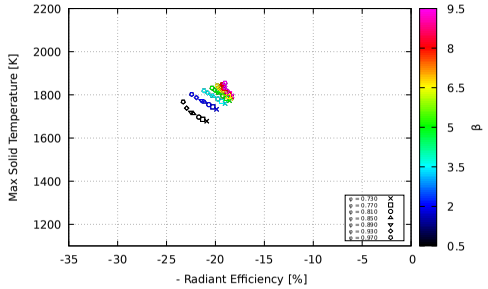

(f) $Q_{comb} = 1000$ kW and $L = 3.0$ cm.

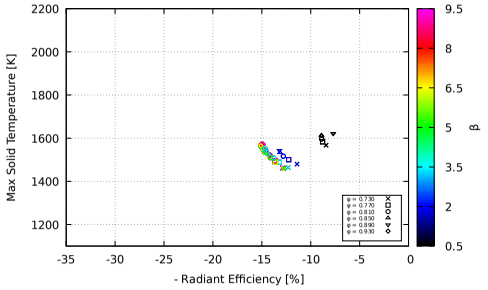

(g) $Q_{comb} = 1200$ kW and $L = 1.0$ cm.

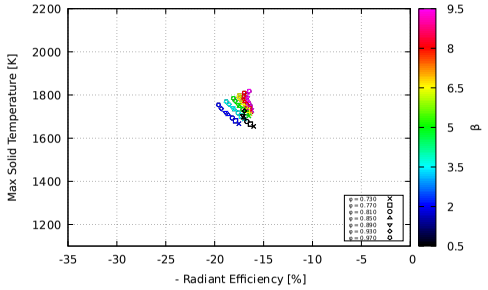

(h) $Q_{comb} = 1200$ kW and $L = 2.0$ cm.

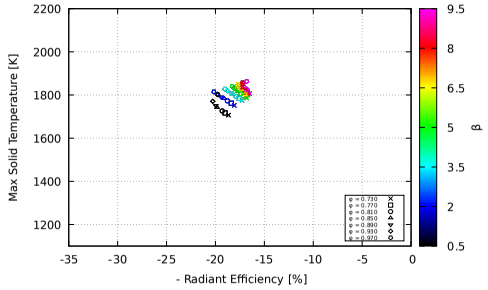

(i) $Q_{comb} = 1200$ kW and $L = 3.0$ cm.

Figure A.5: Interaction between ϕ and β across Power/Length combinations.

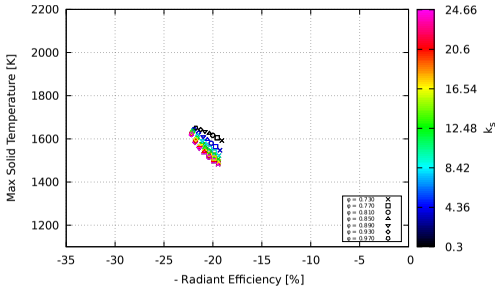

(a) $Q_{comb} = 800$ W and $L = 1.0$ cm.

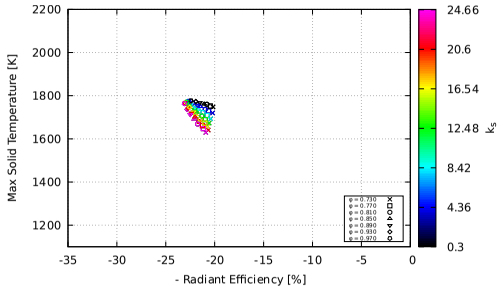

(b) $Q_{comb} = 800$ kW and $L = 2.0$ cm.

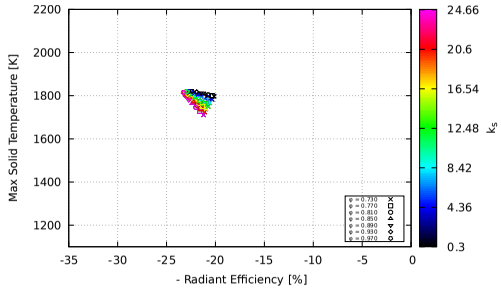

(c) $Q_{comb} = 800$ kW and $L = 3.0$ cm.

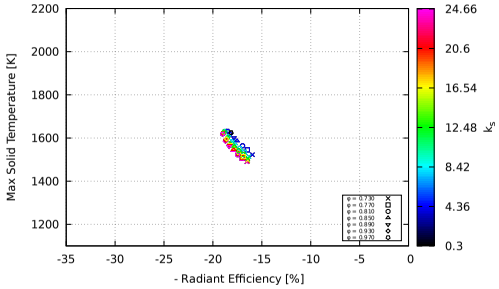

(d) $Q_{comb} = 1000$ kW and $L = 1.0$ cm.

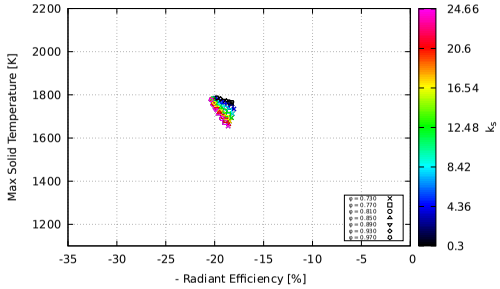

(e) $Q_{comb} = 1000$ kW and $L = 2.0$ cm.

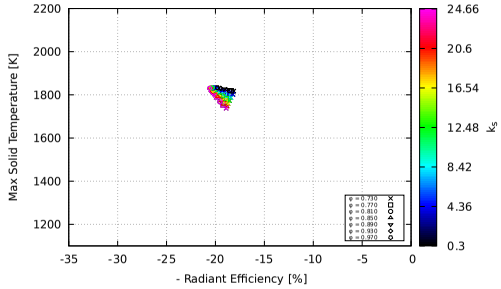

(f) $Q_{comb} = 1000$ kW and $L = 3.0$ cm.

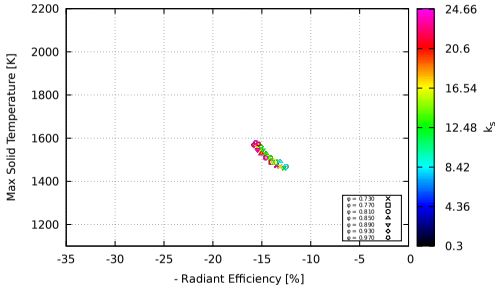

(g) $Q_{comb} = 1200$ kW and $L = 1.0$ cm.

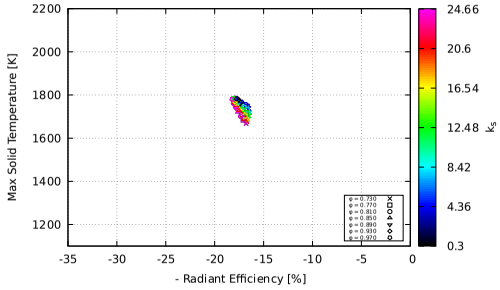

(h) $Q_{comb} = 1200$ kW and $L = 2.0$ cm.

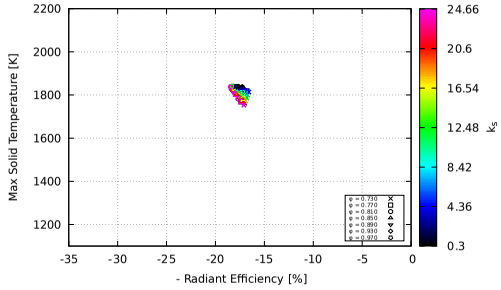

(i) $Q_{comb} = 1200$ kW and $L = 3.0$ cm.

Figure A.6: Interaction between ϕ and k_s across Power/Length combinations.

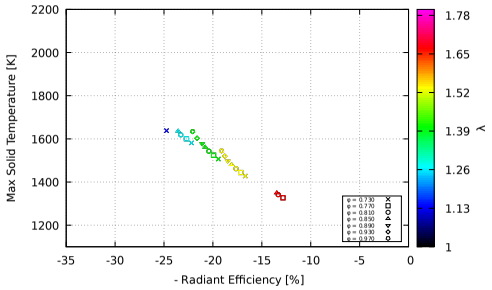

(a) $Q_{comb} = 800$ W and $L = 1.0$ cm.

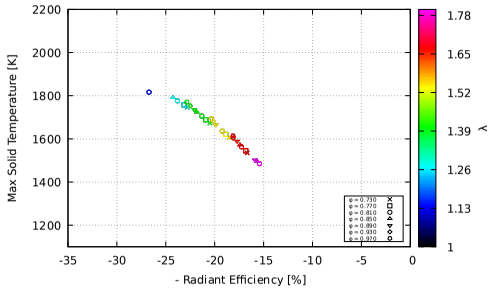

(b) $Q_{comb} = 800$ kW and $L = 2.0$ cm.

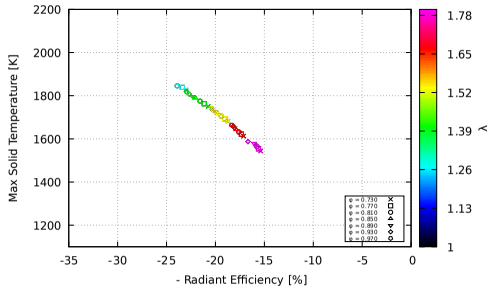

(c) $Q_{comb} = 800$ kW and $L = 3.0$ cm.

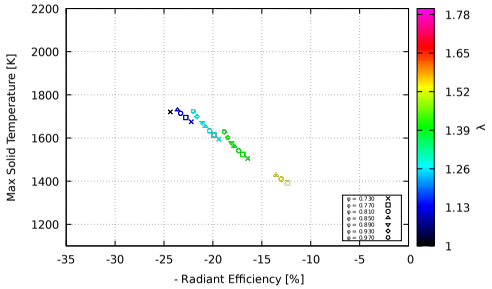

(d) $Q_{comb} = 1000$ kW and $L = 1.0$ cm.

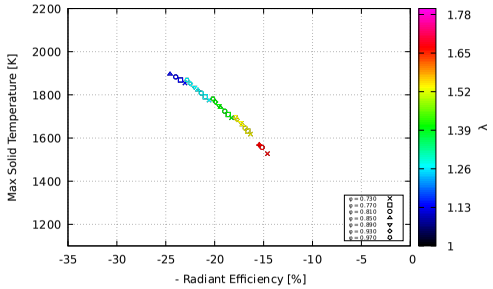

(e) $Q_{comb} = 1000$ kW and $L = 2.0$ cm.

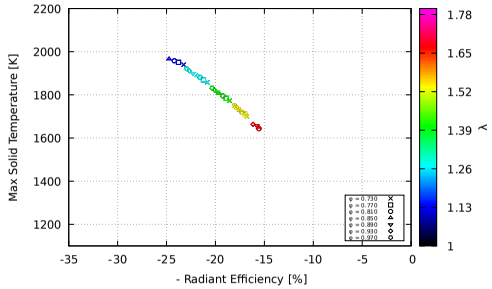

(f) $Q_{comb} = 1000$ kW and $L = 3.0$ cm.

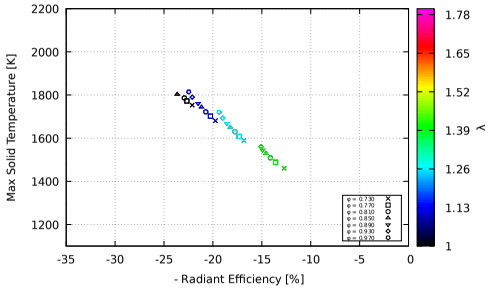

(g) $Q_{comb} = 1200$ kW and $L = 1.0$ cm.

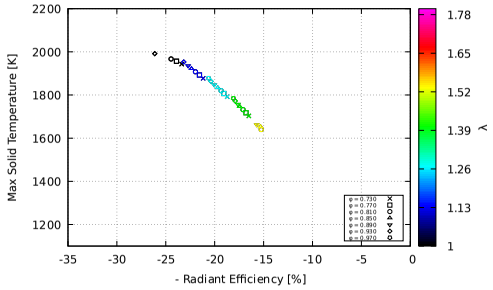

(h) $Q_{comb} = 1200$ kW and $L = 2.0$ cm.

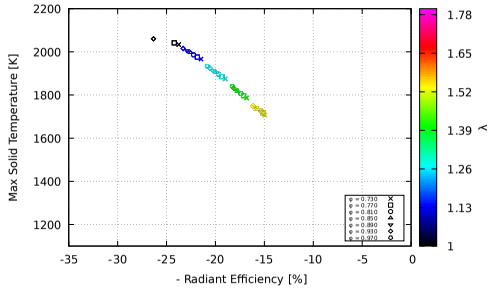

(i) $Q_{comb} = 1200$ kW and $L = 3.0$ cm.

Figure A.7: Interaction between ϕ and λ across Power/Length combinations.

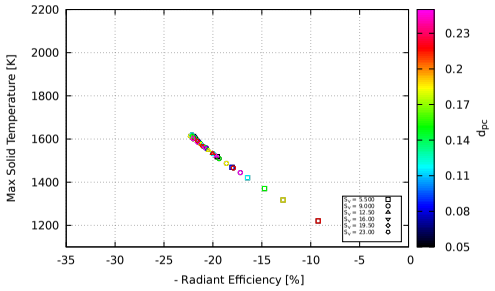

(a) $Q_{comb} = 800$ W and $L = 1.0$ cm.

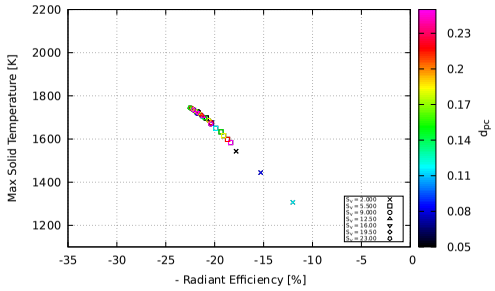

(b) $Q_{comb} = 800$ kW and $L = 2.0$ cm.

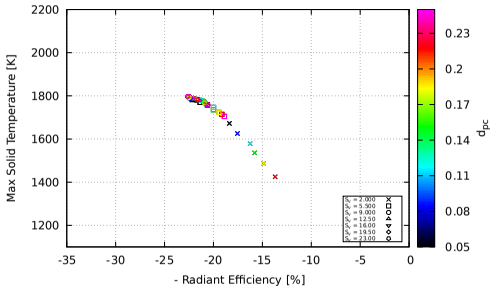

(c) $Q_{comb} = 800$ kW and $L = 3.0$ cm.

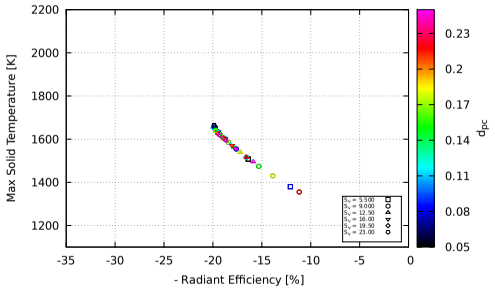

(d) $Q_{comb} = 1000$ kW and $L = 1.0$ cm.

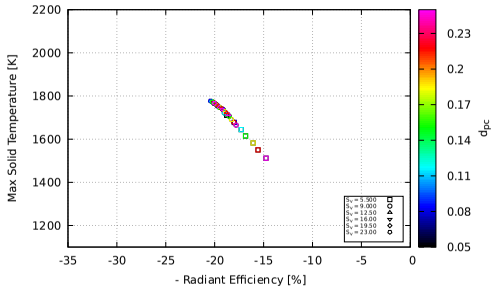

(e) $Q_{comb} = 1000$ kW and $L = 2.0$ cm.

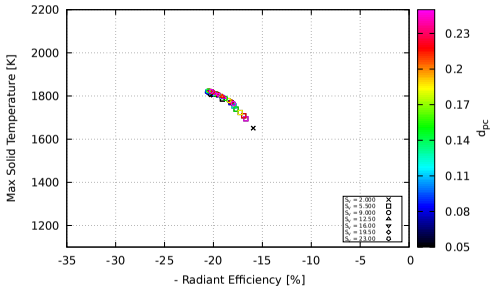

(f) $Q_{comb} = 1000$ kW and $L = 3.0$ cm.

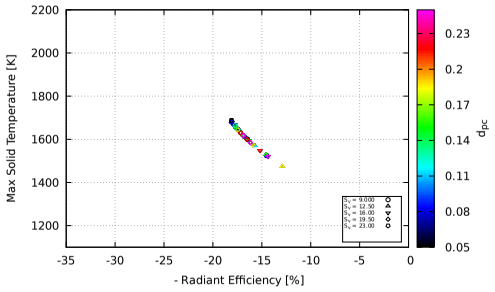

(g) $Q_{comb} = 1200$ kW and $L = 1.0$ cm.

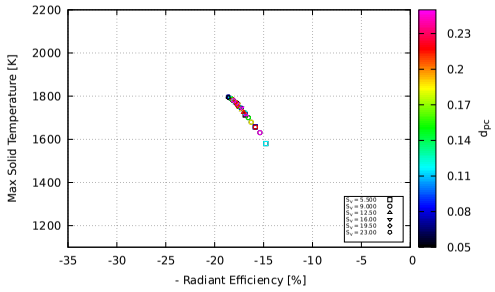

(h) $Q_{comb} = 1200$ kW and $L = 2.0$ cm.

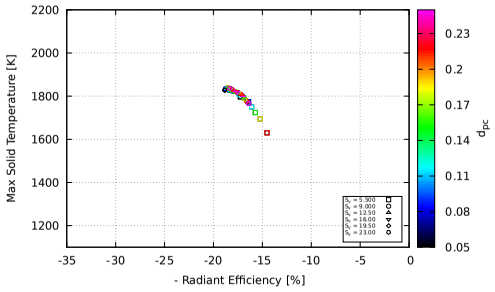

(i) $Q_{comb} = 1200$ kW and $L = 3.0$ cm.

Figure A.8: Interaction between S_v and d_{pc} across Power/Length combinations.

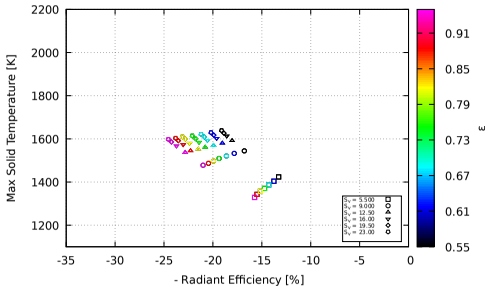

(a) $Q_{comb} = 800$ W and $L = 1.0$ cm.

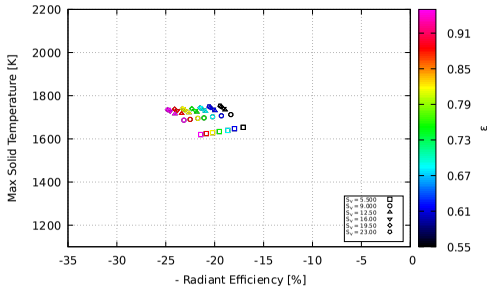

(b) $Q_{comb} = 800$ kW and $L = 2.0$ cm.

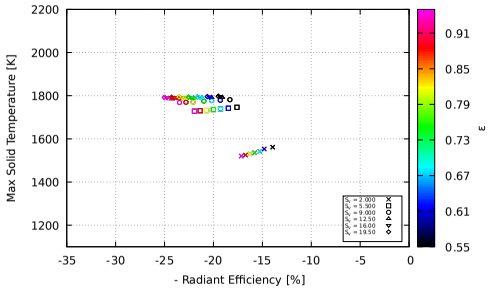

(c) $Q_{comb} = 800$ kW and $L = 3.0$ cm.

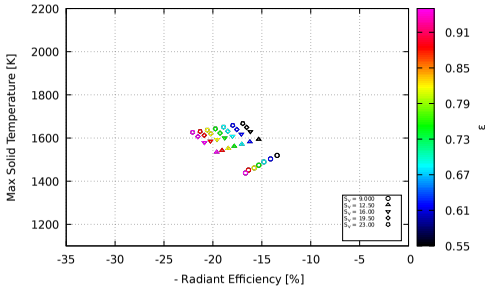

(d) $Q_{comb} = 1000$ kW and $L = 1.0$ cm.

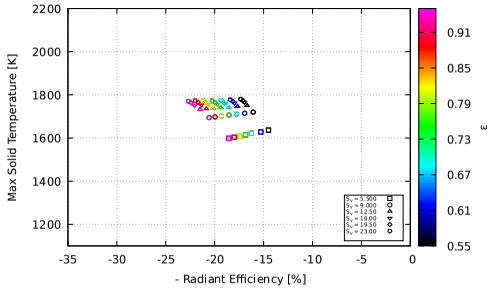

(e) $Q_{comb} = 1000$ kW and $L = 2.0$ cm.

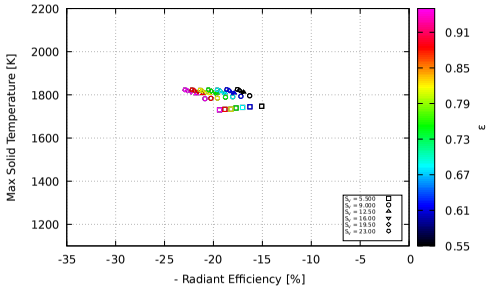

(f) $Q_{comb} = 1000$ kW and $L = 3.0$ cm.

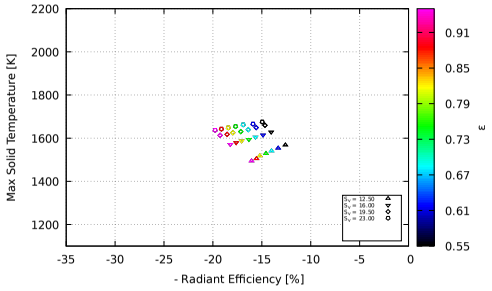

(g) $Q_{comb} = 1200$ kW and $L = 1.0$ cm.

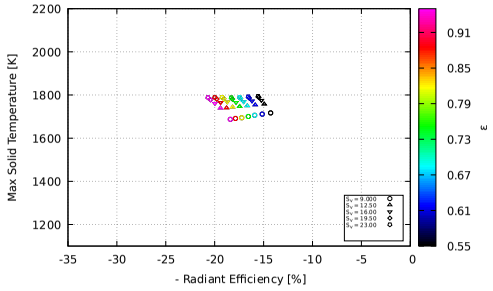

(h) $Q_{comb} = 1200$ kW and $L = 2.0$ cm.

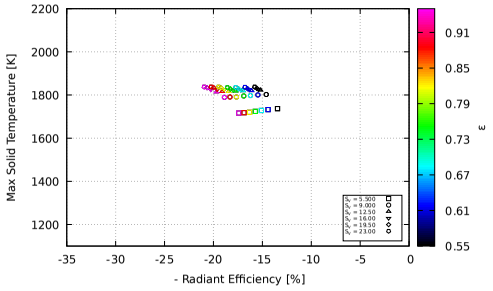

(i) $Q_{comb} = 1200$ kW and $L = 3.0$ cm.

Figure A.9: Interaction between S_v and ε across Power/Length combinations.

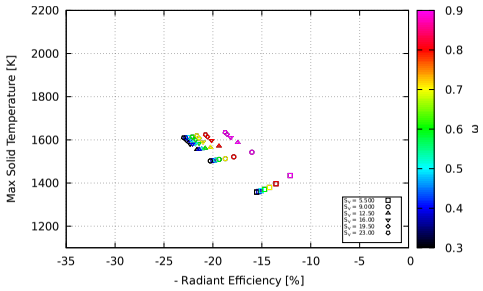

(a) $Q_{comb} = 800$ W and $L = 1.0$ cm.

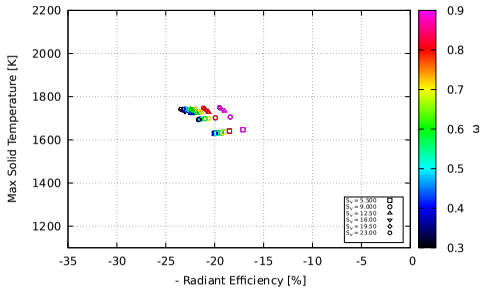

(b) $Q_{comb} = 800$ kW and $L = 2.0$ cm.

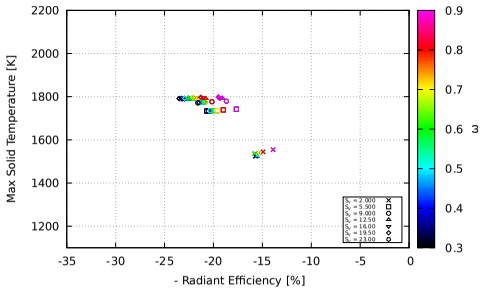

(c) $Q_{comb} = 800$ kW and $L = 3.0$ cm.

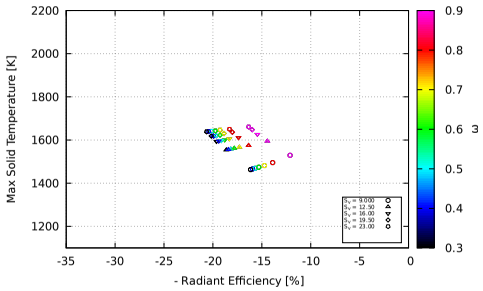

(d) $Q_{comb} = 1000$ kW and $L = 1.0$ cm.

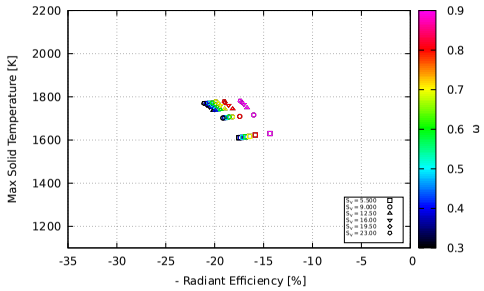

(e) $Q_{comb} = 1000$ kW and $L = 2.0$ cm.

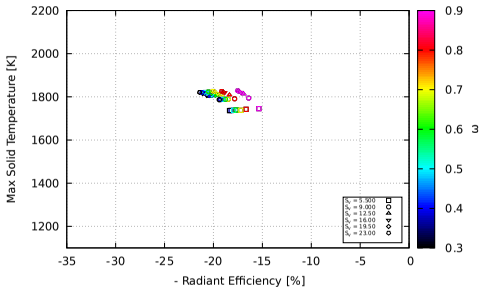

(f) $Q_{comb} = 1000$ kW and $L = 3.0$ cm.

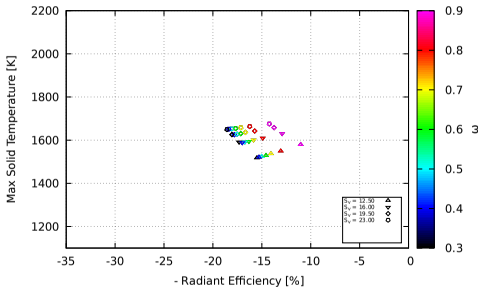

(g) $Q_{comb} = 1200$ kW and $L = 1.0$ cm.

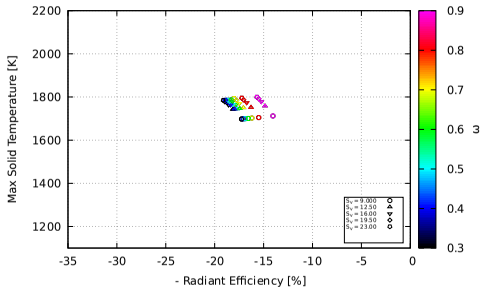

(h) $Q_{comb} = 1200$ kW and $L = 2.0$ cm.

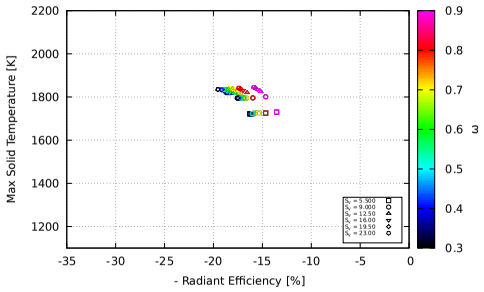

(i) $Q_{comb} = 1200$ kW and $L = 3.0$ cm.

Figure A.10: Interaction between S_v and ω across Power/Length combinations.

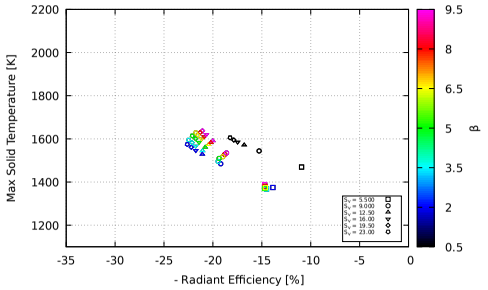

(a) $Q_{comb} = 800$ W and $L = 1.0$ cm.

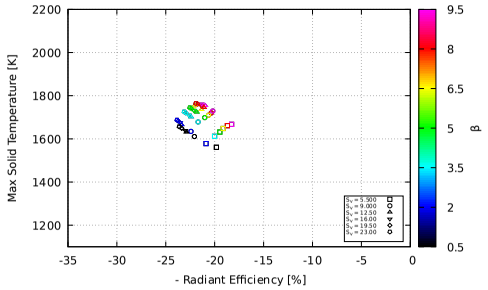

(b) $Q_{comb} = 800$ kW and $L = 2.0$ cm.

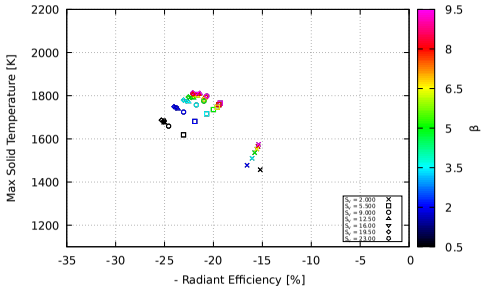

(c) $Q_{comb} = 800$ kW and $L = 3.0$ cm.

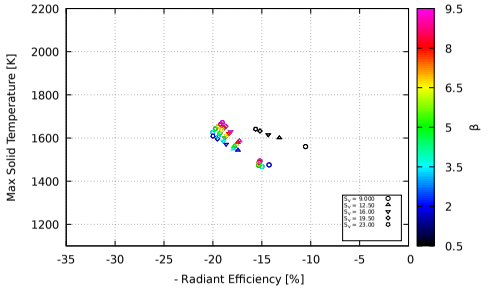

(d) $Q_{comb} = 1000$ kW and $L = 1.0$ cm.

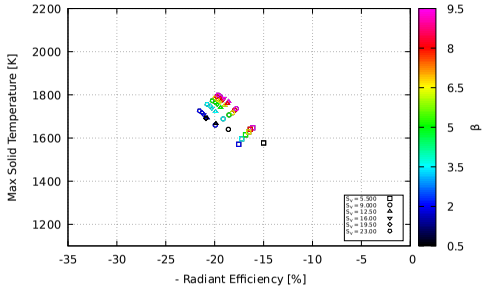

(e) $Q_{comb} = 1000$ kW and $L = 2.0$ cm.

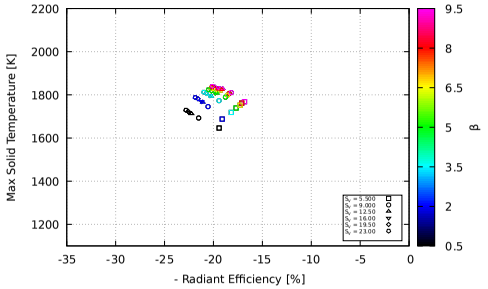

(f) $Q_{comb} = 1000$ kW and $L = 3.0$ cm.

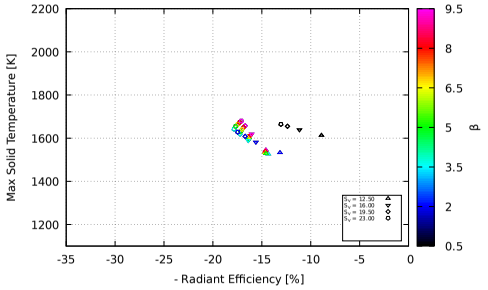

(g) $Q_{comb} = 1200$ kW and $L = 1.0$ cm.

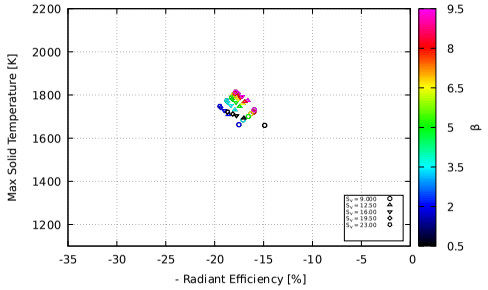

(h) $Q_{comb} = 1200$ kW and $L = 2.0$ cm.

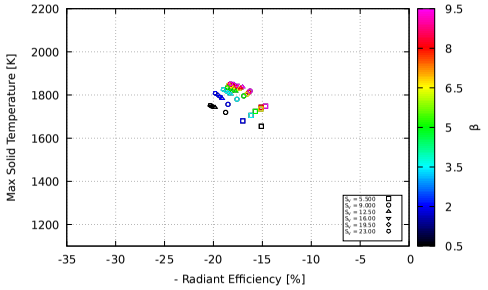

(i) $Q_{comb} = 1200$ kW and $L = 3.0$ cm.

Figure A.11: Interaction between S_v and β across Power/Length combinations.

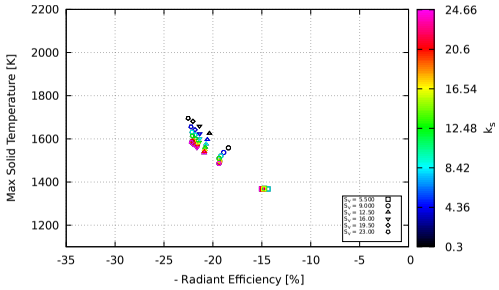

(a) $Q_{comb} = 800$ W and $L = 1.0$ cm.

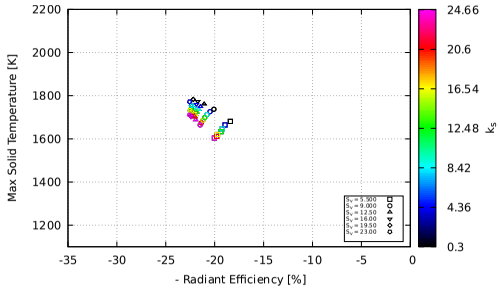

(b) $Q_{comb} = 800$ kW and $L = 2.0$ cm.

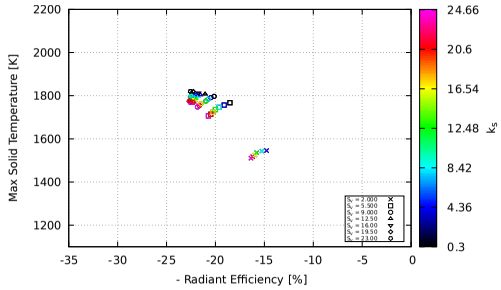

(c) $Q_{comb} = 800$ kW and $L = 3.0$ cm.

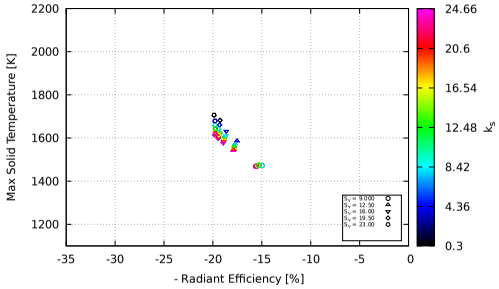

(d) $Q_{comb} = 1000$ kW and $L = 1.0$ cm.

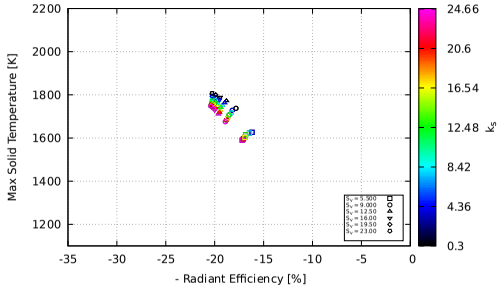

(e) $Q_{comb} = 1000$ kW and $L = 2.0$ cm.

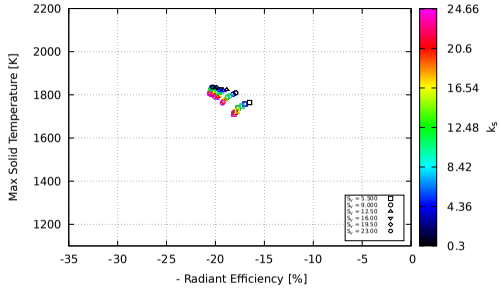

(f) $Q_{comb} = 1000$ kW and $L = 3.0$ cm.

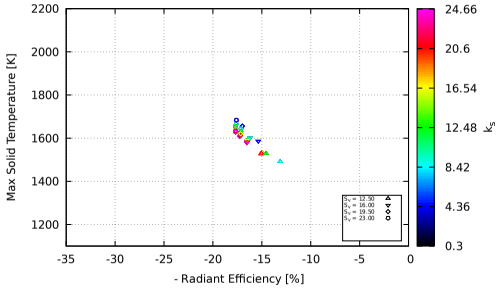

(g) $Q_{comb} = 1200$ kW and $L = 1.0$ cm.

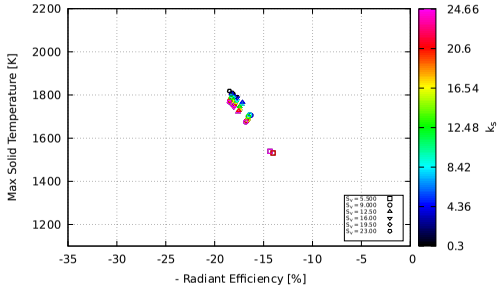

(h) $Q_{comb} = 1200$ kW and $L = 2.0$ cm.

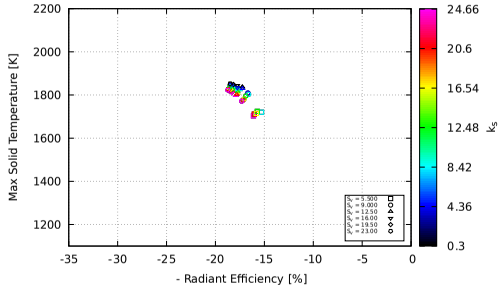

(i) $Q_{comb} = 1200$ kW and $L = 3.0$ cm.

Figure A.12: Interaction between S_v and k_s across Power/Length combinations.

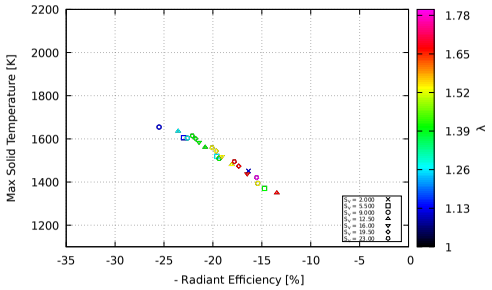

(a) $Q_{comb} = 800$ W and $L = 1.0$ cm.

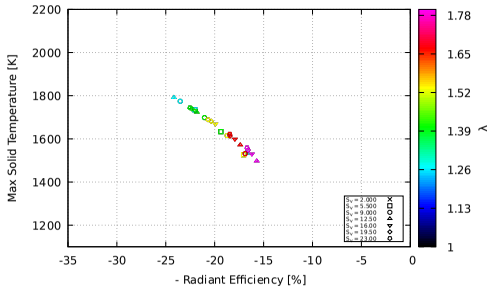

(b) $Q_{comb} = 800$ kW and $L = 2.0$ cm.

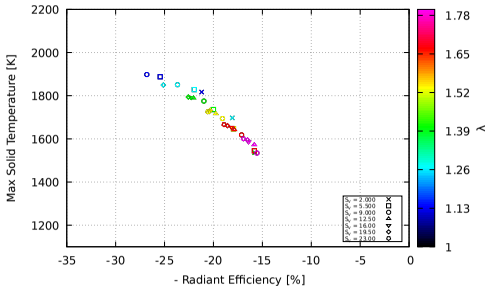

(c) $Q_{comb} = 800$ kW and $L = 3.0$ cm.

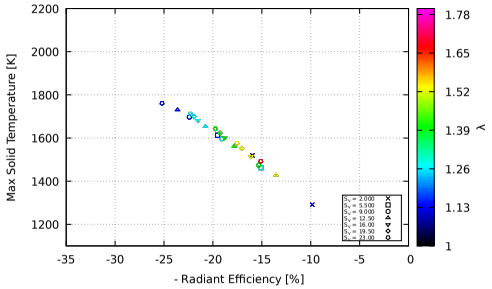

(d) $Q_{comb} = 1000$ kW and $L = 1.0$ cm.

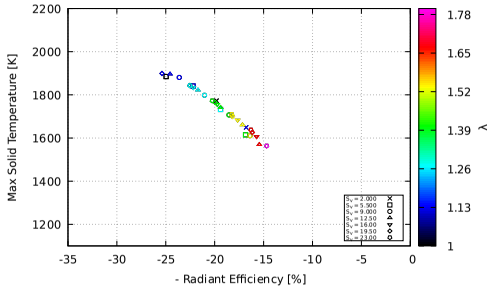

(e) $Q_{comb} = 1000$ kW and $L = 2.0$ cm.

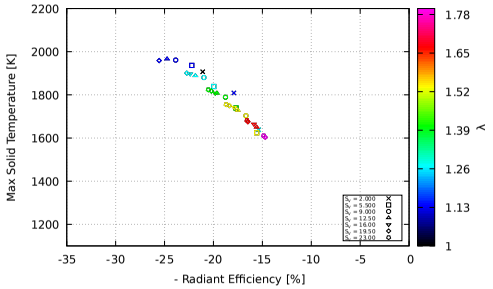

(f) $Q_{comb} = 1000$ kW and $L = 3.0$ cm.

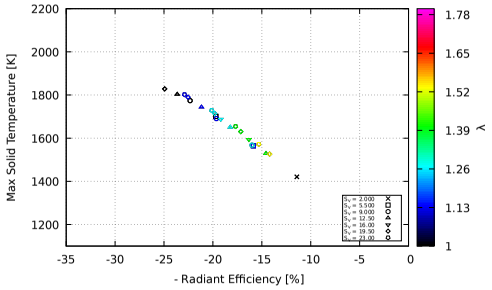

(g) $Q_{comb} = 1200$ kW and $L = 1.0$ cm.

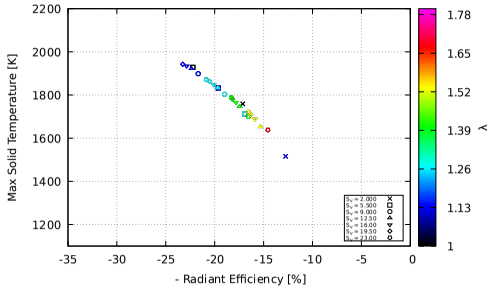

(h) $Q_{comb} = 1200$ kW and $L = 2.0$ cm.

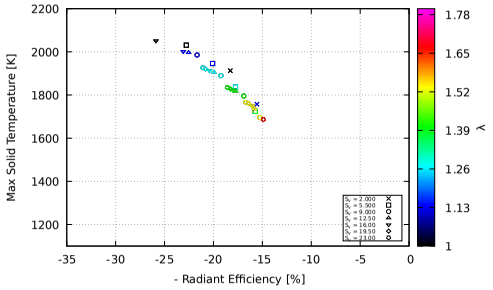

(i) $Q_{comb} = 1200$ kW and $L = 3.0$ cm.

Figure A.13: Interaction between S_v and λ across Power/Length combinations.

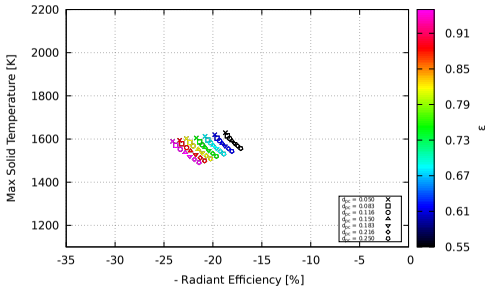

(a) $Q_{comb} = 800$ W and $L = 1.0$ cm.

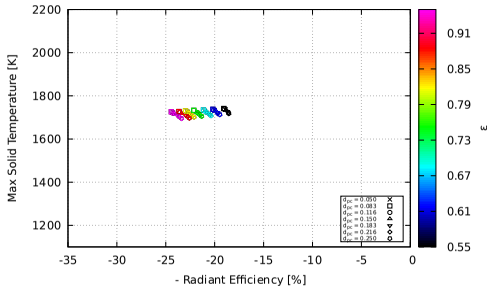

(b) $Q_{comb} = 800$ kW and $L = 2.0$ cm.

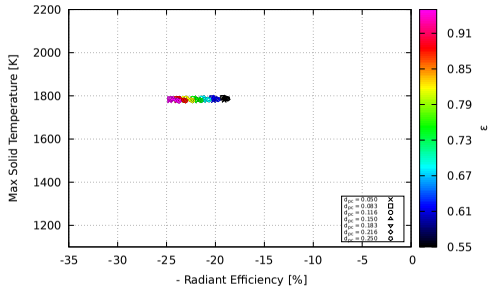

(c) $Q_{comb} = 800$ kW and $L = 3.0$ cm.

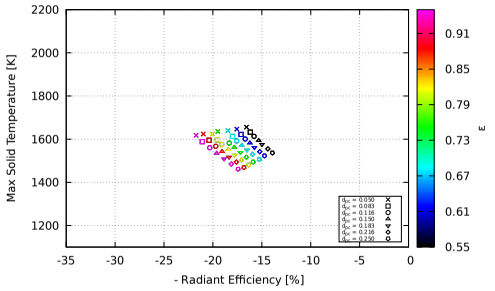

(d) $Q_{comb} = 1000$ kW and $L = 1.0$ cm.

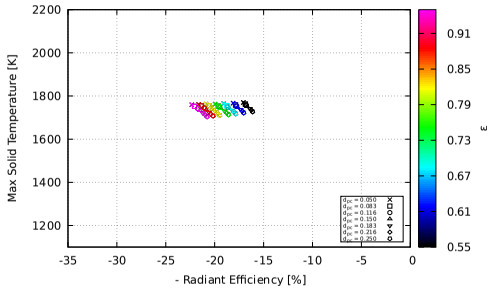

(e) $Q_{comb} = 1000$ kW and $L = 2.0$ cm.

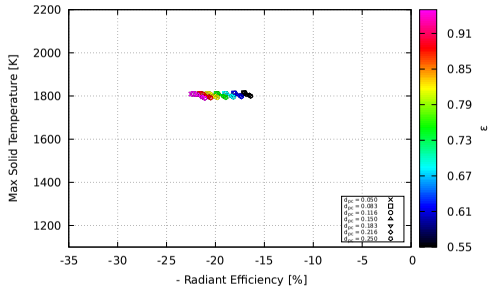

(f) $Q_{comb} = 1000$ kW and $L = 3.0$ cm.

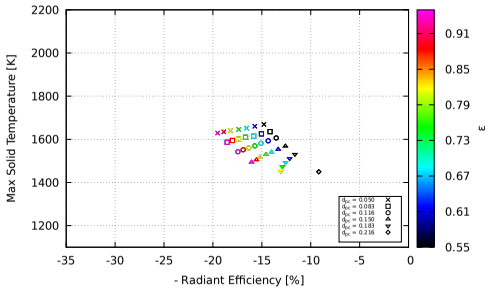

(g) $Q_{comb} = 1200$ kW and $L = 1.0$ cm.

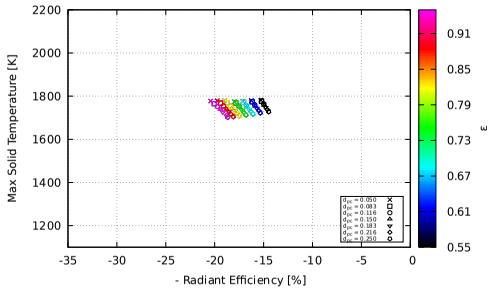

(h) $Q_{comb} = 1200$ kW and $L = 2.0$ cm.

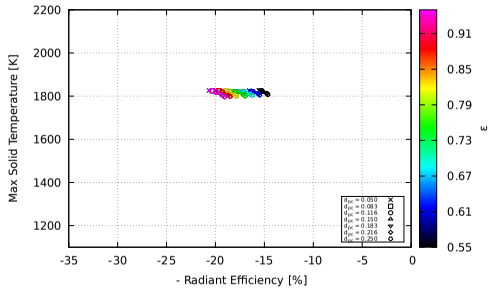

(i) $Q_{comb} = 1200$ kW and $L = 3.0$ cm.

Figure A.14: Interaction between d_{pc} and ε across Power/Length combinations.

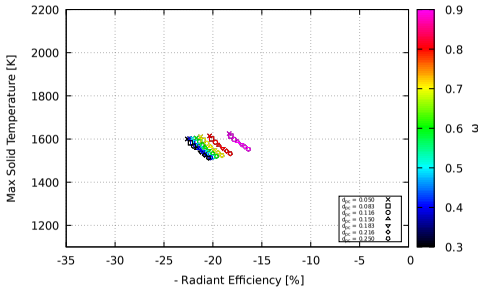

(a) $Q_{comb} = 800$ W and $L = 1.0$ cm.

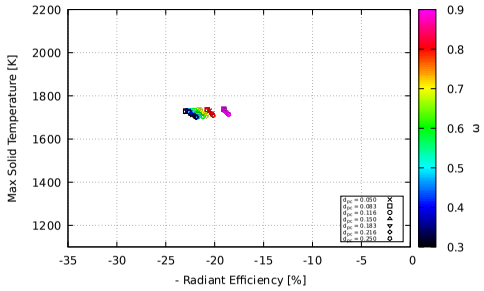

(b) $Q_{comb} = 800$ kW and $L = 2.0$ cm.

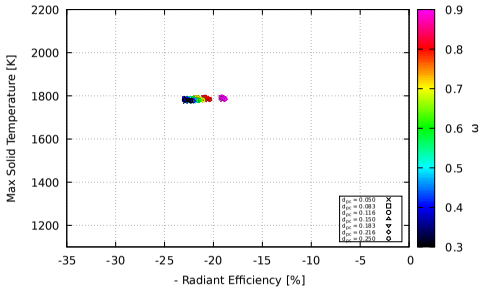

(c) $Q_{comb} = 800$ kW and $L = 3.0$ cm.

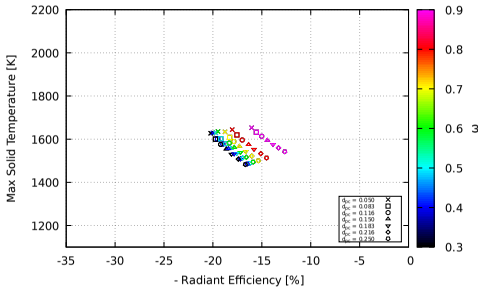

(d) $Q_{comb} = 1000$ kW and $L = 1.0$ cm.

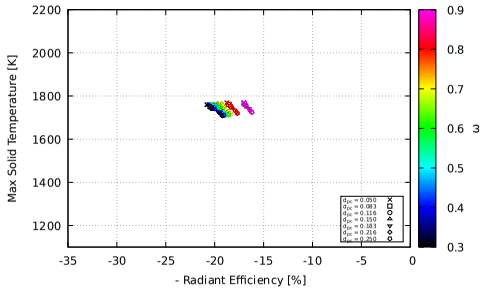

(e) $Q_{comb} = 1000$ kW and $L = 2.0$ cm.

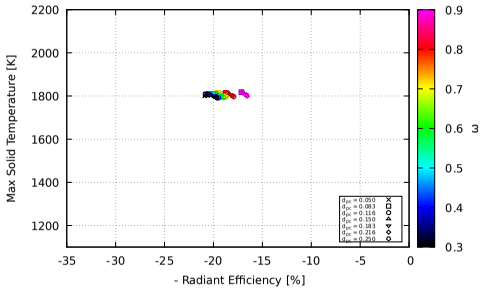

(f) $Q_{comb} = 1000$ kW and $L = 3.0$ cm.

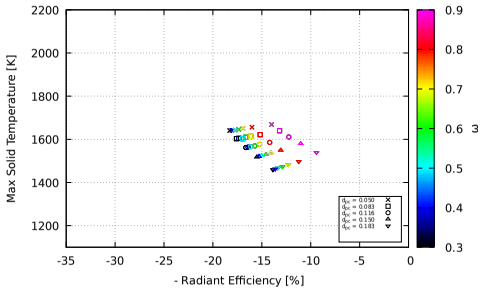

(g) $Q_{comb} = 1200$ kW and $L = 1.0$ cm.

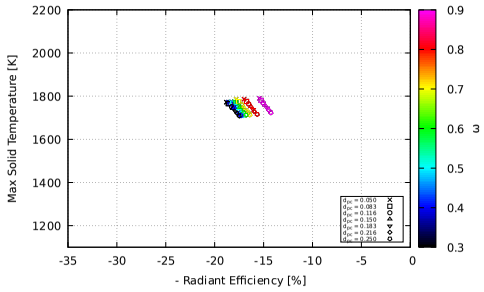

(h) $Q_{comb} = 1200$ kW and $L = 2.0$ cm.

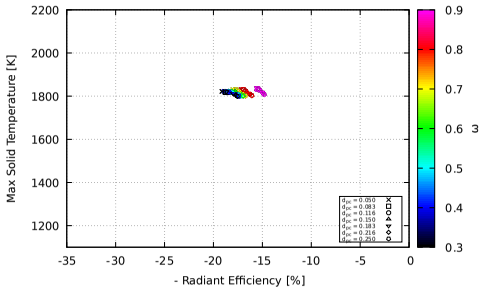

(i) $Q_{comb} = 1200$ kW and $L = 3.0$ cm.

Figure A.15: Interaction between d_{pc} and ω across Power/Length combinations.

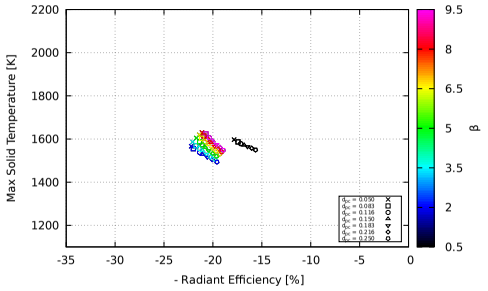

(a) $Q_{comb} = 800$ W and $L = 1.0$ cm.

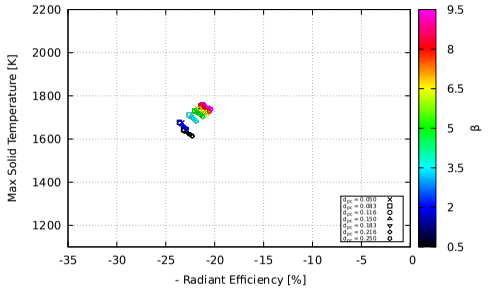

(b) $Q_{comb} = 800$ kW and $L = 2.0$ cm.

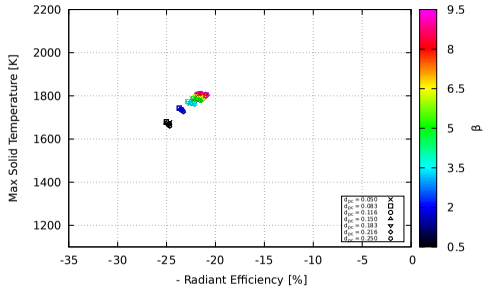

(c) $Q_{comb} = 800$ kW and $L = 3.0$ cm.

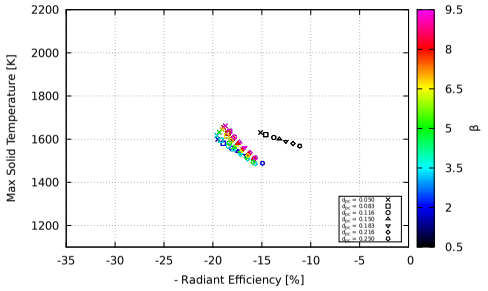

(d) $Q_{comb} = 1000$ kW and $L = 1.0$ cm.

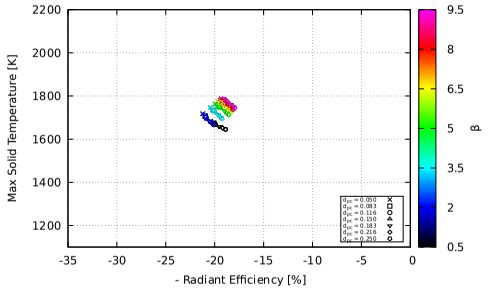

(e) $Q_{comb} = 1000$ kW and $L = 2.0$ cm.

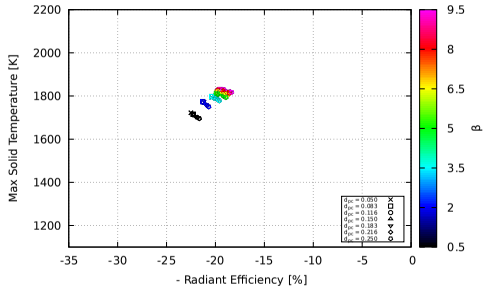

(f) $Q_{comb} = 1000$ kW and $L = 3.0$ cm.

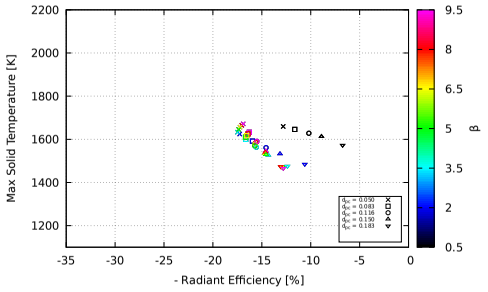

(g) $Q_{comb} = 1200$ kW and $L = 1.0$ cm.

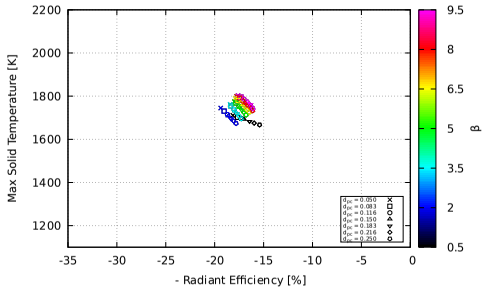

(h) $Q_{comb} = 1200$ kW and $L = 2.0$ cm.

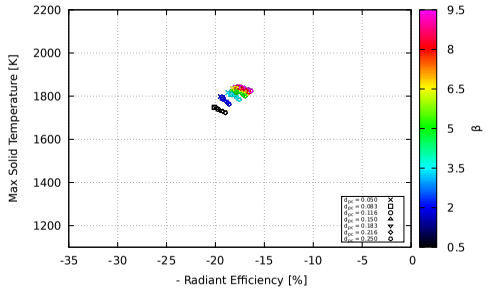

(i) $Q_{comb} = 1200$ kW and $L = 3.0$ cm.

Figure A.16: Interaction between d_{pc} and β across Power/Length combinations.

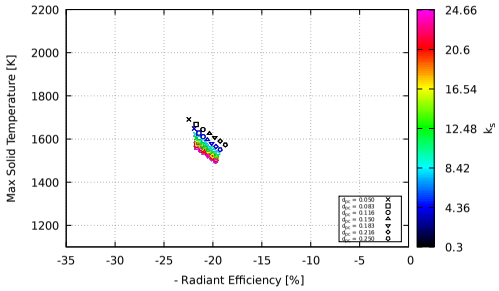

(a) $Q_{comb} = 800$ W and $L = 1.0$ cm.

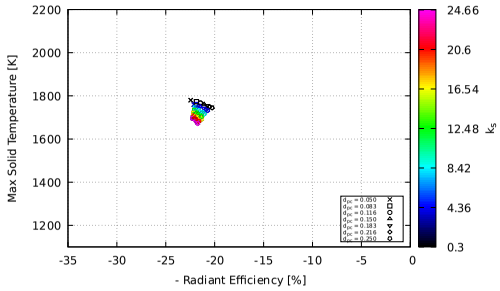

(b) $Q_{comb} = 800$ kW and $L = 2.0$ cm.

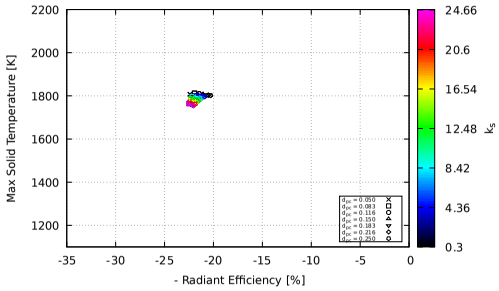

(c) $Q_{comb} = 800$ kW and $L = 3.0$ cm.

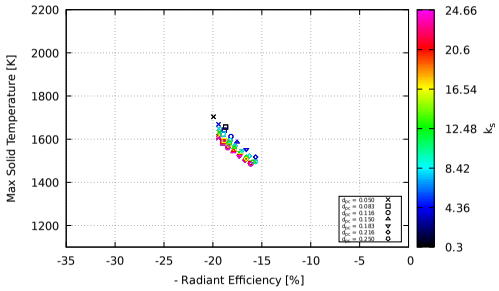

(d) $Q_{comb} = 1000$ kW and $L = 1.0$ cm.

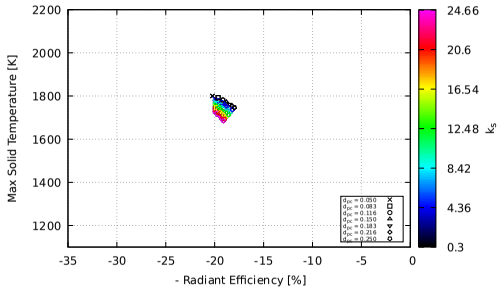

(e) $Q_{comb} = 1000$ kW and $L = 2.0$ cm.

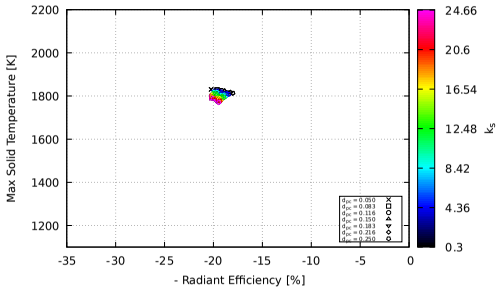

(f) $Q_{comb} = 1000$ kW and $L = 3.0$ cm.

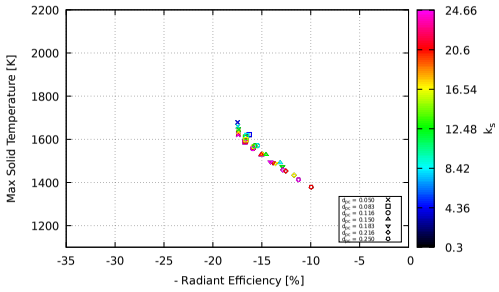

(g) $Q_{comb} = 1200$ kW and $L = 1.0$ cm.

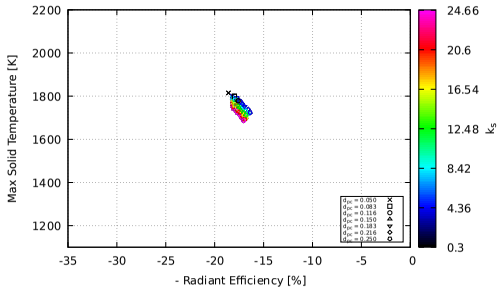

(h) $Q_{comb} = 1200$ kW and $L = 2.0$ cm.

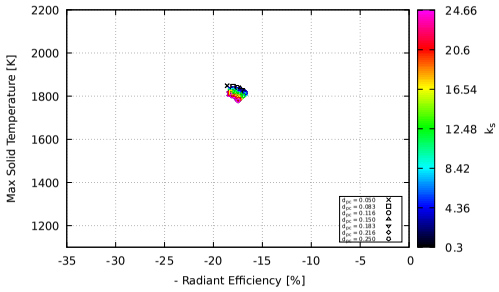

(i) $Q_{comb} = 1200$ kW and $L = 3.0$ cm.

Figure A.17: Interaction between d_{pc} and k_s across Power/Length combinations.

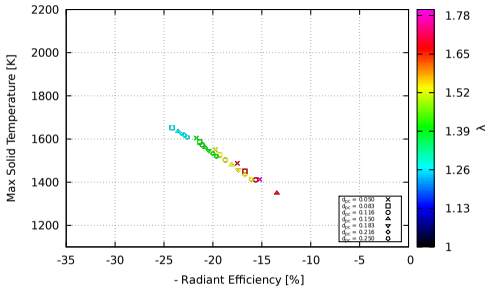

(a) $Q_{comb} = 800$ W and $L = 1.0$ cm.

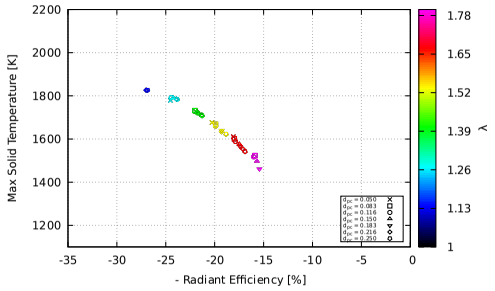

(b) $Q_{comb} = 800$ kW and $L = 2.0$ cm.

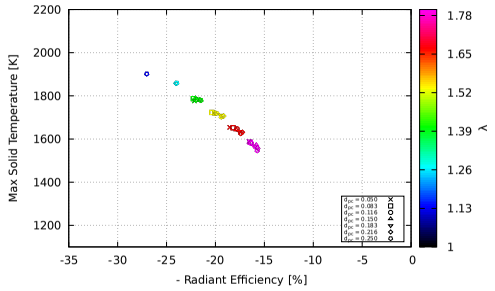

(c) $Q_{comb} = 800$ kW and $L = 3.0$ cm.

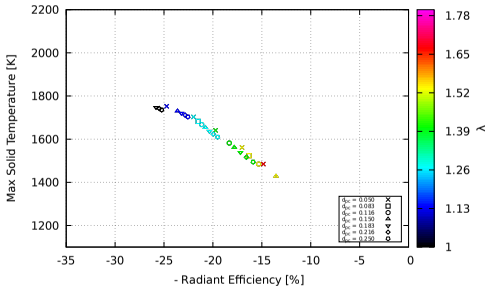

(d) $Q_{comb} = 1000$ kW and $L = 1.0$ cm.

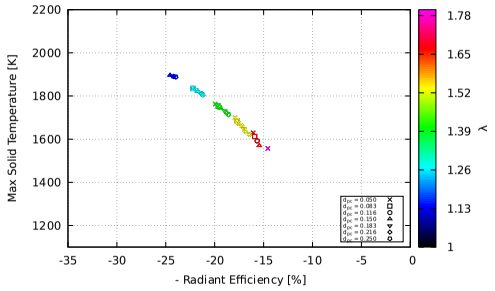

(e) $Q_{comb} = 1000$ kW and $L = 2.0$ cm.

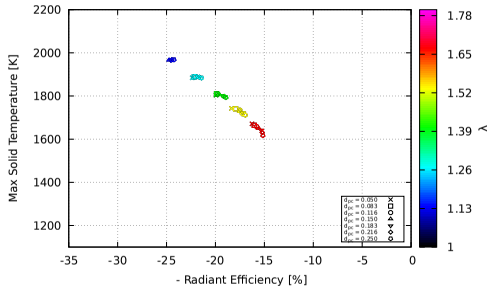

(f) $Q_{comb} = 1000$ kW and $L = 3.0$ cm.

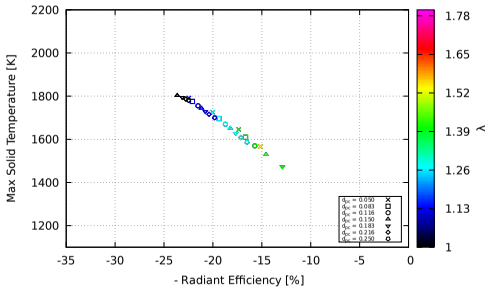

(g) $Q_{comb} = 1200$ kW and $L = 1.0$ cm.

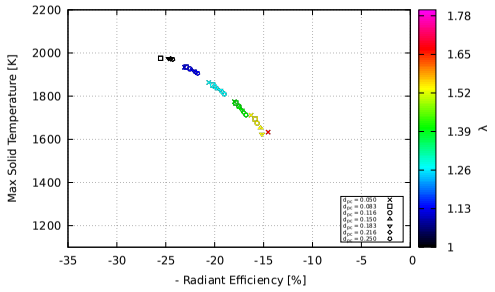

(h) $Q_{comb} = 1200$ kW and $L = 2.0$ cm.

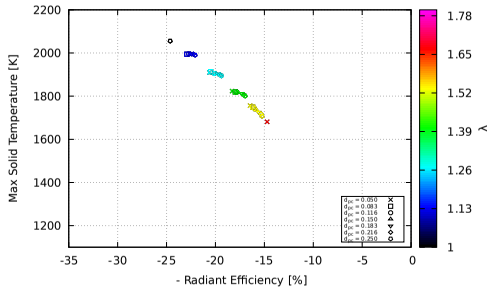

(i) $Q_{comb} = 1200$ kW and $L = 3.0$ cm.

Figure A.18: Interaction between d_{pc} and λ across Power/Length combinations.

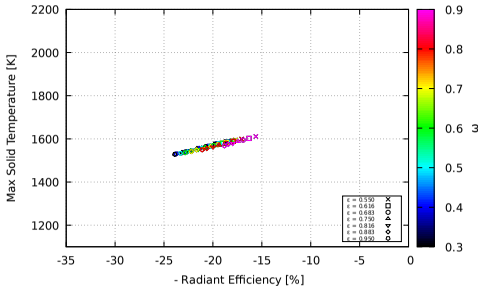

(a) $Q_{comb} = 800$ W and $L = 1.0$ cm.

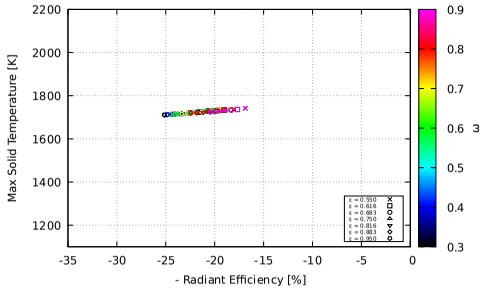

(b) $Q_{comb} = 800$ kW and $L = 2.0$ cm.

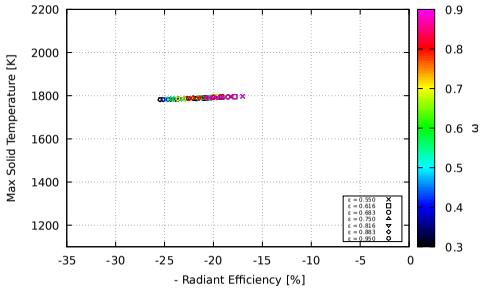

(c) $Q_{comb} = 800$ kW and $L = 3.0$ cm.

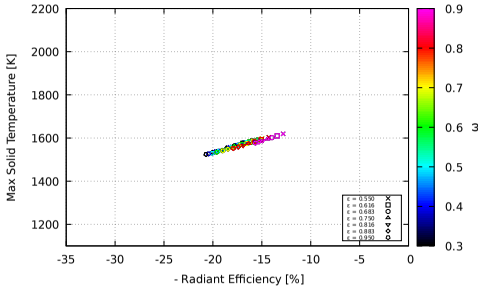

(d) $Q_{comb} = 1000$ kW and $L = 1.0$ cm.

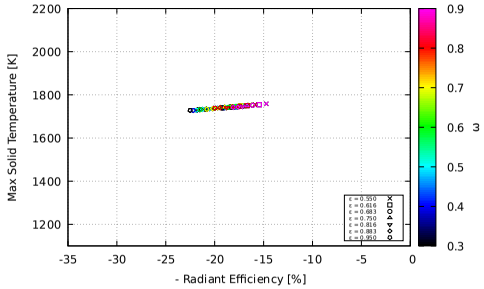

(e) $Q_{comb} = 1000$ kW and $L = 2.0$ cm.

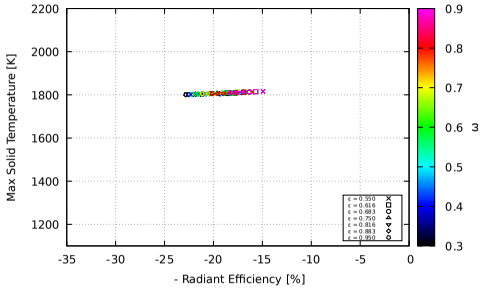

(f) $Q_{comb} = 1000$ kW and $L = 3.0$ cm.

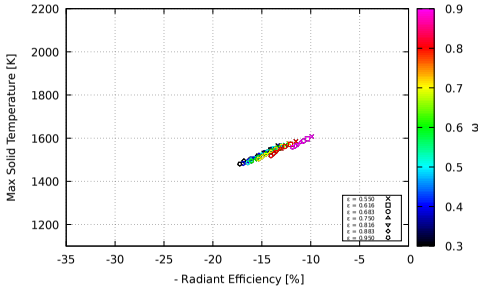

(g) $Q_{comb} = 1200$ kW and $L = 1.0$ cm.

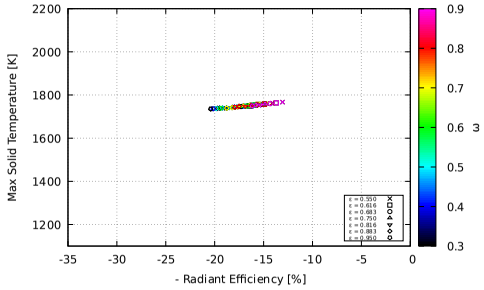

(h) $Q_{comb} = 1200$ kW and $L = 2.0$ cm.

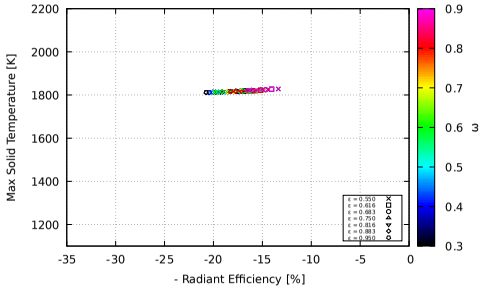

(i) $Q_{comb} = 1200$ kW and $L = 3.0$ cm.

Figure A.19: Interaction between ε and ω across Power/Length combinations.

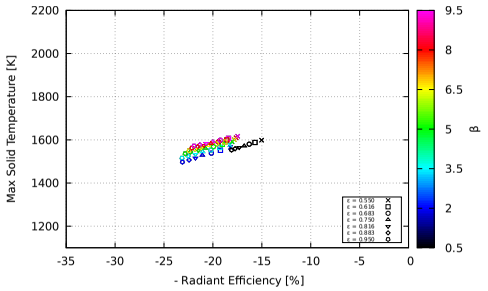

(a) $Q_{comb} = 800$ W and $L = 1.0$ cm.

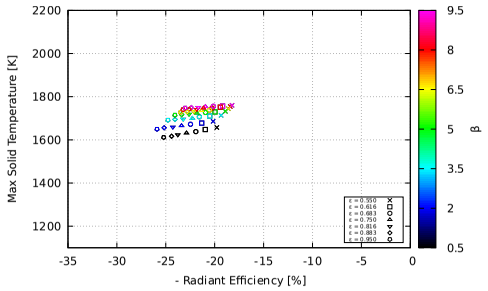

(b) $Q_{comb} = 800$ kW and $L = 2.0$ cm.

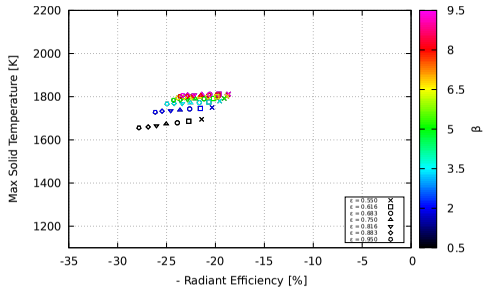

(c) $Q_{comb} = 800$ kW and $L = 3.0$ cm.

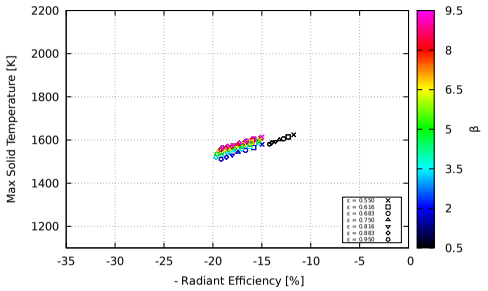

(d) $Q_{comb} = 1000$ kW and $L = 1.0$ cm.

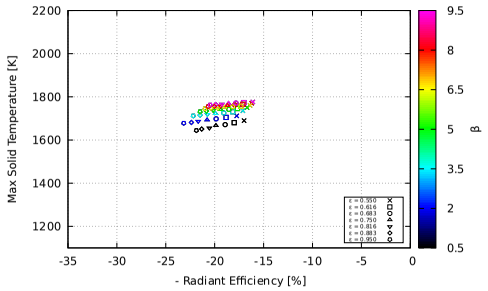

(e) $Q_{comb} = 1000$ kW and $L = 2.0$ cm.

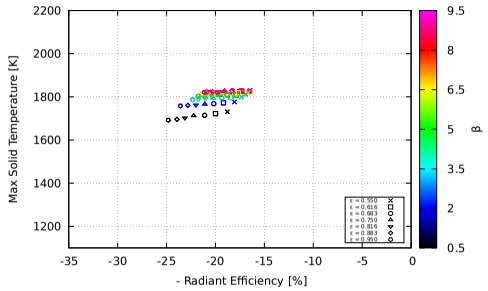

(f) $Q_{comb} = 1000$ kW and $L = 3.0$ cm.

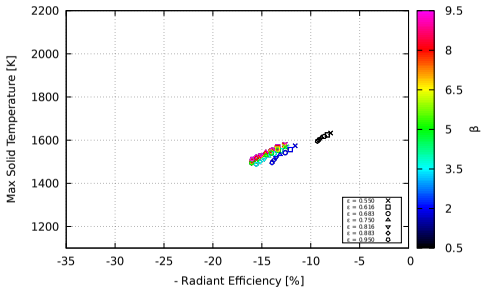

(g) $Q_{comb} = 1200$ kW and $L = 1.0$ cm.

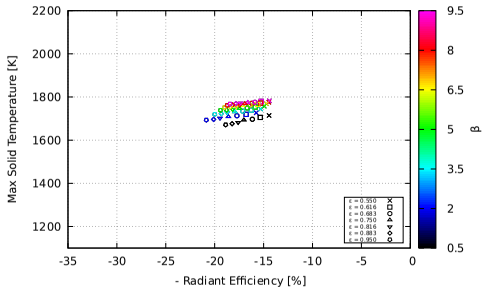

(h) $Q_{comb} = 1200$ kW and $L = 2.0$ cm.

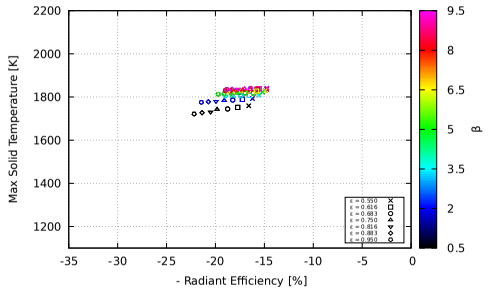

(i) $Q_{comb} = 1200$ kW and $L = 3.0$ cm.

Figure A.20: Interaction between ε and β across Power/Length combinations.

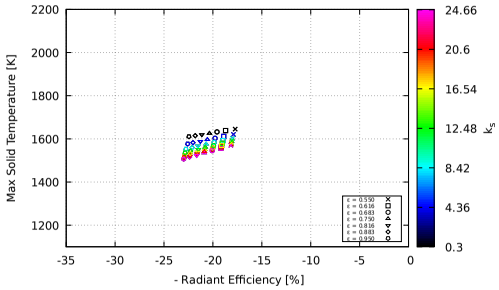

(a) $Q_{comb} = 800$ W and $L = 1.0$ cm.

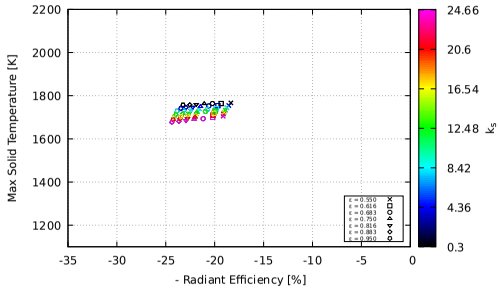

(b) $Q_{comb} = 800$ kW and $L = 2.0$ cm.

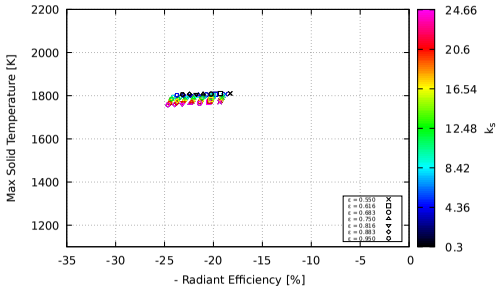

(c) $Q_{comb} = 800$ kW and $L = 3.0$ cm.

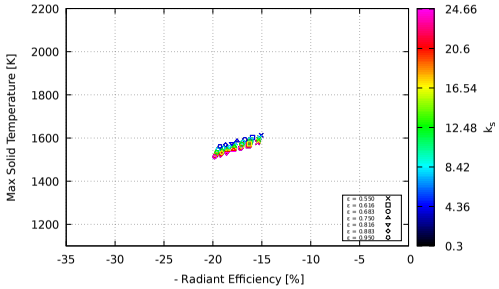

(d) $Q_{comb} = 1000$ kW and $L = 1.0$ cm.

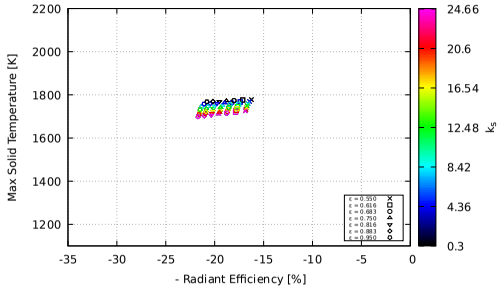

(e) $Q_{comb} = 1000$ kW and $L = 2.0$ cm.

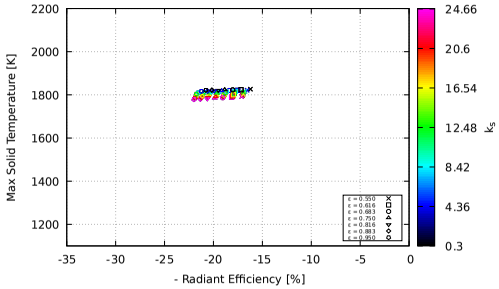

(f) $Q_{comb} = 1000$ kW and $L = 3.0$ cm.

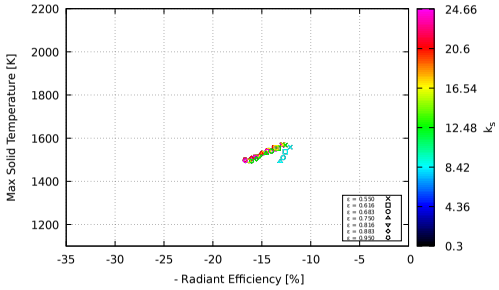

(g) $Q_{comb} = 1200$ kW and $L = 1.0$ cm.

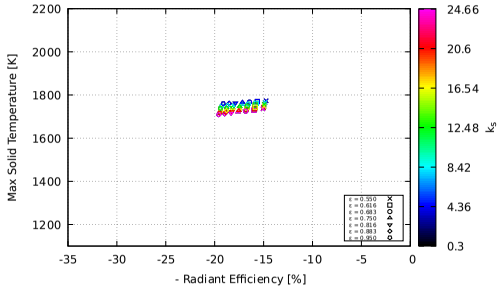

(h) $Q_{comb} = 1200$ kW and $L = 2.0$ cm.

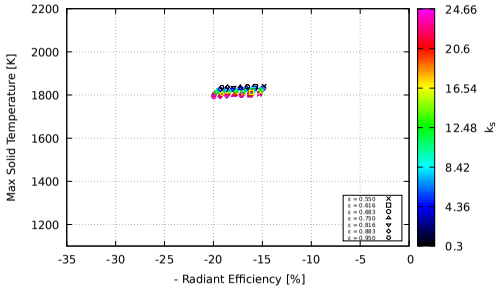

(i) $Q_{comb} = 1200$ kW and $L = 3.0$ cm.

Figure A.21: Interaction between ε and k_s across Power/Length combinations.

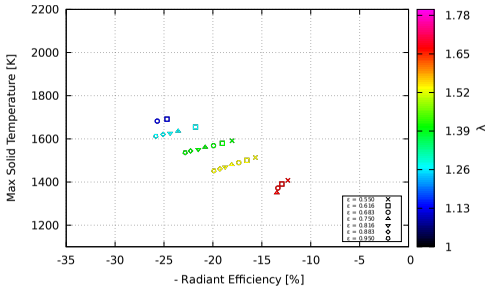

(a) $Q_{comb} = 800$ W and $L = 1.0$ cm.

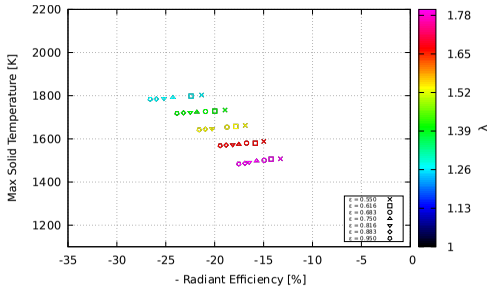

(b) $Q_{comb} = 800$ kW and $L = 2.0$ cm.

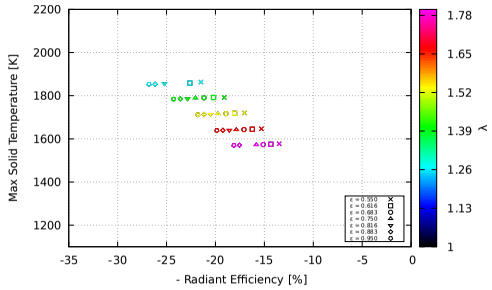

(c) $Q_{comb} = 800$ kW and $L = 3.0$ cm.

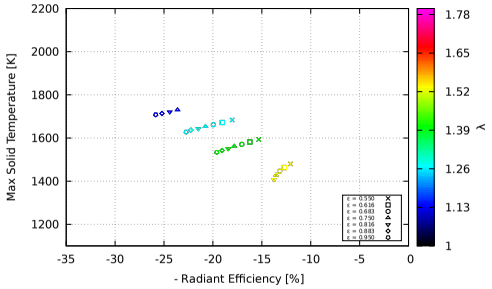

(d) $Q_{comb} = 1000$ kW and $L = 1.0$ cm.

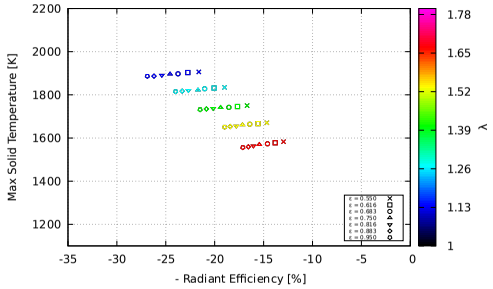

(e) $Q_{comb} = 1000$ kW and $L = 2.0$ cm.

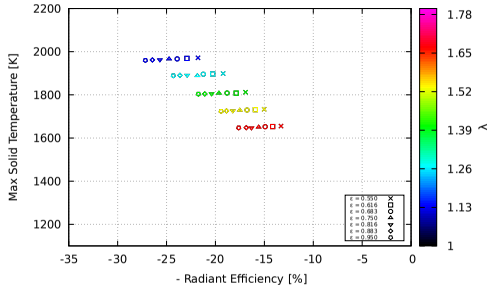

(f) $Q_{comb} = 1000$ kW and $L = 3.0$ cm.

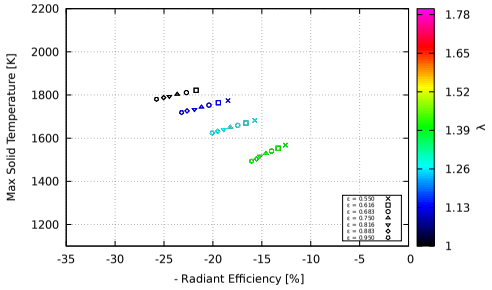

(g) $Q_{comb} = 1200$ kW and $L = 1.0$ cm.

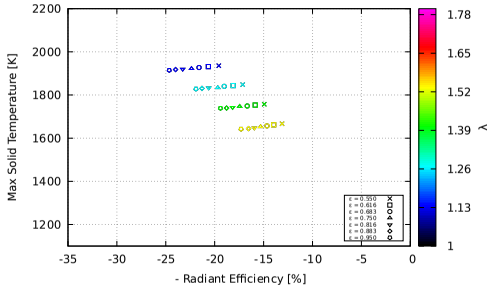

(h) $Q_{comb} = 1200$ kW and $L = 2.0$ cm.

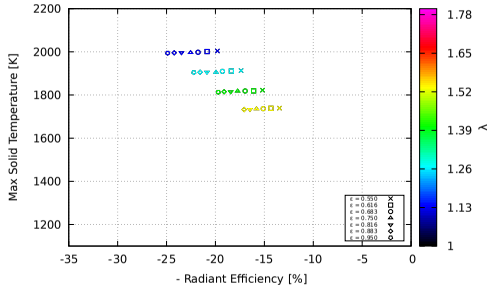

(i) $Q_{comb} = 1200$ kW and $L = 3.0$ cm.

Figure A.22: Interaction between ε and λ across Power/Length combinations.

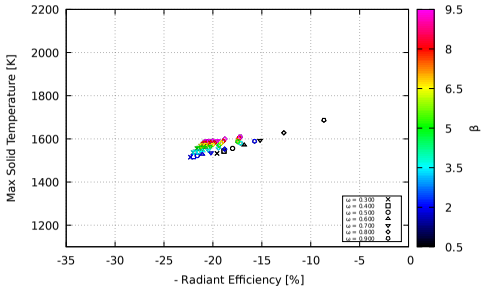

(a) $Q_{comb} = 800$ W and $L = 1.0$ cm.

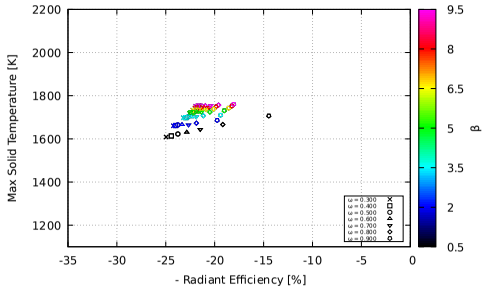

(b) $Q_{comb} = 800$ kW and $L = 2.0$ cm.

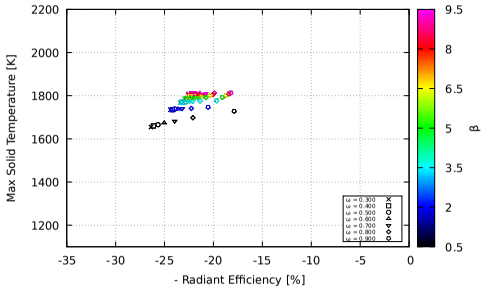

(c) $Q_{comb} = 800$ kW and $L = 3.0$ cm.

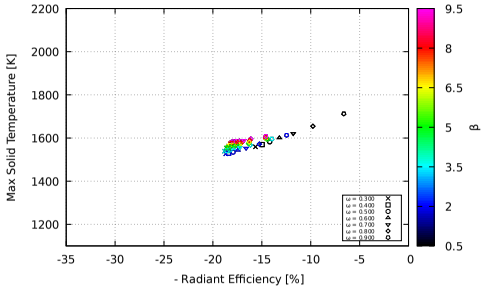

(d) $Q_{comb} = 1000$ kW and $L = 1.0$ cm.

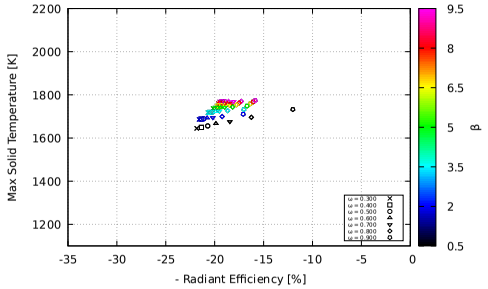

(e) $Q_{comb} = 1000$ kW and $L = 2.0$ cm.

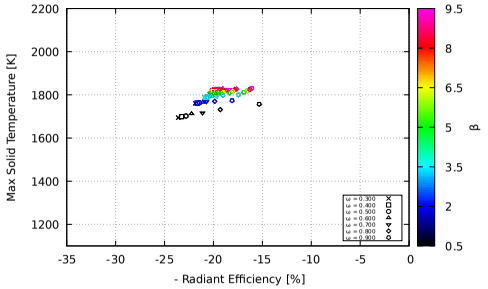

(f) $Q_{comb} = 1000$ kW and $L = 3.0$ cm.

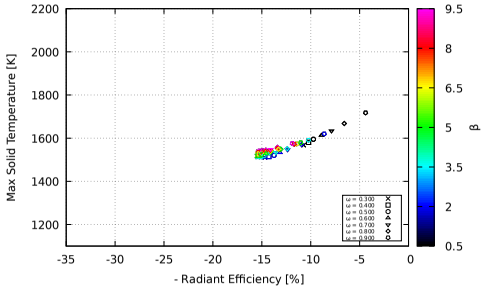

(g) $Q_{comb} = 1200$ kW and $L = 1.0$ cm.

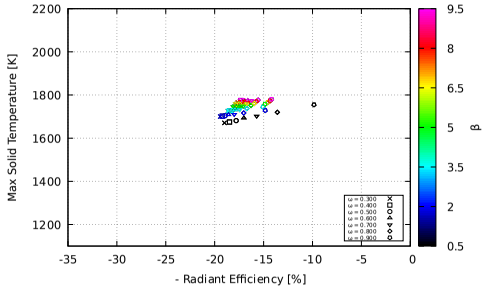

(h) $Q_{comb} = 1200$ kW and $L = 2.0$ cm.

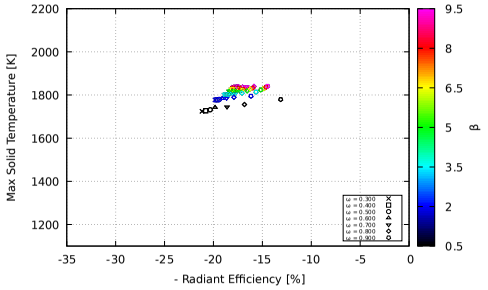

(i) $Q_{comb} = 1200$ kW and $L = 3.0$ cm.

Figure A.23: Interaction between ω and β across Power/Length combinations.

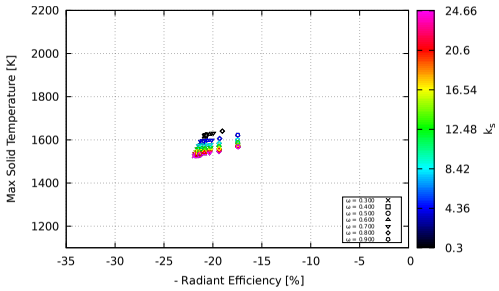

(a) $Q_{comb} = 800$ W and $L = 1.0$ cm.

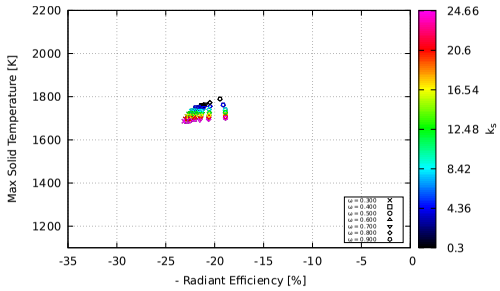

(b) $Q_{comb} = 800$ kW and $L = 2.0$ cm.

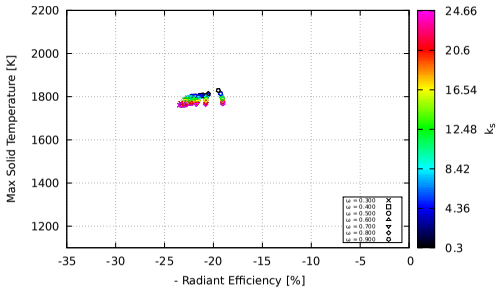

(c) $Q_{comb} = 800$ kW and $L = 3.0$ cm.

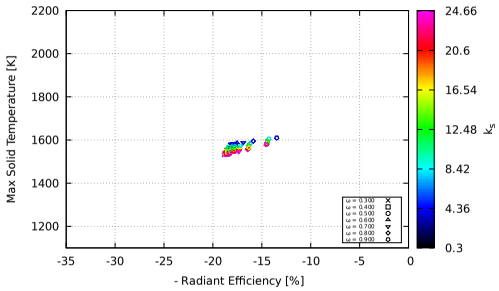

(d) $Q_{comb} = 1000$ kW and $L = 1.0$ cm.

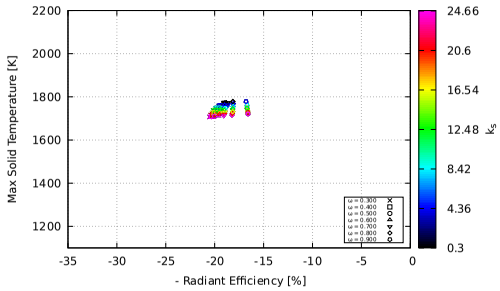

(e) $Q_{comb} = 1000$ kW and $L = 2.0$ cm.

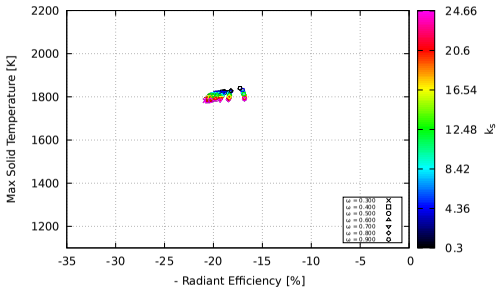

(f) $Q_{comb} = 1000$ kW and $L = 3.0$ cm.

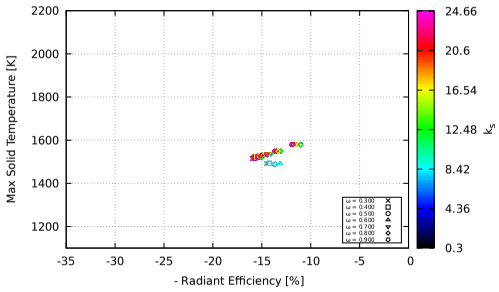

(g) $Q_{comb} = 1200$ kW and $L = 1.0$ cm.

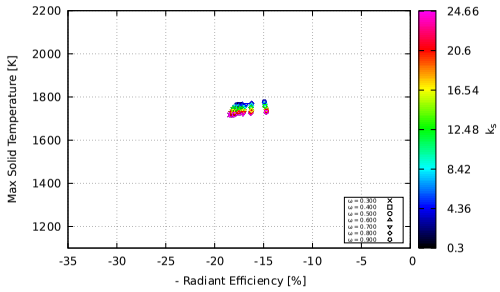

(h) $Q_{comb} = 1200$ kW and $L = 2.0$ cm.

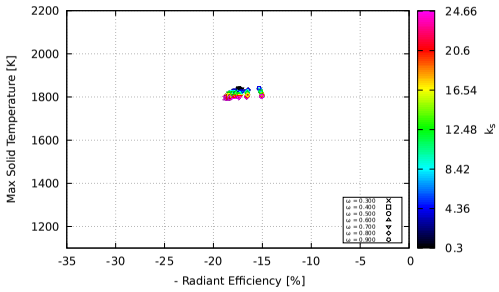

(i) $Q_{comb} = 1200$ kW and $L = 3.0$ cm.

Figure A.24: Interaction between ω and k_s across Power/Length combinations.

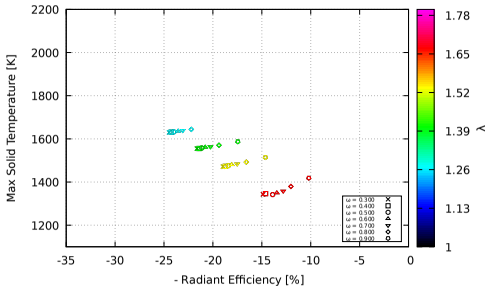

(a) $Q_{comb} = 800$ W and $L = 1.0$ cm.

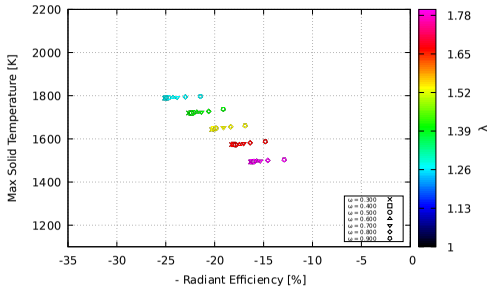

(b) $Q_{comb} = 800$ kW and $L = 2.0$ cm.

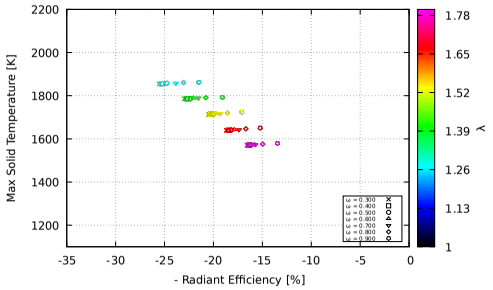

(c) $Q_{comsathe:b} = 800$ kW and $L = 3.0$ cm.

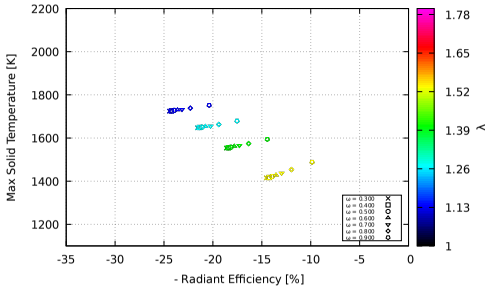

(d) $Q_{comb} = 1000$ kW and $L = 1.0$ cm.

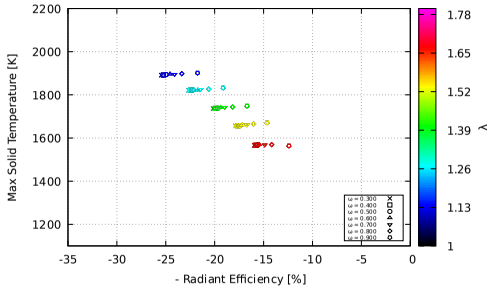

(e) $Q_{comb} = 1000$ kW and $L = 2.0$ cm.

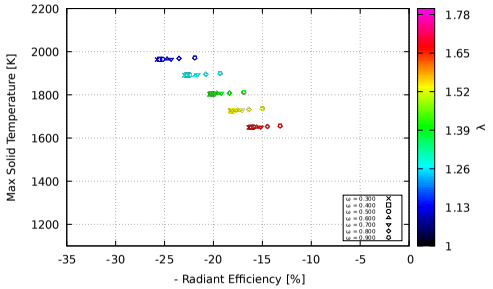

(f) $Q_{comb} = 1000$ kW and $L = 3.0$ cm.

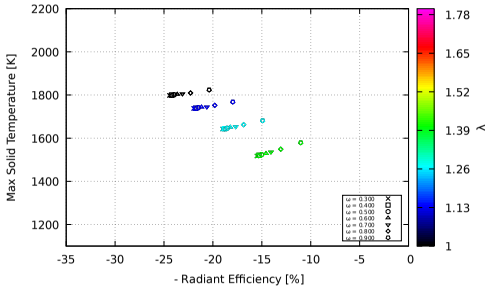

(g) $Q_{comb} = 1200$ kW and $L = 1.0$ cm.

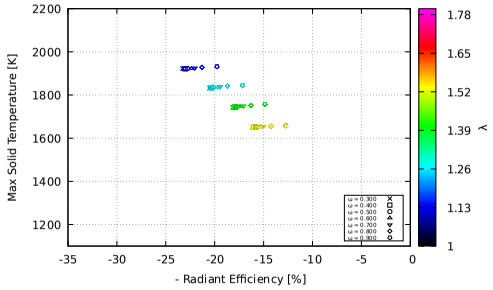

(h) $Q_{comb} = 1200$ kW and $L = 2.0$ cm.

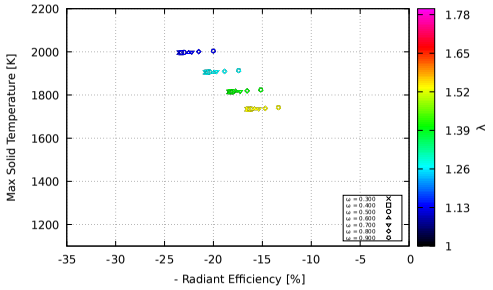

(i) $Q_{comb} = 1200$ kW and $L = 3.0$ cm.

Figure A.25: Interaction between ω and λ across Power/Length combinations.

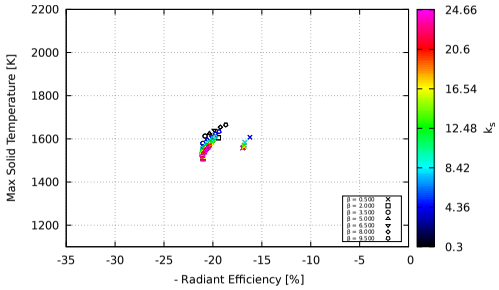

(a) $Q_{comb} = 800$ W and $L = 1.0$ cm.

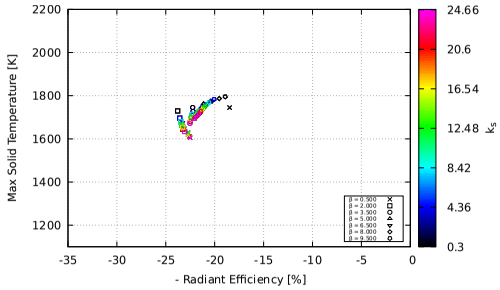

(b) $Q_{comb} = 800$ kW and $L = 2.0$ cm.

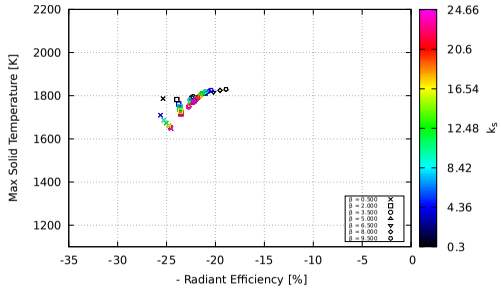

(c) $Q_{comb} = 800$ kW and $L = 3.0$ cm.

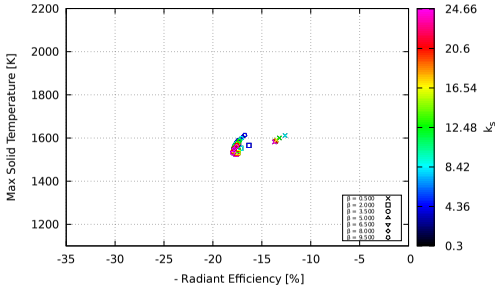

(d) $Q_{comb} = 1000$ kW and $L = 1.0$ cm.

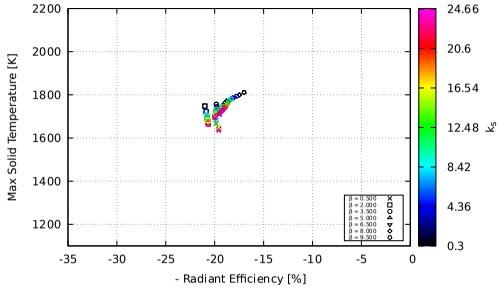

(e) $Q_{comb} = 1000$ kW and $L = 2.0$ cm.

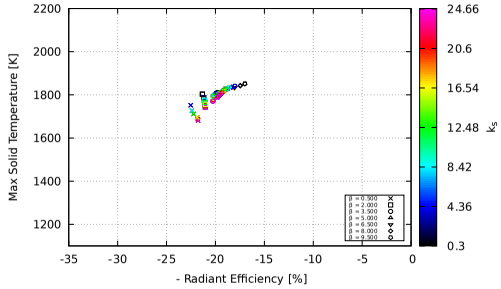

(f) $Q_{comb} = 1000$ kW and $L = 3.0$ cm.

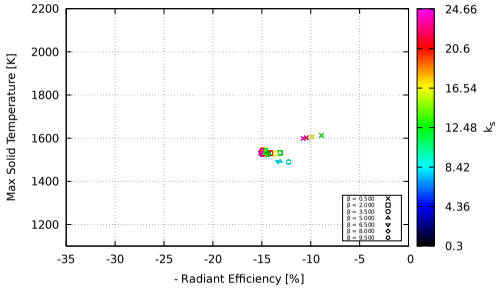

(g) $Q_{comb} = 1200$ kW and $L = 1.0$ cm.

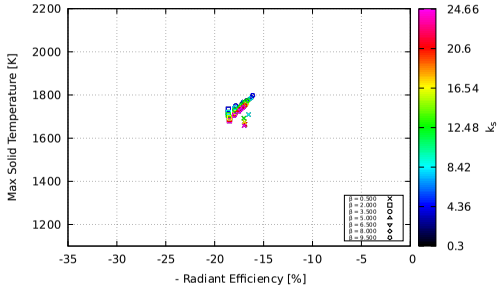

(h) $Q_{comb} = 1200$ kW and $L = 2.0$ cm.

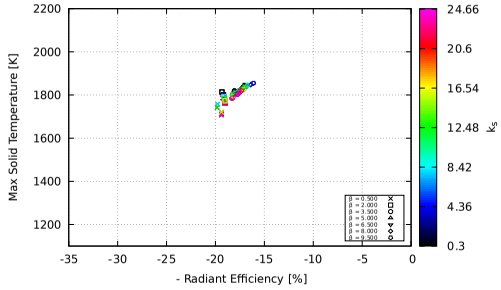

(i) $Q_{comb} = 1200$ kW and $L = 3.0$ cm.

Figure A.26: Interaction between β and k_s across Power/Length combinations.

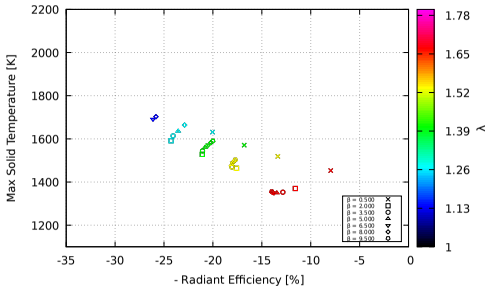

(a) $Q_{comb} = 800$ W and $L = 1.0$ cm.

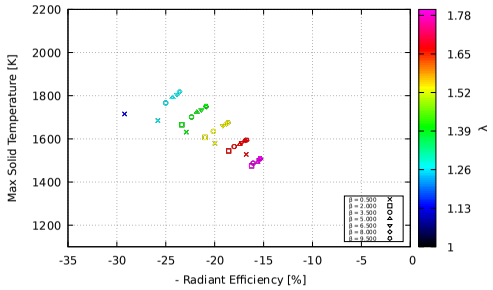

(b) $Q_{comb} = 800$ kW and $L = 2.0$ cm.

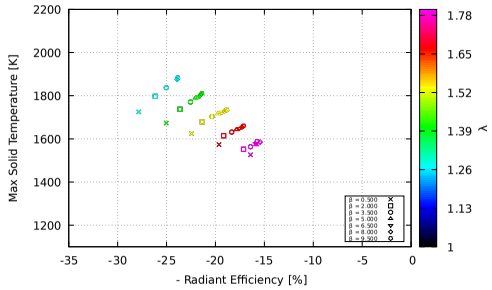

(c) $Q_{comb} = 800$ kW and $L = 3.0$ cm.

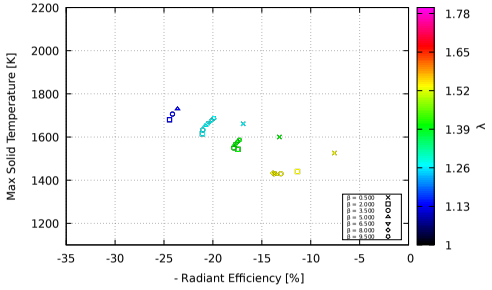

(d) $Q_{comb} = 1000$ kW and $L = 1.0$ cm.

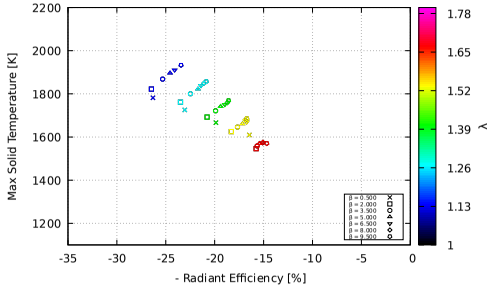

(e) $Q_{comb} = 1000$ kW and $L = 2.0$ cm.

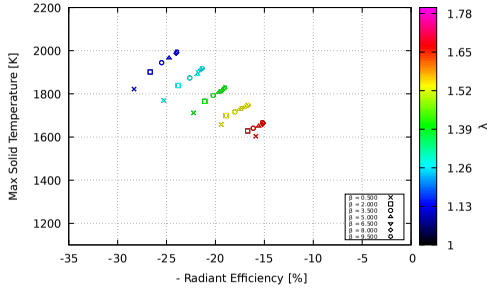

(f) $Q_{comb} = 1000$ kW and $L = 3.0$ cm.

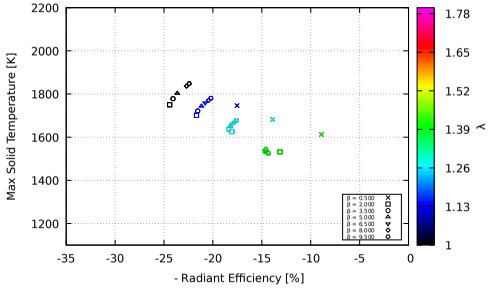

(g) $Q_{comb} = 1200$ kW and $L = 1.0$ cm.

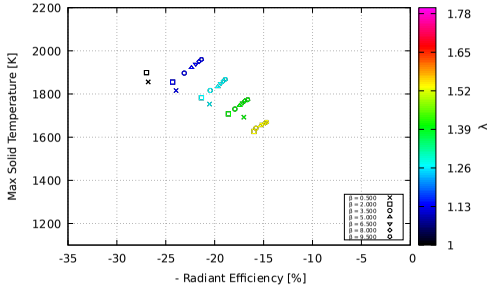

(h) $Q_{comb} = 1200$ kW and $L = 2.0$ cm.

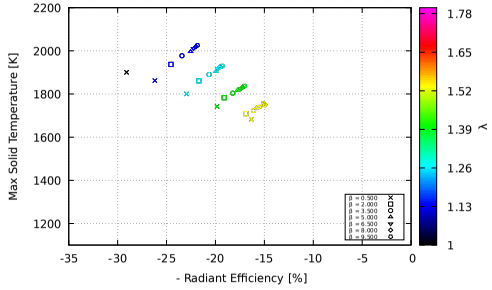

(i) $Q_{comb} = 1200$ kW and $L = 3.0$ cm.

Figure A.27: Interaction between β and λ across Power/Length combinations.

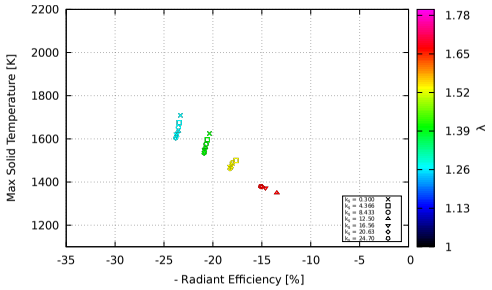

(a) $Q_{comb} = 800$ W and $L = 1.0$ cm.

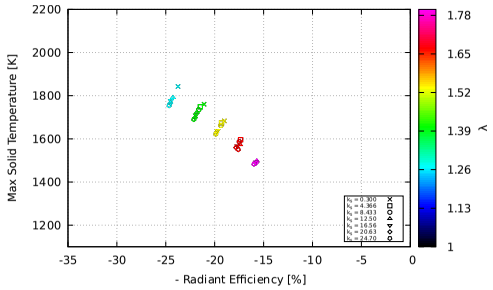

(b) $Q_{comb} = 800$ kW and $L = 2.0$ cm.

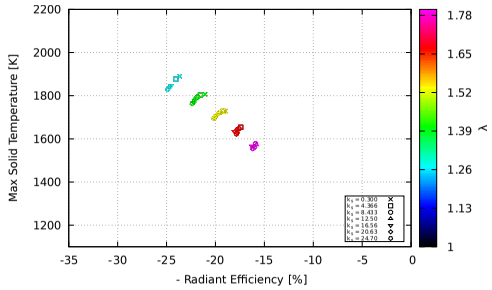

(c) $Q_{comb} = 800$ kW and $L = 3.0$ cm.

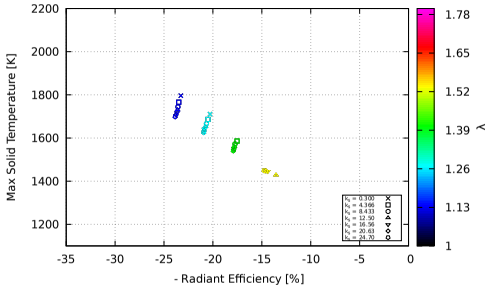

(d) $Q_{comb} = 1000$ kW and $L = 1.0$ cm.

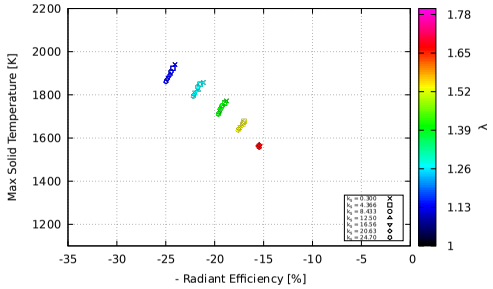

(e) $Q_{comb} = 1000$ kW and $L = 2.0$ cm.

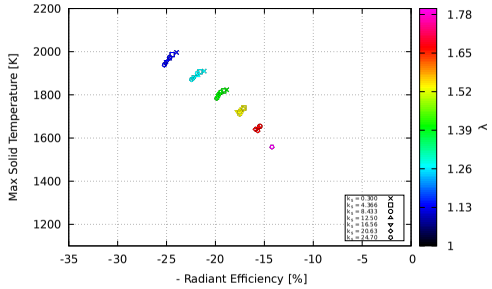

(f) $Q_{comb} = 1000$ kW and $L = 3.0$ cm.

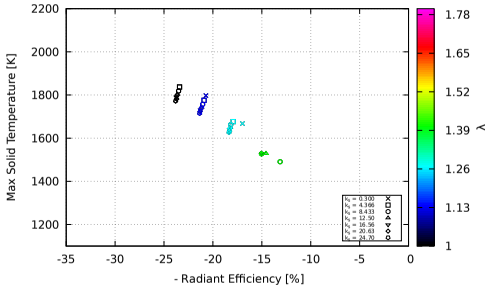

(g) $Q_{comb} = 1200$ kW and $L = 1.0$ cm.

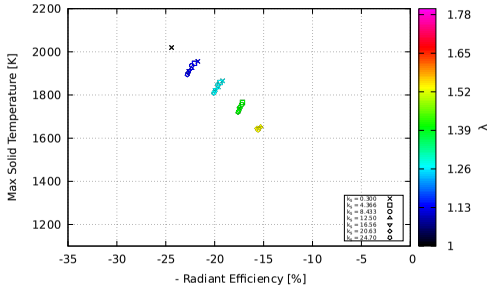

(h) $Q_{comb} = 1200$ kW and $L = 2.0$ cm.

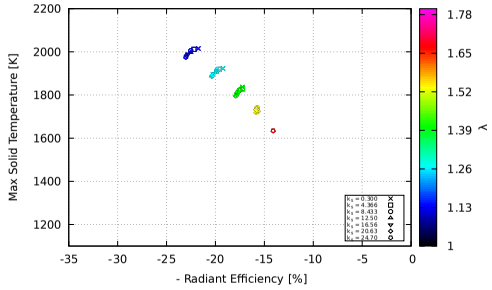

(i) $Q_{comb} = 1200$ kW and $L = 3.0$ cm.

Figure A.28: Interaction between k_s and λ across Power/Length combinations.